Mathematical Investigation of Hydrodynamic Contributions to Amoeboid Cell Motility in *Physarum polycephalum*

By

OWEN LESLIE LEWIS
B.S. (Harvey Mudd College) 2005

DISSERTATION

Submitted in partial satisfaction of the requirements for the degree of

DOCTOR OF PHILOSOPHY

in

Applied Mathematics

in the

OFFICE OF GRADUATE STUDIES

of the

UNIVERSITY OF CALIFORNIA

DAVIS

Approved:

Robert D. Guy (Chair)

Alex Mogilner

John K. Hunter

Juan Carlos del Álamo

Committee in Charge

2014

ProQuest LLC.
789 East Eisenhower Parkway
P.O. Box 1346
Ann Arbor, MI 48106 - 1346

To Those Who Come After.

Abstract

In this work, we investigate the role of intracellular fluid flow in the migration of *Physarum polycephalum*. We develop two distinct models. Initially, we model the intracellular space of a *physarum* plasmodium as a peristaltic chamber. We derive a PDE relating the deformation of the chamber boundary and the flux of fluid along the chamber center line. We then solve this PDE for two distinct boundary deformations and evaluate the characteristic stress associated with the peristaltic flow. We compare the derived stress, as well as the relative phase of the deformation and flow waves, with values seen in experiments. Second, we develop a poro-elastic model of the interior of *physarum* that accounts for cytoskeletal structure, as well as adhesive interactions with the substrate. We develop this model within a framework similar to the Immersed Boundary method, which readily allows for computer simulation. We then use this model to simulate cell crawling across a range of parameters that characterize the coordination of adhesion to the substrate. We identify a spatio-temporal form of adhesion coordination that is consistent with experiments. We also show that this form is both efficient and robust, when compared to similar forms of adhesion coordination.

Acknowledgments

I would like to thank my advisor Dr. Robert D. Guy for his years of patience, assistance, and tutelage. I would also like to thank my collaborators Dr. Toshiyuki Nakagaki, Dr. Juan Carlos del Álamo, and Shun Zhang for their expertise and time. Their experiments greatly enriched my own work. Finally, I would like to thank Laura Luttmer, for being there.

Table of Contents

CHAPTER 1

Introduction

1.1 Amoeboid Motility

Cell migration plays a critical role in a wide variety of biological processes. From wound healing and immune response to morphogenesis, the mechanics of motile cells play a key part. Amoeboid motility is a fast type of cell migration defined by large shape changes as the cell extends and retracts various pseudopodia and blebs [BRA01]. Research on amoeboid motility has recently intensified in part because of a newfound appreciation of the broad applicability of amoeboid motility types. This migration mode is robust to changes in the extracellular matrix and may be used to move across a 2-D surface or through a 3-D environment [CHA08B]. Furthermore, studies have suggested that the general mechanisms of amoeboid motility may be independent of the specific molecular nature of the cell-matrix adhesions [LÄM08]. Thus, amoeboid cells are able to cross barriers, move through confined channels, or squeeze through 3-D matrices by contracting and pushing off the surrounding environment. Certain cancer cells have even been shown to dynamically regulate motility type and switch to amoeboid motility, based on chemical treatments or extracellular geometry [KEL00, SAB09].

Despite the vast existing knowledge about the biological and molecular processes involved in amoeboid migration, our understanding of the underlying mechanical processes is still rather phenomenological. Cells exhibiting amoeboid migration must generate protrusive stresses to drive the leading edge forward. These stresses may be generated by the polymerization of filamentous actin or by a flow of cytoplasm driven by contraction induced pressure [LÄM09]. Furthermore, in order for locomotion to take place, internal stresses must be transmitted to the substrate. In the traditional paradigm of mesenchymal motility, the transmission of stress is accomplished by an array of regulated proteins that mediate adhesion to the substrate. However, there is evidence that amoeboid cells can migrate in 3-D environments *without* specific molecular adhesion. It has been suggested that fluid-driven motility modes may be well suited to migration in the absence of specific adhesion because intracellular pressure pushing on the extracellular matrix may generate a frictional force large enough for the cell to push or pull itself through the environment [Cha08b]. However, this hypothetical description of amoeboid motility has not been tested. It seems clear that motility of this form requires the coordination of contractile stresses (to generate pressure gradients), flow of cytoplasmic material, and mechanical interactions with the extracellular matrix (whether specific molecular adhesions or not). However, at this point we lack any quantitative understanding of how these effects may be coordinated in motile amoeboid cells.

To address this issue, mathematical modeling can be extremely helpful. Mathematical models allow "measurement" of quantities that are virtually inaccessible through experiment; for example, intracellular pressure is difficult to measure, but readily computable in a model of fluid dynamics. Furthermore, mechanistic models provide the ability to directly control parameters that may be impossible to perturb in experiments, or difficult to alter without undesired downstream effects. Thus, modeling provides the ability to completely isolate the effects of a particular mechanical component of the system in question. This can be extremely helpful in understanding the complex interplay of mechanical forces that generate cell motility.

1.2 *Physarum polycephalum*

Physarum polycephalum is a large multi-nucleated slime mold that belongs to the supergroup *Amoebozoa*. The subgroup of *Dictyostelids* are known as cellular slime molds and are comprised of mononuclear cells that can form multicellular aggregates that coordinate behavior through chemical signaling [Pál96]. Members of *Dictyostelium* have been the subject of much study, including the mechanisms by which both individuals and aggretate "slugs" migrate [DA07, Rie05]. In contrast, *physarum* belongs to the "acellular" or plasmodial slime mold subgroup of *Myxomycetes*. *Physarum* is composed of a large, multinucleated aggregate of cytoplasm, which may grow to the macro-scale but lacks membrane divisions between individual cells.

Due to its large size, *physarum* is relatively easy to study under a light microscope, and has been used as a model organism in cellular biology for several decades. *Physarum* was heavily studied in early investigations into the nature and movement of cytoplasm [Kam59]. Due to the prevailence of large intracellular flows, the streaming of cytoplasm within *physarum* plasmodia has been the focus of cytology studies [Kes82, Kam68, Kam61]. In addition to simple streaming of cytoplasm, the plasmodium of *physarum* exhibits a vast array of cellular behaviors that have been studied in a variety of contexts. The emergence of contractile patterns has been studied in the context of coupled oscillators [Tak97a, Tak97b, Tak00, Tak01, Nak99, Ter05] and complex viscoelastic materials [Tep91, Rad13, Tep97, Ost84]. The branching of flow networks within *physarum* has even been studied as a model system of transportation networks [Bau13, Bau10].

Physarum plasmodia grow an intricate branched network of gelated cytoplasm that resembles a vascular system. This network merges into a fan-shaped structure at the leading edge of the organism as it migrates across its substrate. Figure 1.1a shows a fully grown organism and this cytoplasmic network. Through the network, the organism generates a periodic back-and-forth flow of cytoplasm known as shuttle streaming. This flow is driven by pressure gradients created by contraction of the actomyosin network within the cell [All63, Ohl95, Kuk87], which is regulated by a Ca^{2+} oscillation [Yos10].

Removing a small sample of the organism results in a so-called microplasmodium. Examples of microplasmodia may be seen in the Figure 1.1b and the insets of Figure 1.1c The multinucleated nature of *physarum* means that these smaller scale plasmodia are capable of sustaining organic function and may eventually grow back to the scale of the original. Initially after segregation, microplasmodia adopt a round shape and begin to reorganize their disrupted cytoskeleton [Nag75]. As the microplasmodia grow to a critical size (approximately 100 µm across), a sharp transition occurs [Koy98]. An elongated tadpole-like shape develops, with a flow channel of non-gelated cytoplasm along the cell longitudinal axis. This results in a drastic increase in intracellular fluid velocity as a distinct pattern of cytoplasmic flow develops. In Figure 1.1c we show data from our experimental collaborators Shun Zhang and Juan Carlos del Álamo where several plasmodium are allowed to grow while their "shape factor," $S_f = P^2/4\pi A$ is measured. Here, P is the perimeter of the cell and A is its area. A shape factor of one corresponds to a perfectly round cell, while a larger shape factor indicates elongation. The data clearly illustrates this sharp transition as a function of microplasmodium size. Once this transition occurs, the smaller *physarum* amoebae may exhibit a similar behavior to their macroscale counterparts. In these microplasmodia, a rhythmic stream of cytoplasm flows back and forth along the centerline of the cell: a precursor to the shuttle streaming seen in developed plasmodial networks. The onset of this behavior has been observed to coincide with a drastic increase in the locomotion speed of growing *physarum*. It has naturally been hypothesized that the flow of cytoplasm is therefore a driving phenomenon in this particular example of amoeboid motility.

Due to the relatively large scale of the plasmodia, Particle Image Velocimetry (PIV) experiments allow

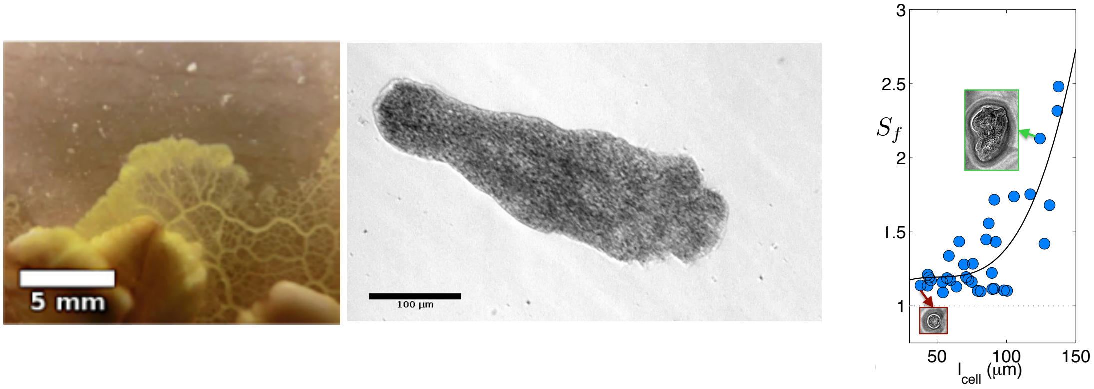

(a) Fully developed plasmodium.

(b) Small developing microplasmodium segregated from mature organism.

(c) Transition of shape factor.

Figure 1.1: A *physarum* plasmodium is shown in (a), illustrating the plasmodial network of a fully developed organism. A microplasmodium is shown in (b) that was generated by removing a small portion of the mature organism. In (c) we present measurements showing the shape factor $S_f = P^2/4\pi A$ of *physarum* microplasmodia as a function of the cell length. Data shows a sudden elongation (associated with cytoplasmic streaming) at a critical plasmodium size. The inset shows two example microplasmodia, before and after elongation. Unpublished data courtesy of Shun Zhang and Juan Carlos del Álamo.

researchers to measure the intracellular fluid velocity in *physarum* using cell organelles as flow tracers. In [Mat08], the authors perform PIV to measure the spatiotemporal flow of cytoplasm within migrating *physarum* microplasmodia. In these experiments, the authors observe a periodic, pulsatile flow of cytoplasm forward and backward along the longitudinal axis of the plasmodium body. A region of forward flow (directed toward the anterior end of the cell) develops at the plasmodium posterior and propagates forward along the cell axis. This is followed by a region of backward flow that also develops at the posterior of the cell and propagates to the anterior. Thus, the spatiotemporal organization of the cytoplasmic flow is characterized by a *phase wave* profile. A phase wave is a profile of the form $f(kx - \omega t)$, where f is some periodic function (such as a sinusoid). For such waveforms, the wave profile will propagate through the domain with velocity ω/k. Figure 1.2 shows flow data reported in [Mat08] as a function of time and the longitudinal cell body coordinate (called the Anterior-Posterior (AP) axis by the authors). The pitched lines of constant flow velocity (marked by circles) indicate the phase wave character of the flow, and the slope of these lines represents the phase velocity.

In [Mat08], it is argued that the phase wave nature of the cytoplasmic flow is critical to generating motility via the observed behavior. This argument is motivated by two key observations. First, the direction that the phase wave travels is from the posterior to the anterior of the cell. The anterograde propogation

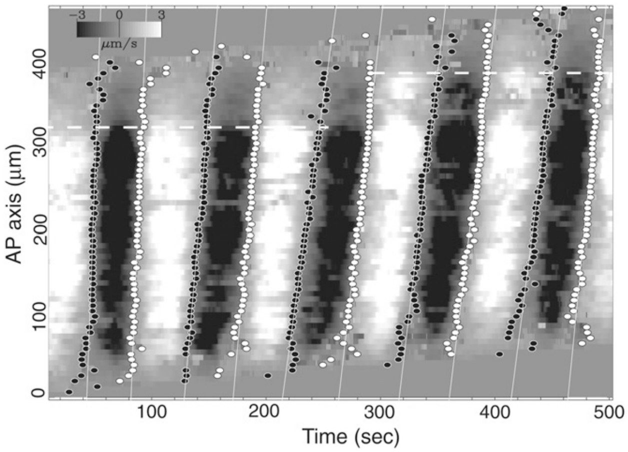

Figure 1.2: Maximum flow along the cell axis as a function of time and location on the Anterior-Posterior (AP) axis of the cell. Circles denote stagnation points of zero flow velocity. Open circles indicate a transition from backward to forward flow, while filled circles indicate a transition from forward to backward flow. Reprinted from [Mat08] with permission from Elsevier.

of the flow wave is argued to result in a net forward displacement of fluid within the cell, and thus the center of mass is transported forward. We reproduce this argument in more detail in Chapter 4. The second observation of [Mat08] is that the flow wave is of the same wavelength and period as the wave of contraction on the cell exterior. The two waves have a well-defined phase relative to one another. This phase relationship ensures that forward flow of cytoplasm occurs at locations on the cell body that are (on average) wider than locations in which cytoplasm is flowing backwards. Again, this is argued to imply a net forward flux of material, and thus a translation of the cell. Both of these explanations of motility are based purely on hydrodynamic phenomena. Neither includes a discussion of the stresses generated by this behavior, nor how those stresses may be transmitted to the substrate to enact locomotion. We will address this shortcoming through the use of various mathematical models of *physarum*. The main goal of this work is to more quantitatively elucidate the mechanisms by which *physarum* microplasmodium migrate while generating the observed flows of cytoplasm.

First, we will provide a mathematical investigation into the plausibility of the description of motility in *physarum* provided in [Mat08]. Can hydrodynamic effects alone explain the motion of *physarum* microplasmodia? This is addressed in Chapter 2, where we model a single microplasmodia as a peristaltic chamber of cytoplasmic fluid. We quantify the phase relationships between contraction and flow that necessarily result from driving cytoplasmic flow through traveling waves of contraction. These phase relationships are qualitatively compared to those observed in [Mat08]. Simultaneously, we quantify the characteristic stresses associated with the flows predicted by our model. These stresses are found to be of a biologically relevant scale, though on average rather small.

We then develop a more complex model of *physarum* plasmodium that is easily amenable to computational exploration. This model includes a description of the mechanical structure of the cell interior (cytoskeleton), as well as adhesive interactions with the substrate. The cytoskeleton is modeled as a porous, elastic meshwork permeated by viscous cytosol. Adhesive interactions are described via a modulated viscous drag with the substrate. Chapter 3 contains a detailed derivation of the modeling framework and the numerical methods used in simulation. In Chapter 4, we use the model to simulate crawling *physarum* plasmodia. We then analyze the flow patterns generated within the cell and the stresses applied to the substrate by the crawling cell. The model predictions are compared to experimental measurements obtained by our collaborators using live *physarum*. We identify parameter regimes that give model predictions that most closely reproduce experimental measurements. Migration in these parameter ranges is shown to be extremely efficient and robust.

Chapter 2

Peristaltic Flow Within *Physarum*

2.1 Introduction

We begin by developing a hydrodynamic model of the behavior observed in migrating *physarum* plasmodium. We will use this model to address one of the main hypotheses put forward in [Mat08]. In [Mat08], the authors noted a particular correlation between the deformation of the cell boundary and the flow of cytoplasm along the cell interior. Both phenomena propagate along the cell axis from posterior to anterior. Moreover, there is a similar period of the two waves, and they appear to have a well defined timing relative to one another. This particular relative phase was postulated to be at least partially responsible for translation of the center of mass of the plasmodium (discussed in more detail in Section 2.7). One goal of our modeling work is to investigate the validity of this hypothesis. Concurrently, we attempt to quantify the stresses generated by the observed deformations and flows. In order to enact motility, the plasmodium must exert stresses on the substrate that it migrates across. We quantify stresses associated with the flows predicted by our model to explore the possibility that hydrodynamic effects may be used to generate the forces that drive the cell across the substrate. With this in mind, we model the cell as a microscopic peristaltic pump.

The cellular contractions observed and measured in [Mat08] bear a stark similarity to the deformations seen in peristalsis. Peristalsis is a phenomenon whereby waves of contraction propagate along the exterior of a fluid-filled tube or chamber. When these waves of contraction result in net transport of fluid along the axis of the tube, it is referred to as a peristaltic pump. Peristaltic pumping is observed in numerous physiological contexts where tubular smooth muscle structures are common. The gastrointestinal tract, bile duct, and fallopian tubes all engage in peristaltic pumping. Peristalsis also has applications in industrial processes, where a peristaltic pump can be used to move slurries and corrosive materials without the liquid coming into contact with any mechanical parts of the device. However, the notion that a cell may peristaltically "pump" itself across a substrate is a here-to-fore novel concept.

Mathematical analysis of motility using traveling waves dates back as far as [Tay51], where peristaltic-like waves of deformation were studied as a propulsive mechanism for microscopic swimmers. Later, the efficiency of peristalsis as a pumping mechanism became the subject of much investigation. Most studies were asymptotic and applicable to restricted parameter regimes. Zero Reynolds number and infinite wave length were assumed in [Sha69], while vanishingly small boundary deformations were assumed in [Fun68]. A review of much of the early work on this subject may be found in [Jaf71]. The main quantity of interest in these works is usually the volume of fluid that the pump may transport, or alternately, the pressure gradient that the pump is capable of overcoming. Later, numerical techniques were brought to bear on the problem. In [Poz87], a boundary integral method is used to investigate a wider variety of deformations (including non-symmetric contraction of the pump walls). In [Fau92], the Immersed Boundary (IB) method is used to investigate the transport of solid objects within a peristaltic pump, such as in the fallopian tract. With more sophisticated numerical methods, elastic effects were added to problem. In [Car97] the authors model the boundary of a peristaltic pump as a contractile elastic medium to more closely approximate smooth muscle in the ureter. In [Ter08], pumping of visco-elastic fluids was simulated. Critically, all of these investigations assume a peristaltic pump of infinite length (or approximate one using a periodic domain).

The assumption of an infinitely long tube is not appropriate in the context of the system we are modelling. The characteristic length (400 μm) of the *physarum* plasmodium in [Mat08] is significantly longer than the characteristic width (50 μm) or thickness (20 μm). However, it is not clear that the length may safely be regarded as infinite. Moreover, the cell is fundamentally a closed system. The cell membrane segregates the intracellular fluid from the extracellular space, and therefore, the peristaltic "pump" may not transport fluid in the traditional sense. We must take into account the "ends" of the pump at the anterior and posterior of the cell, and thus we will be modeling peristalsis in a finite domain. Investigations into finite length peristalsis are relatively new. The mechanics of peristaltically pumping fluid over a finite distance (from one reservoir to another) was explored in [Li93]. More recently, the effects of peristaltic motion of the walls has been investigated in the context of closed, microfluidic devices [Sel01]. In this work, the authors investigate peristaltic flow in the high Womersley number regime (that is, a regime where inertial effects dominate), and are concerned mostly with the mixing properties of the induced flow. This approximation is not relevant to the length and timescales of interest in our problem, and we are not concerned with mixing properties. However, peristaltic mixing *has* been studied in the context of *physarum* plasmodium, using a discrete chamber model [Iim12]. The existing investigation that most closely matches the model we will develop may be found in [Yi02], where the authors asymptotically calculate the flow profile in a finite length chamber under the assumption of small boundary deformation. This is an approximation we will also make. However, the authors in [Yi02] do not address the potential phase relationships between deformation and flow, nor do they attempt to quantify the associated fluid stresses.

We will now develop a model of a migrating *physarum* plasmodium, which we treat as a chamber undergoing peristaltic deformations. We will quantify the flow driven by various deformations of the chamber wall, as well as the stresses associated with those flows. This is done to investigate the plausibility of peristaltic pumping as a mechanism to generate the forces necessary for cell motility. Moreover, we explore the fundamental asymmetries which aid in this form of locomotion. One asymmetry is immediately apparent: the directionality of the peristaltic wave. However, it is not immediately clear if this is sufficient to drive motility in a non-inertial regime. Finally, we will investigate the origin of the phase relationship (between deformation and flow) noted in [Mat08], as the authors suggest that it is a primary generator of net mass transport.

2.2 Dimension Reduction

We begin by treating the cell interior as a microscopic chamber that is filled with incompressible Newtonian fluid. Let the fluid domain be defined by $0 \leq x \leq L_x$, $-h(x,t) \leq y \leq h(x,t)$, and $-d/2 \leq z \leq d/2$. The half width of the domain is given by the periodic function $h(x,t)$, which we will *prescribe* to drive the flow (more on this in later sections). Figure 2.1 shows an illustrative example of the intracellular space that is filled with fluid. Within the chamber, we assume that inertial effects are negligible, and therefore the force density balance on the fluid is given by Stokes equation:

$$\mu \Delta \boldsymbol{u} - \nabla p = 0. \tag{2.1}$$

Here $\boldsymbol{u}$ is the fluid velocity field in the cell chamber, μ is the dynamic viscosity of the fluid, and p is the hydrodynamic pressure. We note that in the experiments of [Mat08] the characteristic height (from the basal to dorsal surface of the cell) is roughly $d \approx 20$ µm. This is slightly less than the characteristic width of the fluid domain ($\ell \approx 40$ µm), and both are significantly less than the length of the fluid domain ($L_x \approx 400$ µm). Therefore, we make a thin gap approximation to the momentum equation of Newtonian fluid [Ach90]. We assume a characteristic flow velocity scale U and see that the terms of $\mu\Delta\boldsymbol{u}$ scale like

$$\mu\Delta\boldsymbol{u} = \mu\left(\frac{\partial^2\boldsymbol{u}}{\partial x^2} + \frac{\partial^2\boldsymbol{u}}{\partial y^2} + \frac{\partial^2\boldsymbol{u}}{\partial z^2}\right) \sim \frac{\mu U}{L_x^2} + \frac{\mu U}{\ell^2} + \frac{\mu U}{d^2}. \tag{2.2}$$

Since d is the smallest length scale in the problem, the third term above will dominate, and we therefore approximate

$$\mu\Delta\boldsymbol{u} \approx \mu\frac{\partial^2\boldsymbol{u}}{\partial z^2}. \tag{2.3}$$

Note that to justify our choice to ignore the second term in Equation (2.2) we do not require that $d << \ell$, but rather that $d^2 << \ell^2$. This is reasonable for the scales in our problem. Therefore the momentum equation may be reduced to the following balance of viscous force densities and pressure:

$$\frac{\partial p}{\partial x} = \mu\frac{\partial^2 u}{\partial z^2}, \tag{2.4}$$

$$\frac{\partial p}{\partial y} = \mu\frac{\partial^2 v}{\partial z^2}, \tag{2.5}$$

$$\frac{\partial p}{\partial z} = \mu\frac{\partial^2 w}{\partial z^2}, \tag{2.6}$$

where $\boldsymbol{u} = (u, v, w)$. We still have the incompressibility constraint

$$\frac{\partial u}{\partial x} + \frac{\partial v}{\partial y} + \frac{\partial w}{\partial z} = 0. \tag{2.7}$$

Since the first term of Equation (2.7) scales as U/L_x, the other two must as well. From this we can deduce the scaling $v \sim U\ell/L_x$ and $w \sim Ud/L_x$, which implies that the flow in the y- and z-directions is much smaller than that in the x-direction. Returning to Equations (2.4)–(2.6), this allows us to deduce the scaling of the pressure gradient

$$\left(\frac{\partial p}{\partial x}, \frac{\partial p}{\partial y}, \frac{\partial p}{\partial z}\right) \sim \frac{U}{d^2}\left(1, \frac{\ell}{L_x}, \frac{d}{L_x}\right). \tag{2.8}$$

Clearly, the second and third terms are much smaller than the first. Therefore, as a first approximation we may assume that the pressure is a function of x only. Considering only flow in the x-direction (for now), we return to the relation

$$\mu\frac{\partial^2 u}{\partial z^2} = \frac{\partial p}{\partial x}. \tag{2.9}$$

Since p is assumed to not be a function of z, this is easily solvable. Integrating twice and imposing a no-slip boundary condition on the basal and dorsal surfaces of the fluid domain ($z = \pm d/2$), we solve for the flow profile as a function of z:

$$u(z) = \frac{p_x}{8\mu}\left(d^2 - 4z^2\right). \tag{2.10}$$

This is simply the standard Poiseuille flow profile [Poi46]. Now, we can utilize this flow profile to evaluate the viscous stress applied by the flow to the basal surface of the cell

$$\sigma = \mu \left.\frac{\partial u}{\partial z}\right|_{z=-\frac{d}{2}} = -\frac{p_x d}{2}. \tag{2.11}$$

We will utilize this expression later when we address the characteristic stresses associated with the flow within the cell. Finally, note that most experiments performed on *physarum* measure the intracellular velocity in the xy-plane. Therefore, we make the simplifying assumption that the experimentally measured velocity can be characterized by the *average* velocity over the height of the cell. We calculate this mean velocity as

$$\bar{u} = \frac{1}{d}\int_{\frac{-d}{2}}^{\frac{d}{2}} u(z)\,dz = \frac{-p_x d^2}{12\mu}. \tag{2.12}$$

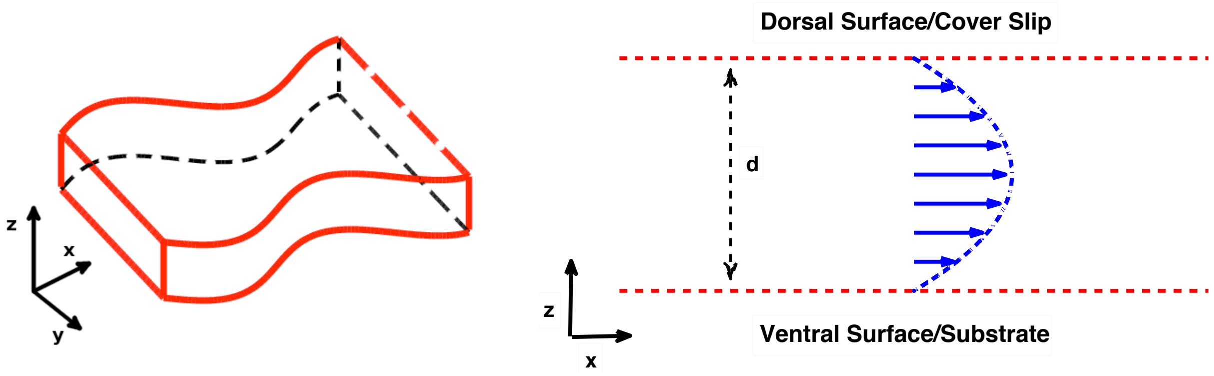

(a) Schematic of the peristaltic chamber. (b) Side view of peristaltic chamber with Poiseille flow profile.

Figure 2.1: A schematic of the geometry for our model. The chamber is assumed to be of uniform thickness (d) in the z-direction. The longitudinal flow profile in this direction is assumed to be a parabolic Poiseuille flow.

For the remainder of this section, we will only be concerned with the two-dimensional, planar flow within the cell chamber. Therefore, we will drop the "bar" notation and refer to the mean velocity in the longitudinal direction as u. Similarly, v will denote the average velocity in the lateral (y-) direction. However, this should be understood to imply that the flow has already been averaged over the z-coordinate.

We now address the flux of fluid in the longitudinal direction. We define the quantity

$$Q(x,t) = \int_{-h}^{h} u\,dy. \tag{2.13}$$

This quantity does not correspond to the traditional notion of volumetric flux. In our model, Q has units of *area per time*, as opposed to volume per time. However, it is our chosen quantity of interest and will be referred to as “flux” from this point forth.

We now directly calculate the flux from the longitudinal fluid velocity u. In order to do this, we make use of our earlier approximations. Since the pressure is assumed to not be a function of y, Equation (2.4) shows that the velocity u is not either. This leads us to a uniform flow profile in the y-direction. This assumption, coupled with Equation (2.12), leads to

$$u(y,x) = u(x) = \frac{-p_x d^2}{12\mu}. \tag{2.14}$$

Integrating to find the flux immediately gives

$$Q(x) = \int_{-h}^{h} u(x)\,dy = 2hu(x) = \frac{-p_x h d^2}{6\mu}. \tag{2.15}$$

It should be noted that our assumption of uniform flow in the y-direction is not particularly critical to the above relationship. The uniform profile in y is obviously a crude approximation and indeed does not even satisfy a no-slip boundary condition at $y = \pm h$. We *could* perform another lubrication approximation on the two-dimensional flow to account for variations in the y-direction. This would yield that u has a Poiseuille flow profile in the y-direction. If the magnitude of this Poiseuille flow is given by Equation (2.12), then we may write

$$u(x,y) = \frac{-p_x(x) d^2}{12\mu}\left(1 - \left(\frac{y}{h}\right)^2\right). \tag{2.16}$$

Integrating over a chamber cross section gives

$$Q(x) = \int_{-h}^{h} u(x,y)\,dy = \frac{-p_x h d^2}{9\mu}. \tag{2.17}$$

Thus we see that the precise assumption regarding the flow profile in the y-direction is not critical, as its effect on the calculated flux simply amounts to an order one constant. This calculation is purely expository. For the duration of Chapter 2, we will assume that the flow profile is uniform in the y-direction, and thus the flux $Q(x)$ is given by Equation (2.15). Combining Equations (2.11) & (2.15), we can relate the flux Q

and boundary deformation h to the characteristic viscous stresses associated with the flow

$$\sigma = \frac{3\mu}{d}\frac{Q(x,t)}{h(x,t)}. \tag{2.18}$$

Now, all that remains is to determine the flux of fluid driven by the boundary deformation.

2.3 Relating Deformation and Flux

Assuming that the two-dimensional flow field (in the xy-plane) is incompressible, we have

$$\nabla \cdot \boldsymbol{u} = \nabla \cdot \begin{bmatrix} u \\ v \end{bmatrix} = u_x + v_y = 0. \tag{2.19}$$

This equation is obviously an approximation, as we have averaged an incompressible fluid over the z-direction. However, in experiments, *physarum* are seen to change area in the xy-plane by no more than approximately 5% [Zha13]. This implies that the planar flow field is *nearly* incompressible. Integrating over the width of the domain, we have

$$\begin{aligned} 0 &= \int_{-h}^{h} (u_x + v_y)\, dy \\ &= \frac{\partial}{\partial x}\int_{-h}^{h} u\, dy - \left(u|_{y=h} + u|_{y=-h} \right)\frac{\partial h}{\partial x} + \int_{-h}^{h} v_y\, dy \\ &\approx \frac{\partial}{\partial x}\int_{-h}^{h} u\, dy + \int_{-h}^{h} v_y\, dy \\ &= \frac{\partial}{\partial x} Q(x,t) + v|_{y=-h}^{y=h} \\ &= Q_x(x,t) + v(h(x,t),t) - v(-h(x,t),t) \\ &= Q_x(x,t) + 2h_t(x,t). \end{aligned} \tag{2.20}$$

Where again, $Q(x,t)$ is the fluid flux through a cross section of the domain. We have made use of the fact that $v(h) = h_t$ and $v(-h) = -h_t$ (which derives from a no slip boundary condition). We have also assumed that $|h_x| << 1$, in order to ignore the boundary terms from the Leibniz integration rule. This is equivalent to an assumption that the wavelength of the deformation is long compared to the width of the cell. As we will see, the wavelength of the deformation is on the order of 1600 µm, while the cell width is on the order of 50 µm. Notice that Equation (2.20) requires very few assumptions about the fluid in question. We have simply integrated the incompressibility constraint.

Now we have a one-dimensional partial differential equation (PDE) that is defined on the interval $0 < x < L_x$ for time $t > 0$. Given a boundary function $h(x,t)$, Equation (2.20) determines the associated flux of fluid within the chamber. However, we still require the appropriate boundary conditions to close the system. Given that *physarum* is enclosed by an impermeable bilipid membrane, one might assume that no-slip boundary conditions for the fluid should be imposed at both $x = 0$ and $x = L_x$. We note that no-slip boundary conditions for the fluid result in homogeneous Dirichlet boundary conditions for the flux ($Q = 0$). However, Equation (2.20) is a *first order* differential equation for Q. This implies that imposing boundary conditions at both ends of the domain over-determines the system, and we are left with a constrained problem. In light of this fact, it is perhaps not immediately clear what boundary conditions are appropriate for Equation (2.20). This will be discussed further in the following sections.

2.4 Boundary Deformations

We now impose a boundary deformation which mimics the peristaltic contractions observed to propagate down the lateral sides of migrating *physarum* specimens. Experimental measurements have shown that the cell membrane deformations appear to be a traveling, periodic function (phase wave), which propagates from the posterior to the anterior end of the cell [MAT08, ZHA13]. These wave-like contractions travel with a distinct velocity, which we refer to as the phase velocity.

2.4.1 Unconstrained Deformation

As a first approximation, we idealize the boundary deformation as a traveling sinusoid of the form

$$h(x,t) = h_0 + A\cos\left(k\frac{x}{L_x} - \omega t\right), \tag{2.21}$$

with the stipulation that $k \neq 0$. We refer to k as the wave number of the deformation, and thus the wavelength is given by $\lambda = 2\pi L_x/k$. Similarly, ω is the frequency of the wave, and the period is given by $T = 2\pi/\omega$. The ratio $\omega L_x/k$ gives the phase velocity and has units of length per time. Intuitively, this can be thought of as the velocity with which the peak (or any point of given phase) of the sinusoid travels in the spatial coordinate. Now, given our assumed form of the chamber wall deformation, a simple calculation shows that

$$h_t = \omega A \sin\left(k\frac{x}{L_x} - \omega t\right). \tag{2.22}$$

From Equation (2.20) we calculate

$$Q_x = -2\omega A \sin\left(k\frac{x}{L_x} - \omega t\right). \tag{2.23}$$

Integrating gives

$$Q(x,t) = \frac{2AL_x\omega}{k}\sin\left(k\frac{x}{L_x} - \omega t\right) + C(t), \tag{2.24}$$

where $C(t)$ is a spatially *independent* function of integration determined by the boundary conditions. We make the assumption that the domain is "closed" at the left end ($x = 0$) and impose a no flux condition $Q(0,t) = 0$. This is analogous to the assumption that fluid may not pass through the cell membrane at the posterior end of the chamber. However, we have made no assumptions about the behavior of the model at the anterior end of the chamber. Indeed, fluid is free to flow in and out of the "head" at $x = L_x$, resulting in a very clear asymmetry in the domain. We will return to this idea in the following section. Imposing the boundary condition and a brief calculation gives that

$$C(t) = \frac{-2AL_x\omega}{k}\cos\left(\omega t\right), \tag{2.25}$$

and therefore the resulting solution to Equation (2.20) is

$$Q(x,t) = \frac{2AL_x\omega}{k}\left(\cos\left(k\frac{x}{L_x} - \omega t\right) - \cos\left(\omega t\right)\right). \tag{2.26}$$

Finally, we define the displacement of the chamber wall as

$$\bar{h}(x,t) = h(x,t) - h_0 = A\cos\left(k\frac{x}{L_x} - \omega t\right). \tag{2.27}$$

We may regard the displacement $\bar{h}$ as the input of the model, while the resulting flux Q may be thought of as the output.

2.4.2 Volume Preserving Deformation

We now return to the previous discussion of what boundary conditions are appropriate to impose on Equation (2.20). In the previous section, we stipulated a zero flux boundary condition at the left ($x = 0$) boundary of the chamber only. This allows a free flow of fluid in and out of the right boundary ($x = L_x$). However, if we consider the physical system we are modeling, it is obvious that cytoplasm cannot flow freely through the anterior end of the cell membrane. We may therefore choose to impose another no flux boundary condition at the right boundary. Doing so over-determines the problem, as previously stated. The consequence of this is a constraint on the allowable deformations $h(x,t)$. Zero flux through both domain boundaries implies overall volume conservation of the chamber. Thus, for the system to have a solution, the deformation must be consistent with volume conservation.

The space of deformations which satisfy this constraint is far too large to explore fully. Therefore we make the following assumption: The chamber boundary has a "preferred" deformation which is the same as in the previous section (Equation (2.21)); However, there is a spatially uniform correction term which is calculated to impose constant volume on the chamber,

$$h(x,t) = h_0 + A\cos\left(k\frac{x}{L_x} - \omega t\right) + D(t). \tag{2.28}$$

The correction term D is determined by integrating over the chamber to determine the overall chamber volume as a function of time.

$$\begin{aligned}
V(t) &= \int\limits_{\Omega} 1\,dy\,dx \\
&= \int\limits_{0}^{L_x}\int\limits_{-h}^{h} 1\,dy\,dx \\
&= 2\int\limits_{0}^{L_x} h(x,t)\,dx \\
&= 2\int\limits_{0}^{L_x} \left(h_0 + A\cos\left(k\frac{x}{L_x} - \omega t\right) + D(t)\right)dx \\
&= 2\left(h_0 L_x + \frac{AL_x}{k}\sin\left(k\frac{x}{L_x} - \omega t\right)\Bigg|_{x=0}^{L_x} + L_x D(t)\right) \\
&= 2h_0 L_x + 2L_x D(t) + \frac{2AL_x}{k}\left(\sin\left(k - \omega t\right) - \sin\left(-\omega t\right)\right) \\
&= 2h_0 L_x + 2L_x D(t) + \frac{2AL_x}{k}\left(\sin\left(k - \omega t\right) + \sin\left(\omega t\right)\right).
\end{aligned} \tag{2.29}$$

Now, we impose the constraint that $V(t) = V(0) = 2h_0 L_x$. This allows us to calculate the correction term

$$D(t) = -\frac{A}{k}\left(\sin\left(k - \omega t\right) + \sin\left(\omega t\right)\right). \tag{2.30}$$

We now have the fully determined, volume preserving deformation

$$h(x,t) = h_0 + A\cos\left(k\frac{x}{L_x} - \omega t\right) - \frac{A}{k}\left(\sin\left(k - \omega t\right) + \sin\left(\omega t\right)\right). \tag{2.31}$$

We proceed as in the previous section. Taking the time derivative of Equation (2.31) gives

$$h_t = -\omega A \cos\left(k\frac{x}{L_x} - \omega t\right) - \frac{A\omega}{k}\left(\cos(\omega t) - \cos(k - \omega t)\right). \tag{2.32}$$

Substituting into Equation (2.20) and integrating with respect to x gives

$$Q(x,t) = \frac{2\omega A L_x}{k}\cos\left(k\frac{x}{L_x} - \omega t\right) + \frac{A\omega x}{k}\left(\cos(\omega t) - \cos(k - \omega t)\right) + F(t), \tag{2.33}$$

where $F(t)$ is a constant of integration that will be determined by boundary conditions. Here, we impose *only* the boundary condition that $Q(0,t) = 0$. This gives

$$Q(0,t) = \frac{2\omega A L_x}{k}\cos(-\omega t) + F(t) = 0, \tag{2.34}$$

which can readily be solved to obtain

$$F(t) = \frac{-2\omega A L_x}{k}\cos(-\omega t). \tag{2.35}$$

This gives the complete description of the flux function

$$Q(x,t) = \frac{2\omega A L_x}{k}\left(\cos\left(k\frac{x}{L_x} - \omega t\right) - \cos(\omega t)\right) + \frac{2A\omega x}{k}\big(\cos(\omega t) - \cos(k - \omega t)\big). \tag{2.36}$$

Notice here that evaluating the flux at the right domain endpoint ($x = L_x$) gives

$$Q(L_x,t) = \frac{2\omega A L_x}{k}\big(\cos(k - \omega t) - \cos(\omega t) + \cos(\omega t) - \cos(k - \omega t)\big) = 0. \tag{2.37}$$

Thus, the no flux boundary condition is automatically satisfied at the right end of the domain, due to the constraint imposed on the deformation h. Again, we specifically call attention to the *displacement* of the chamber wall

$$\bar{h}(x,t) = h(x,t) - h_0 = A\cos\left(k\frac{x}{L_x} - \omega t\right) - \frac{A}{k}\left(\sin(k - \omega t) + \sin(\omega t)\right), \tag{2.38}$$

which we regard as the input which generates an output of flux given by Equation (2.36).

2.5 Stress Generation

We now address the issue of the stresses associated with the flux generated by the flow of cytoplasm. In order to migrate, it is necessary for a cell such as *physarum* to generate stresses internally and transmit them to the underlying substrate in a coordinated fashion. Our goal is to quantify the stresses that are a generated via the peristaltic pumping of intracellular fluid observed in experiments. Recall from Equation (2.18) that the viscous stress on the basal surface of the chamber is given by the non-linear relationship

$$\sigma = \frac{3\mu Q(x,t)}{h(x,t)d}. \tag{2.39}$$

From the preceding sections, we have proposed to two idealized deformation functions (Equations (2.21) & (2.31)) and calculated the flux of intracellular fluid that results (Equations (2.26) & (2.36)).

2.5.1 Unconstrained Deformation

In the case of the unconstrained deformation, where fluid may flow freely through the head of the domain, we rewrite the deformation as

$$h(x,t) = h_0\left(1 + \frac{A}{h_0}\cos\left(k\frac{x}{L_x} - \omega t\right)\right) = h_0\left(1 + \left(\frac{A}{h_0}\right)h_1(x,t)\right). \tag{2.40}$$

Again, h_0 is the resting half width of the chamber, while A is the amplitude of the displacement wave. In *physarum* specimens observed in [Mat08], the average width of the cell is approximately 40 μm, while the amplitude of deformation is approximately one fourth of that (10 μm). This allows us to estimate the non-dimensional amplitude of deformation $A/h_0 \approx 1/4$. We now define the parameter

$$\varepsilon := \frac{A}{h_0}, \tag{2.41}$$

and make the assumption that $\varepsilon << 1$. Noticing that the function h_1 is order one, we make use of the asymptotic expansion $1/\left(1+\epsilon\right) = 1 - \epsilon + \mathcal{O}\left(\epsilon^2\right)$. We then approximate

$$\frac{1}{h} = \frac{1}{h_0\left(1 + \varepsilon h_1(x,t)\right)} \approx \frac{1}{h_0}\left(1 - \varepsilon h_1(x,t)\right). \tag{2.42}$$

This gives us an asymptotic approximation of the basal viscous stress due to flow of fluid within the cell

$$\sigma = \frac{3\mu Q}{dh_0\left(1+\varepsilon h_1\right)} \approx \frac{6\mu A L_x \omega}{dkh_0}\Bigg(\Big(\cos\left(kx - \omega t\right) - \cos\left(\omega t\right)\Big)\Big(1 - \varepsilon\cos\left(kx - \omega t\right)\Big)\Bigg). \tag{2.43}$$

Expanding Equation (2.43), we arrive at the following expression:

$$\sigma = \frac{6\mu\varepsilon\omega L_x}{dk}\Bigg[\underbrace{\cos\left(k\frac{x}{L_x} - \omega t\right) - \cos\left(\omega t\right)}_{\text{T1}} - \underbrace{\varepsilon\Big(\cos^2\left(k\frac{x}{L_x} - \omega t\right) - \cos\left(k\frac{x}{L_x} - \omega t\right)\cos\left(\omega t\right)\Big)}_{\text{T2}}\Bigg]. \tag{2.44}$$

The stress σ is comprised of two distinct functional forms that have been labeled Terms T1 & T2. Term T1 is comprised of two pure sinusoids. If we were to integrate over one period of the wave, the stress contributed by Term T1 would be zero. That is to say, the stresses directed forward, and those directed backwards would cancel over one period of the wave. Conversely, Term T2 is comprised of two *products* of sinusoids (with the same period). This means that the full stress σ does have non-zero average, but only Term T2 contributes to this average. Furthermore, we see that while Term T1 is $\mathcal{O}\left(\varepsilon^0\right)$, Term T2 is $\mathcal{O}\left(\varepsilon\right)$. This means that for $\varepsilon << 1$, Term T1 will give a good approximation to the characteristic scale of the stress σ, while Term T2 gives the average stress over each period of the wave.

We now calculate the characteristic scale of *average* stress associated with the flow wave. The period averaged basal viscous stress is give by

$$\langle\sigma\rangle := \frac{\omega}{2\pi}\int_0^{\frac{2\pi}{\omega}} \sigma\, dt = \frac{3\varepsilon^2\mu\omega L_x}{4kd\pi}\left(2\sin\left(k\frac{x}{L_x}\right)\cos\left(k\frac{x}{L_x}\right)+4\pi\cos\left(k\frac{x}{L_x}\right)-\sin\left(2k\frac{x}{L_x}\right)-4\pi\right). \tag{2.45}$$

From Equation (2.45), we can calculate the "total average" (that is, a temporal and spatial average) viscous stress

$$\langle\overline{\sigma}\rangle := \frac{1}{L_x}\int_0^{L_x}\langle\sigma\rangle\, dx = \frac{3\varepsilon^2\mu\omega L_x}{d}\frac{\left(\sin\left(k\right)-k\right)}{k^2}. \tag{2.46}$$

Notice that $\langle\overline{\sigma}\rangle$ indeed has units of stress; We will return to discuss the scale of this term in Section 2.6. We use this quantity as a measure of the average imbalance of stresses (over one period of the wave) associated with the flow of cytoplasm. As currently developed, the model does not address how these stresses may be transmitted to the substrate (that will be addressed in later chapters). However, at this point $\langle\overline{\sigma}\rangle$ represents the only component of the model that is not perfectly symmetric in time. Both the flux of fluid (Q) and the imposed deformation ($\bar{h}$) have zero average over one period of the wave (for both the free and constrained deformation). However, at second order in ε, we see that there is non-zero average stress associated with the flow, which may be used to enact motility.

We now return to Term T1 and address the issue of the relative scale of the stresses generated by the flow of fluid. As previously mentioned, Term T2 is of a higher order in ε, therefore we make the approximation that the size of the stress may be reasonably approximated by the size of Term T1. We define

$$\sigma_{\text{size}} := \frac{6\mu\varepsilon\omega L_x}{dk}\left(\cos\left(k\frac{x}{L_x}-\omega t\right)-\cos\left(\omega t\right)\right), \tag{2.47}$$

and note that $\sigma_{\text{size}} \approx \sigma$ to leading order in ε. We again integrate over the domain to find the "spatial average stress" associated with the wave,

$$\overline{\sigma}_{\text{size}} := \frac{1}{L_x}\int_0^{L_x} \sigma_{\text{size}}\, dx = \frac{6\mu\varepsilon\omega L_x}{d}\frac{\left(\sin(\omega t) + \sin(k - \omega t) - \cos(\omega t)\right)}{k^2}. \tag{2.48}$$

As we have already mentioned, over one period, this function has zero mean. However, we may still quantify the characteristic magnitude of stresses by maximizing this (continuous) function on the domain $0 \le t \le 2\pi/\omega$. A calculation yields the critical points of $\overline{\sigma}_{\text{size}}$ are given by

$$t^* = \frac{-1}{\omega}\arctan\left(\frac{-1+\cos(k)}{\sin(k) - k}\right). \tag{2.49}$$

Since we only consider $k > 0$ (forward traveling waves), the argument of the $\arctan$ function is restricted to the interval $[0, \infty)$. There are two branches of the $\arctan$ function which yield values of t^* in the interval $[0, 2\pi/\omega]$ (that is, there are two critical points each period of the wave). However, the choice of branch does not change our calculations (as we will be considering the absolute value of $\overline{\sigma}_{\text{size}}$). For this reason, we will only consider the value t^* produces by the primary branch of $\arctan$. Finally, we may define the "maximum average" (that is, averaged in space and maximized in time) stress due to the fluid flow

$$\begin{aligned}\overline{\sigma}_{\max} := |\overline{\sigma}_{\text{size}}(t^*)| = \frac{6\mu\varepsilon\omega L_x}{dk^2}\Bigg| &\sin\left(-\arctan\left(\frac{-1+\cos(k)}{\sin(k)-k}\right)\right) \\ &+ \sin\left(k + \arctan\left(\frac{-1+\cos(k)}{\sin(k)-k}\right)\right) - \cos\left(-\arctan\left(\frac{-1+\cos(k)}{\sin(k)-k}\right)\right)\Bigg|.\end{aligned} \tag{2.50}$$

We now make use of the fact that the maximum average stress may be written in the form

$$\overline{\sigma}_{\max} = \frac{3\mu\omega L_x}{d}\varepsilon f(k). \tag{2.51}$$

Likewise, the total average stress may be written as

$$\langle\overline{\sigma}\rangle = \frac{3\mu\omega}{d}\varepsilon^2 g(k). \tag{2.52}$$

We define the function

$$r(k) := \frac{\langle\overline{\sigma}\rangle}{\varepsilon\,|\overline{\sigma}_{\max}|} = \frac{g(k)}{f(k)}. \tag{2.53}$$

The quantity ϵr is called the "effective stress." Up to a constant ($C = 3\mu\omega L_x/d$), the non-dimensional functions f and g characterize the maximum and total average stresses that are generated each period of the wave. The quantity ϵr is the proportion of the maximum stresses that have non-zero average, and thus have a directionality that may theoretically be harnessed in order to enable motility. Figure 2.2a shows graphs of f, g, and r for values of k in the interval $[0, 2\pi]$. This interval of k corresponds to waves ranging from those with infinite wavelength (spatially homogeneous) to those with a wavelength equal to the cell body length. Before commenting on the stresses generated by this deformation, we will derive the equivalent expressions in the case of the constrained, volume preserving deformation.

2.5.2 Constrained Deformation

We now return to the constrained deformation, which was derived in Section 2.4.2. Recall that the deformation function is given by

$$h(x,t) = h_0\left(1 + \frac{A}{h_0}\left(\cos\left(k\frac{x}{L_x} - \omega t\right) - \frac{1}{k}\big(\sin(k - \omega t) + \sin(\omega t)\big)\right)\right), \tag{2.54}$$

which we rewrite as

$$h(x,t) = h_0\left(1 + \left(\frac{A}{h_0}\right)h_2(x,t)\right). \tag{2.55}$$

Proceeding exactly as before, we asymptotically expand in the limit of small $\varepsilon := A/h_0$,

$$\frac{1}{h} = \frac{1}{h_0\left(1 + \varepsilon h_2(x,t)\right)} \approx \frac{1}{h_0}\left(1 - \varepsilon h_2(x,t)\right). \tag{2.56}$$

We pause here to clarify that the functional form of h_2 is given by

$$h_2(x,t) = \cos\left(k\frac{x}{L_x} - \omega t\right) - \frac{1}{k}\big(\sin(k - \omega t) + \sin(\omega t)\big). \tag{2.57}$$

This means that in the limit $k << 1$, the product εh_2 is no longer small when compared to 1, and our expansion in Equation (2.56) is no longer valid. However, as will be discussed later, we are not concerned with the limit $k << 1$, as these values are not compatible with the wavelength of deformation seen in migrating *physarum*.

Having made this expansion of the inverse of the deformation function h, we can approximate the basal viscous stress associated with flows driven by the volume preserving deformation. We have

$$\begin{aligned}\sigma = \frac{3\mu Q}{dh_0\left(1 + \varepsilon h_2\right)} \approx \frac{6\mu A\omega L_x}{dkh_0}\Bigg[&\left(\cos\left(k\frac{x}{L_x} - \omega t\right) - \cos(\omega t) - x\big(\cos(k - \omega t) - \cos(\omega t)\big)\right)\\ &\times\left(1 - \varepsilon\cos\left(k\frac{x}{L_x} - \omega t\right) + \frac{\varepsilon}{k}\big(\sin(k - \omega t) + \sin(\omega t)\big)\right)\Bigg].\end{aligned} \tag{2.58}$$

Expanding and collecting terms by order in ε, we have

$$\begin{aligned}\sigma = \frac{6\mu\varepsilon\omega L_x}{dk}\Bigg[& \underbrace{\cos\left(k\frac{x}{L_x}-\omega t\right)-\cos(\omega t)-x\big(\cos(k-\omega t)-\cos(\omega t)\big)}_{\text{T3}} \\ & \underbrace{\begin{aligned} +\,\varepsilon\Bigg(& \cos\left(k\frac{x}{L_x}-\omega t\right)\times\left(\cos(\omega t)+x\cos(k-\omega t)\ -\cos\left(k\frac{x}{L_x}-\omega t\right)-x\cos(\omega t)\right) \\ & -\frac{\sin(k-\omega t)}{k}\times\left(\cos(\omega t)+x\cos(k-\omega t)\ -\cos\left(k\frac{x}{L_x}-\omega t\right)-x\cos(\omega t)\right) \\ & \quad -\frac{\sin(\omega t)}{k}\times\left(\cos(\omega t)+x\cos(k-\omega t)\ -\cos\left(k\frac{x}{L_x}-\omega t\right)-x\cos(\omega t)\right)\Bigg)\end{aligned}}_{\text{T4}}\Bigg].\end{aligned} \tag{2.59}$$

Again, we see a structure similar to the case of of the unconstrained deformation. Term T3 has zero mean over one period of the wave, but is a lower order in ε and thus dominates the magnitude of the stress σ. Meanwhile, Term T4 is a product of sinusoids and thus has non-zero mean, while being smaller in magnitude due to the higher order in ε.

As in the case of the unconstrained deformation, we calculate the total average stress as

$$\langle\overline{\sigma}\rangle = \frac{\omega}{2\pi L_x}\int_0^{L_x}\int_0^{\frac{2\pi}{\omega}} \sigma\, dt\, dx = \frac{3\mu\varepsilon^2\omega L_x}{d}\left(\frac{4-4\cos(k)-k\sin(k)-k^2}{k^3}\right). \tag{2.60}$$

Again, we approximate the magnitude of the stress using Term T3 as

$$\sigma_{\text{size}} = \frac{6\mu\varepsilon\omega L_x}{dk}\left(\cos\left(k\frac{x}{L_x}-\omega t\right)-\cos(\omega t)-x\big(\cos(k-\omega t)-\cos(\omega t)\big)\right). \tag{2.61}$$

This allows us to approximate the spatial average stress

$$\overline{\sigma}_{\text{size}} = \frac{1}{L_x}\int_0^{L_x}\sigma_{\text{size}}\, dx = \frac{3\mu\varepsilon\omega L_x}{d}\left(\frac{2\sin(\omega t)+2\sin(k-\omega t)-k\cos(k-\omega t)-k\cos(\omega t)}{k^2}\right), \tag{2.62}$$

which has critical points at

$$t^* = \frac{1}{\omega}\arctan\left(\frac{2\cos(k)+k\sin(k)-2}{k\cos(k)+k-2\sin(k)}\right). \tag{2.63}$$

Again, we see that there are two branches of the arctan function which yield values of t^* in the range of one period $[0, 2\pi/\omega]$. And again, the choice of which branch to use will simply shift the argument of the sinusoids in Equation (2.62) by a value of π. This implies that branch choice simply changes the sign of $\overline{\sigma}_{\text{size}}$. As we are only concerned with the magnitude of spacial average stress, this is irrelevant for our purposes. Now, in contrast to the case of the unconstrained deformation, the argument of the arctan function may take on values anywhere in the interval $(-\infty, \infty)$, and indeed has a pole at $k = \pi$. However, the left and right limits of the argument are $\pm\infty$, and thus t^* has left and right limits of $\pm\pi/(2\omega)$. Again, we see that this does not affect magnitude of $\overline{\sigma}_{\text{size}}$, which is our quantity of interest. Now we calculate the maximum average stress due to the fluid flow:

$$\begin{aligned}&\overline{\sigma}_{\max} := |\overline{\sigma}_{\text{size}}(t^*)| = \\ &\frac{3\mu\varepsilon\omega L_x}{dk^2}\left|2\sin\left(\arctan\left(\frac{2\cos(k)+k\sin(k)-2}{k\cos(k)+k-2\sin(k)}\right)\right)+2\sin\left(k-\arctan\left(\frac{2\cos(k)+k\sin(k)-2}{k\cos(k)+k-2\sin(k)}\right)\right)\right. \\ &\left.-k\cos\left(\arctan\left(\frac{2\cos(k)+k\sin(k)-2}{k\cos(k)+k-2\sin(k)}\right)\right)-k\cos\left(k-\arctan\left(\frac{2\cos(k)+k\sin(k)-2}{k\cos(k)+k-2\sin(k)}\right)\right)\right|.\end{aligned} \tag{2.64}$$

Again we see that both the maximum and total average stresses are of the form

$$\overline{\sigma}_{\max} = \frac{3\mu\omega L_x}{d}\varepsilon f(k), \tag{2.65}$$

and

$$\langle\overline{\sigma}\rangle = \frac{3\mu\omega L_x}{d}\varepsilon^2 g(k). \tag{2.66}$$

This again allows us to define the function

$$r(k) = \frac{g(k)}{f(k)}. \tag{2.67}$$

The functions f, g, and r are illustrated in Figure 2.2b and discussed in the following section.

2.5.3 Discussion of Stresses

We reiterate that Figure 2.2 shows calculated stresses for values of k that correspond to waves with infinite wavelength (spatially homogeneous) to those with a wavelength equal to the cell body length. This range is chosen because *physarum* plasmodia are seen to contract with a wave length several times the length of the plasmodium [MAT08]. Immediately, several characteristics are apparent in Figure 2.2. In the case of the unconstrained deformation, the maximum average stress (or rather, $f(k)$) is maximized at wave number $k = 0$. This means that the cell is generating maximal viscous stresses when the wavelength of the deformation wave is infinite. However, in this regime, the total average viscous stresses (defined by $g(k)$) are in fact zero over one period of the wave. Therefore, we see that while the cell is generating relatively large stresses, the symmetry of the problem results in no net stress that may be used for locomotion. Instead, the

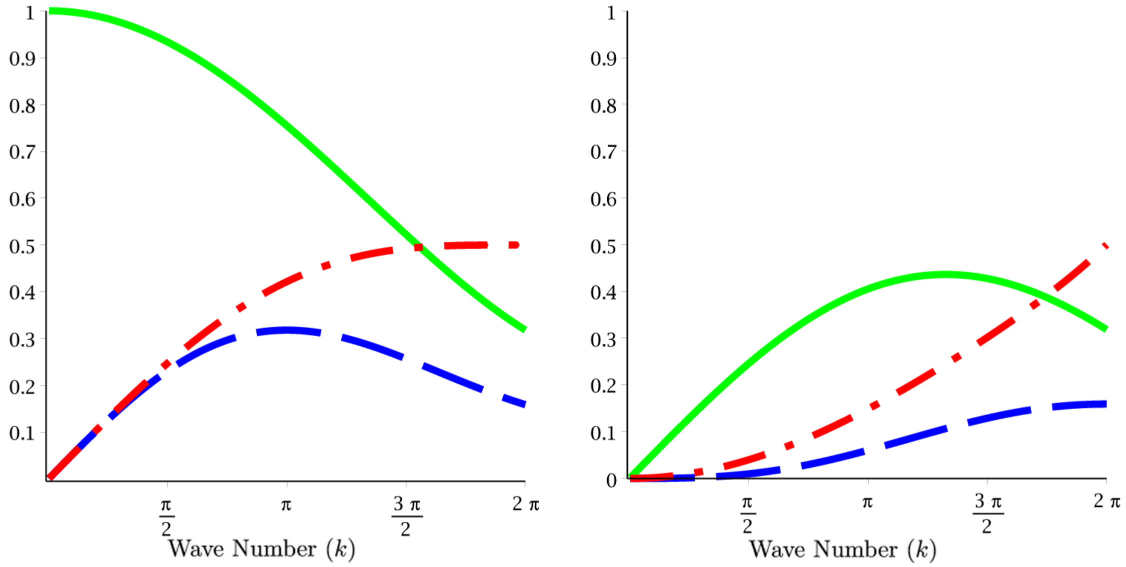

(a) Stress generation with open head.

(b) Stress generation with closed head.

Figure 2.2: Green solid lines indicate the function $f(k)$ which characterizes maximum avearge stress $\overline{\sigma}_{\text{max}}$. Blue dashed lines indicate the function $g(k)$ which characterizes total average stress $\langle\overline{\sigma}\rangle$. Red dash-dot lines indicates the ratio $r(k) = g(k)/f(k)$.

maximum imbalance in stresses occurs at $k = \pi$, which corresponds to a deformation wavelength which is twice the cell body length. At this wavelength, the function g takes on a maximal value of $1/\pi$. Finally, we note that the ratio of these is maximized at $k = 2\pi$, which corresponds to a deformation wavelgnth equal to the cell body length. At this wavelength, the function r takes on a value of $1/2$, while $f(2\pi) = 1/\pi$ and $g(2\pi) = 1/2\pi$. This may be interpretted to mean that while the deformation is generating stresses of magnitude $1/\pi$, a proportion $\varepsilon/2$ of them are directionally unbalanced and thus may be used to drive the cell across its substrate. In Section 2.6 we will redimensionalize these stresses to their physical scales.

The case of constrained deformation is rather different. The maximum average stress f has a non-trivial extrema in the interval $k \in [0, 2\pi]$, but now the total average stress (g) is maximized at $k = 2\pi$. It is still the case that in the limit $k \to 0$ (infinite wavelength, or spatially homogeneous deformation), the total average and effective stresses are negligible. However, we are not concerned with this limit, as our approximations are dubious in this case. Curiously enough, in the case $k = 2\pi$, all three measures of stress (f, g, and r) are identical to those calculated with unconstrained deformation. This is a consequence of the functional form of the constrained deformation given in Equation (2.31). When $k = 2\pi$, this reduces to the unconstrained deformation given by Equation (2.21). finally, we note that for all values of k, all three stresses (f, g, and r) are less than or equal to the same measurements in the case of the unconstrained deformation. This implies that when deformation is constrained by volume preservation, not only does the cell produce less stress, but a smaller ratio of the stress produced is directionally unbalanced for use in motility. This implies that a front-back asymmetry in the domain aids in the generation of motile stresses. We will return to this idea in the following section.

2.6 Redimensionalization

We now return to the problem of redimensionalizing the model predictions and examining the predicted stress generation in physical units. From Equations (2.50) & (2.64), we can see that only five parameters are required to calculate the stresses associated with the flow of cytoplasm. From [Mat08] and our collaboration with Dr. Nakagaki, we have good estimates for the thickness of the cell in the z-direction (d), the frequency of the wave pattern (ω), and the non-dimensional deformation amplitude ($\epsilon = A/h_0$). We also can estimate the wave number (k) from the data presented in [Mat08]. The one parameter that we do not have accurate estimates for is the viscosity of the cytoplasm within the cell chamber (μ). Estimation of the rheological properties of cell interiors is a difficult problem and may result in values ranging over several orders of magnitude depending on cell type and experimental set-up [Lim06]. To our knowledge, no attempt to experimentally measure or estimate of the internal rheology of *physarum* plasmodium exists in the literature.

However, our model does provide us a way to crudely estimate the cytoplasmic viscosity. Equation (2.14) allows us to perform this estimation, provided that we know the characteristic flow velocity and pressure gradient. While we do not know the local pressure gradient within the cell, we do know the characteristic length of the cell body (L_x). We also have estimates for the characteristic pressure difference ($[p]$) from the anterior to posterior of the cell [Kam57]. Finally, it is relatively easy to extract a characteristic velocity scale from the data in [Mat08]. The known parameters are listed in Table 2.1.

Using the values listed in Table 2.1 and Equation (2.14), we approximate the viscosity of the intracellular fluid as

$$\mu \approx \frac{[p]d^2}{12 L_x U}. \tag{2.68}$$

This yields a viscosity of $\mu = 50/3$ Pa sec ≈ 17 Pa sec. For comparison, this is roughly the viscosity of honey [VP], or approximately $17,000$ times the viscosity of water. As previously stated, measuring the viscosity of cytoplasm is a difficult problem, partially due to the ambiguity of the material being measured.

Table 2.1: Known parameters for peristaltic pumping in *Physarum*.

Parameter	Numerical Value	Description
L_x	400 µm	Cell length
$[p]$	1000 Pa	Pressure difference across cell
$2\pi/\omega$	100 sec	Wave period
$2\pi/k$	1600 µm	Wavelength
d	20 µm	Cell thickness
h_0	20 µm	Cell resting half-width
A	5 µm	Deformation amplitude
U	5 µm/sec	Characteristic fluid veloicty

Cytoplasm is a complex mixture of ions, proteins, and other compounds. Proteins such as actin may polymerize (to form a gel-like network) or depolymerize spontaneously or in response to various chemical signals. This means that the measured rheology of cytoplasm can vary wildly depending on timescale of interest, experimental methodology, environmental factors, or cell type [LP94]. Values for cytoplasmic viscosity have been reported over several orders of magnitude [Lim06], ranging up to 10^4 Pa sec for fibroblasts [Tho99]. Furthermore, our model has homogenized all of this complex rheology into a single parameter. Therefore, while the computed value of μ is rather high to describe *cytosol*, it is well within a reasonable range to describe the viscosity of cytoplasm.

Given our approximate value of μ, we may return to the calculated stress functions and express them in dimensional values. As previously noted, the ratio of deformation amplitude to cell half-width is $\varepsilon = A/h_0 = 0.25$. The dimensional constant found in $\langle\overline{\sigma}\rangle$ and $\overline{\sigma}_{\max}$ is

$$\frac{3\mu\omega L_x}{d} = 10 \text{ Pa}. \tag{2.69}$$

The deformation wavelength seen in [Mat08] corresponds to a wave number of $k \approx \pi/2$. This is a wavelength four times the length of the cell body. Using this value, we may finally evaluate the total average and maximum average stresses. The results are summarized in Table 2.2. We note that the figures listed in Table 2.2 are relatively low compared to experimental measurements in some cell types. Strongly adherent cells such as keratocytes have been observed exerting stresses up to $10,000$ Pa on the substrate [Bur99]. However, some weakly adherent cells such as *dictyostelium* are known to migrate using traction stresses on the order of 20 to 40 Pa or less [Bas14]. Thus, the values of $\overline{\sigma}_{\max}$ calculated in Table 2.2 may be small, however, we note that this analysis addresses only *viscous* stresses associated with the flow of cytoplasm. We have not addressed any elastic or contractile stresses which may also effect traction stress measurements.

Table 2.2: Basal viscous stresses associated with flow. All values calculated with $k = \pi/2$.

		Unconstrained deformation	Constrained deformation
$\overline{\sigma}_{\max}$	Maximum Average Stress	2.333 Pa	0.6150 Pa
$\langle\overline{\sigma}\rangle$	Total Average Stress	0.1446 Pa	0.006159 Pa

Finally, we note again that the maximum average stress $\overline{\sigma}_{\max}$, as well as the total average stress $\langle\overline{\sigma}\rangle$, are larger in the case of unconstrained deformation, compared to constrained deformation. Since the constraint which we placed on the deformation was meant to prevent fluid flow through the anterior head of the cell, this case corresponds to a spatially symmetric domain. The model suggests that a spatial heterogeneity aids in the production of viscous stress via peristaltic pumping. It has been observed that the cell head is mechanically distinct from the rest of the body of the plasmodium [Sto94]. The head of the cell appears to be more elatically compliant, as the tail has a more developed and organized actin cytoskeleton and cortex. Within the context of our model, the unconstrained deformation represents the situation where the elastic stiffness of the head region is zero. In this case, fluid may flow into the head without penalty. Conversely, in the limit of infinite stiffness, fluid may not flow into the head, regardless of the applied pressure. This scenario is mimicked by our constrained deformation. It is unlikely that either scenario perfectly captures the mechanics of the cell head *in vivo*, and a more sophisticated model would represent an elastic regime between these two limits. However, our model does indicate that the mechanical heterogeneity at the cell head may be an important factor in generating motility. In the case of the constrained deformation, the model shows that there is a non-zero net viscous stress associated with the flow in a closed peristaltic pump. The directionality of the peristaltic wave is enough of an asymmetry to generate this non-zero stress. However, this stress is exceptionally low. An *additional* asymmetry such as the mechanical response in the head, may increase the unbalanced stresses associated with the peristaltic flow. This suggests that a more sophisticated model including the mechanically distinct cell head is of value. We will develop and analyze just such a model in Chapters 3 & 4.

2.7 Phase Differences

Having now quantified the stresses associated with two distinct forms of peristaltic pumping within the cell body, we now quantify the relative timing of the flow and deformation waves. In [Mat08], the authors noted a particular relationship between flow and deformation. Picking a location on the cell axis and regarding both waves as a function of time only, they noted that deformation preceded flow by approximately one quarter of the wave period. That is, the maximum forward flow velocity of the wave occurred approximately 25 sec after the same location on the cell axis had reached its maximum width. This behavior is illustrated in Figure 2.3. It was hypothesized that this phase relationship aided in driving motility. This hypothesis was based on the argument that with this particular timing, the width of the cell would be (on average) wider at locations in space and time where the flow was directed forward. Similarly, the cell would be narrower at locations where the flow was directed backwards. The result of this asymmetry, it was argued, is a net forward flux of mass, as more cytoplasm flows forward through a larger channel. However, this behavior is not generic at all points along the cell axis. Figure 2.4 shows that for much of the length of the cell body, the maximum cell width (open circles) occurs a quarter period before the maximum flow velocity (center of the white region of forward flow). However, in regions closer to the head (indicated with dashed white lines), this relationship is broken and appears to even reverse. Near the cell head, the maximum cell width occurs just *after* the maximum flow velocity. We explore this phase relationship with our model and determine, if possible, the origin of the observed data.

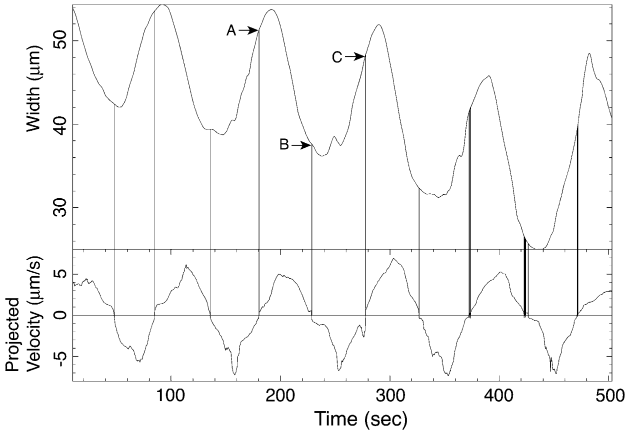

Figure 2.3: Time sequence of cell width and intracellular fluid velocity along the cell axis. Measurements were taken at a location on the cell axis indicated by a dashed grey line in Figure 2.4. Reprinted from [Mat08] with permission from Elsevier.

2.7.1 Unconstrained Deformation

For simplicity, we will work in non-dimensional body coordinates. This is accomplished via the transformation $x \mapsto x/L_x$. This simplifies calculations greatly and does not affect predicted values, as we will only be concerned with non-dimensional quantities such as phase. We begin by noting that the imposed

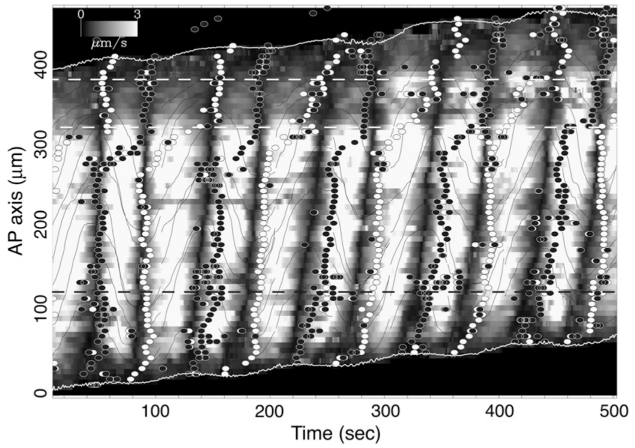

Figure 2.4: Relationship of flow and deformation in migrating *physarum*. Greyscale indicates the magnitude of intracellular flow along the cell axis. Open circles indicate the onset of contraction (cell width is maximal). Filled circles indicate the onset of expansion (where cell width is minimal). Filled grey lines indicate particle paths obtained via integration of the velocity field. The dark grey dashed line indicates the location where the data from Figure 2.3 was obtained. White dashed lines indicate the region in the cell head that appears mechanically distinct from the cell body. Reprinted from [Mat08] with permission from Elsevier.

deformation, Equation (2.21), may be regarded as the real part of a complex exponential oscillation. This oscillation has the form

$$h(x,t) = h_0 + Ae^{i(kx-\omega t)}. \tag{2.70}$$

The *displacement*, given by Equation (2.27), which we earlier referred to as the input of the model, is the real part of the function

$$\overline{h}(x,t) = Ae^{i(kx-\omega t)}. \tag{2.71}$$

The output oscillation, which results from driving the model with this input, is the flux of fluid (Equation (2.26)), which has complex form

$$Q(x,t) = \frac{2A\omega}{k}\left(e^{i(kx-\omega t)} - e^{-i\omega t}\right). \tag{2.72}$$

Both the input and output may be regarded as a complex function multiplied by the temporal oscillation $e^{-i\omega t}$. That is,

$$\overline{h}(x,t) = D(x)e^{-i\omega t}\text{ , and } Q(x,t) = F(x)e^{-i\omega t}. \tag{2.73}$$

The functions $D(x)$ and $F(x)$ may be regarded as spatially varying modulations of the waves $\overline{h}$ and Q respectively. It is a simple matter to determine that

$$D(x) = Ae^{ikx}, \tag{2.74}$$

and that

$$F(x) = 2A\omega \frac{e^{ikx} - 1}{k}. \tag{2.75}$$

Now, we define the spatially varying *phase* of the displacement and flux to be the complex argument of the functions D and F respectively

$$\varphi_{\text{in}} = \arg\Big(D(x)\Big), \text{ and } \varphi_{\text{out}} = \arg\Big(F(x)\Big). \tag{2.76}$$

It is not so simple to derive analytical expressions for φ_{in} and φ_{out}. However, these functions are straightforward to evaluate numerically. Figure 2.5 show calculated values of φ_{in} and φ_{out} as a function of the normalized cell coordinate x. To analyze the relative timing of the displacement and deformation waves, we also calculate the quantity

$$\varphi = \varphi_{\text{out}} - \varphi_{\text{in}}. \tag{2.77}$$

This is a measure of the relative phase of the two oscillations and is defined so that a positive value of φ corresponds to the displacement *preceeding* the flow wave, while a negative value corresponds to the displacement wave *following* the flow wave. Calculated values of φ are shown in Figure 2.5c.

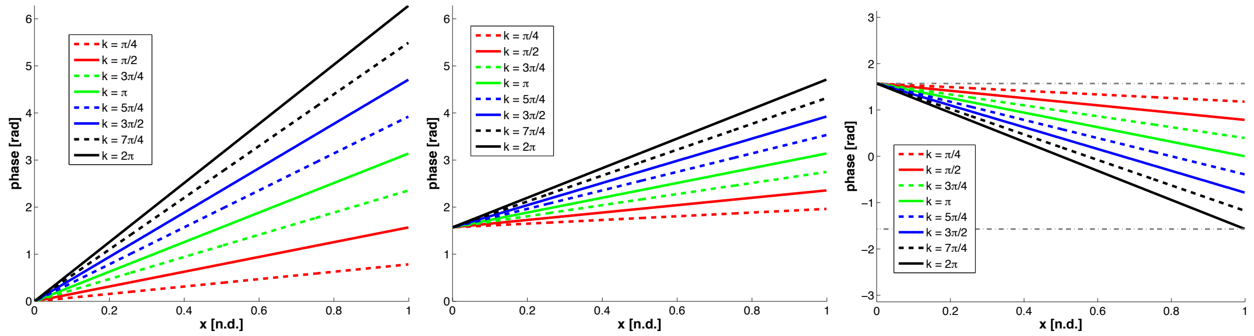

(a) φ_{in} (b) φ_{out} (c) φ

Figure 2.5: Calculated phases for unconstrained deformation. Panel (a) shows the phase of the displacement function $D(x)$ as a function of x and wave number k. Panel (b) shows the phase of the associated flux fucntion $F(x)$. Panel (c) shows the relative phase $\varphi = \varphi_{\text{out}} - \varphi_{\text{in}}$. Dashed grey lines indicate relative phases of $\pm\pi/2$, or one quarter period.

We note that a phase which is perfectly linear in the body coordinate x corresponds to a waveform that propagates along the cell axis in a linear fashion (such as $\cos(kx - \omega t)$). The displacement wave propagates through the cell linearly by construction, and thus φ_{in} is linear in x. However, the phase of the flow wave also is linear. This results in a phase difference φ that is a linear function of the cell-axis coordinate. At the tail of the cell ($x = 0$), we see a phase difference of $\varphi = \pi/2$ regardless of the wave number of the input deformation. This agrees with the observed phase relationship reported in [Mat08] (the wave length of deformation observed in that work corresponds to a value $k \approx \pi/2$). Depending on the wave number k, the phase relationship decreases as a function of body coordinate. In the most extreme case ($k = 2\pi$), we see a phase difference of $\varphi = -\pi/2$ at the head of the cell. This means that the flow wave is preceding the deformation wave by a quarter period. For other wave numbers this decrease in relative phase is less dramatic.

2.7.2 Constrained Deformation

We now perform the same calculation for the volume preserving deformation that was derived in Section 2.4.2. The functional form of the constrained deformation, Equation (2.31) may be regarded as the real part of the complex function

$$h(x,t) = h_0 + A\left(e^{i(kx-\omega t)} + \frac{i}{k}\left(e^{i(k-\omega t)} - e^{-i\omega t}\right)\right). \tag{2.78}$$

This allows us to define the complex displacement function

$$\overline{h}(x,t) = A\left(e^{i(kx-\omega t)} + \frac{i}{k}\left(e^{i(k-\omega t)} - e^{-i\omega t}\right)\right). \tag{2.79}$$

Similarly, the associated flux of fluid given by Equation (2.36) is the real part of

$$Q(x,t) = \frac{2A\omega}{k}\left(e^{i(kx-\omega t)} - xe^{i(k-\omega t)} + xe^{-i\omega t} - e^{-i\omega t}\right). \tag{2.80}$$

Factoring out the complex temporal oscillation allows us to define the input function

$$D(x) = A\left(e^{ikx} + \frac{i}{k}\left(e^{ik} - 1\right)\right), \tag{2.81}$$

and the output function

$$F(x) = 2A\omega\frac{e^{ikx} - xe^{ik} + x - 1}{k}. \tag{2.82}$$

We again define φ_{in}, φ_{out}, and φ in the same manner as the previous section. Figures 2.6a & 2.6b show the calculated phases of the displacement and flow waves in the case of constrained deformation. Figure 2.6c shows the relative phase of the two waves (φ). Again, a positive value of φ corresponds to the displacement wave preceding the flow wave.

The phase relationships illustrated in Figure 2.6 are rather different than those observed in the case of the unconstrained deformation. The flow wave still appears to be a phase wave, as φ_{out} is a linear function of body coordinate. However, the displacement wave phase (φ_{in}) has a much more complex character. For

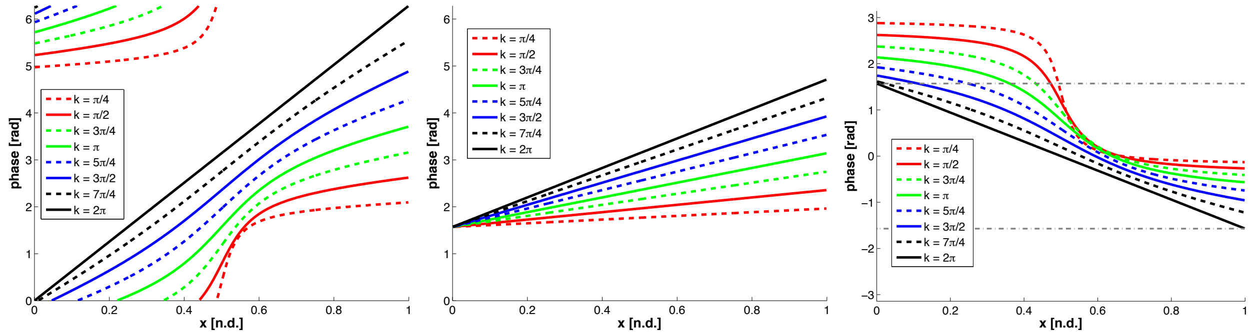

(a) φ_{in} (b) φ_{out} (c) φ

Figure 2.6: Calculated phases for constrained deformation. Panel (a) shows the phase of the displacment function $D(x)$ as a function of x and wave number k. Panel (b) shows the phase of the associated flux fucntion $F(x)$. Panel (c) shows the relative phase $\varphi = \varphi_{\text{out}} - \varphi_{\text{in}}$. Dashed grey lines indicate relative phases of $\pm\pi/2$, or one quarter period.

small values of k (longer wavelength deformations), we see that φ_{in} has a somewhat sigmoidal dependence on body coordinate. The result of this is that the phase difference φ has a sharp transition near the center of the cell body. In the most extreme case shown ($k = \pi/4$), we see a phase difference of approximately $\varphi = \pi$ in the back half of the cell and a phase difference of approximately $\varphi = 0$ in the front half of the cell. This corresponds to a scenario where the flow and deformation waves are perfectly anti-phase in the posterior of the cell and perfectly in-phase in the anterior. As we have previously stated, in the case that $k = 2\pi$ the model reproduces the results of the unconstrained deformation. Other values of k interpolate between these two behaviors.

2.7.3 Relation to Experiment

We now restrict ourselves to the wave number that most closely approximates the observed deformations in migration *physarum* ($k = \pi/2$) and compare the predicted phase differences to experimental observations. This wave number is represented by the solid red lines in Figures 2.5 & 2.6. For clarity, we reproduce the phase difference φ of this wave number for both deformations in Figure 2.7. The solid blue line represents φ for an unconstrained deformation, while the dashed red line represents the same measurement for the constrained deformation. We see that in both cases, the model captures certain aspects of the experimental observations but poorly reproduces other features of the data seen in Figure 2.4.

As we have previously discussed, for the constrained volume preserving deformation, the model predicts a nearly anti-phase relationship in the posterior of the cell ($\varphi \approx 2.6226 \approx 8\pi/10$ at $x = 0$) and a nearly in-phase relationship in the anterior ($\varphi \approx -0.2664 \approx -8\pi/100$ at $x = 1$). Clearly this does

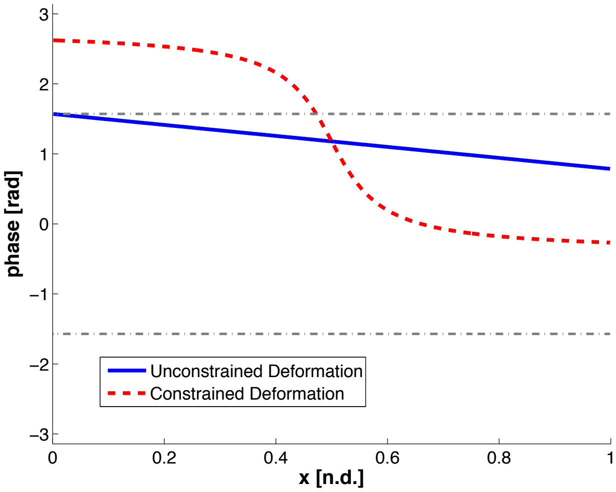

Figure 2.7: Relative phase φ calculated with the model for wave number experimentally observed in [MAT08]. Solid blue line indicates φ for the unconstrained deformation (open head). Dashed red line indicates phase for the constrained deformation (closed head).

not match the experimental data. As previously noted, the experimental data indicates a relative phase of approximately $\pi/2 \approx 1.5708$ throughout *most* of the cell body. Near the anterior end of the cell, there is a transition where the relative phase decreases to approximately $-\pi/2$ over a relatively short spatial domain (see Figure 2.4). The model *does* predict this rapid transition of relative phase. Moreover, the model predicts that the deformation wave "catches up" to the flow wave by a factor of nearly π, just as observed in experiments. However, this transition occurs in a spatial location (the center of the cell) that is not consistent with experimental observations.

Conversely, in the case of unconstrained deformation, our model predicts phase relationships that are relatively constant throughout the spatial domain. For the free deformation, the model gives a relative phase of $\varphi = \pi/2 \approx 1.5708$ at the posterior of the cell ($x = 0$). This decreases linearly to a value of $\varphi = \pi/4 \approx 0.7864$ at the anterior of the cell ($x = 1$). In this case, the model predicts a phase difference that is *close* to the observed value $\pi/2$ throughout most of the domain. The unconstrained deformation, however, fails to reproduce the rapid transition in relative phase that is seen in both experiments and the model with constrained deformation. Thus we see that without constraint, the model predicts the correct (approximate) value of φ throughout the majority of the cell body but fails to capture the qualitative transition near the head. With the deformation constraint, the model predicts a qualitatively correct transition but is inconsistent with the observed location of this transition, as well as the values of φ.

We again come back to the notion that our model, in both cases, involves a highly idealized representation of the cell head. Fluid may flow freely into the head with no penalty, or may not flow into the head at all. In all likelihood, the elastic behavior of the anterior end of *physarum* allows cytoplasm to flow forward and extend the anterior membrane with some associated pressure penalty. Our two model cases are extreme limits of this behavior. It seems plausible that the elastic compliance of the cell head *in vivo* interpolates between these two limits, and gives rise to the precise phase differences observed in experiments.

2.8 Discussion

Physarum plasmodia have been observed to migrate across a substrate while undergoing peristaltic contractions of the cell membrane. These contractions drive a periodic streaming flow of cytoplasm on the cell interior. This flow has been postulated to be responsible for driving the observed motility. In this section, we have developed a model that treats the migrating *physarum* plasmodium as a peristaltic chamber. The behavior of this model was analyzed in two cases: (1) the head of the cell is infinitely compliant, and cytoplasm may flow freely through the anterior end of the peristaltic chamber; (2) the head of the cell is infinitely stiff, and cytoplasm may not flow through the anterior end of the peristaltic chamber.

From the model, we were able to calculate the relative phases of the waves of deformation on the cell exterior and flow on the cell interior. We saw that the model was unable to perfectly reproduce the experimentally observed phase relationship. However, in each case, the model was able to reproduce certain aspects of the observed phase relationships. This suggests that the elastic behavior of the head is not accurately reproduced by either of the idealized cell head behaviors captured with our model. However, it seems plausible that a finite compliance (and some elastic response law) would interpolate between the two limiting cases presented here and accurately reproduce the observed phase differences. Moreover, this may suggest that the observed phase differences are not designed to enable motility, but rather a necessary product of pumping fluid withing a peristaltic chamber (with an elastic end). Regardless, to faithfully reproduce the deformation-flow relationship observed in [Mat08], we require a more sophisticated model that takes into account the elasticity of the domain in which fluid is being pumped. The development of such a model is the main goal of the following chapter.

Using our peristaltic model we also quantified the characteristic viscous stresses generated by the flow of fluid within the cell chamber. We showed that at any particular point in time, there is a non-zero spatial average stress associated with the flow. Furthermore, depending on the form of the deformation wave, this stress may be up to ~ 2.33 Pa in size. Over a full period of the wave, these average stresses nearly balance but not completely. The space and time average stress associated with the flows may be up to ~ 0.14 Pa. Thus, at any point in time, the average stresses associated with the flow may be of biologically relevant scale, but over one full period of the wave the net stress is of a less significant scale.

We saw that the stress associated with flow was in general increased in the case of the unconstrained deformation, when fluid was allowed to flow freely into the head. In the case of a closed head, the domain is spatially symmetric, non-zero stresses are generated, but they are quite small (sub Pa scales). This is a product of the directionality of the deformation and flow waves. However, an additional asymmetry in the problem, namely the infinitely compliant head, increased our measures of stress by an order of magnitude (or more). This again suggests that a more sophisticated model of *physarum* motility should incorporate a treatment of the mechanical asymmetry of the plasmodium head.

Finally, we note that even in the case of the unconstrained deformation, where cytoplasm may flow freely into the head, the spatial average stress is small when compared to some migrating cells [Tho99]. In Chapter 4 we will see that migrating *physarum* exert stresses on its substrate that are on the order of hundreds of Pascals. However, we note that our analysis of the peristaltic model only quantifies the *average* stresses generated by the flow. We have ignored any local treatment of stress. Obviously the stress σ will locally be larger (or smaller) than the values reported in Table 2.2. It is plausible that *physarum* may mechanically transmit these local viscous stresses to the substrate in a coordinated manner, and therefore produce traction stresses on a scale larger than indicated in Table 2.2. Furthermore, we have only treated *viscous* stresses in this analysis, ignoring both contractile and passive elastic stresses within the cytoskeletal structure of the cell. Such stresses are likely to contribute to the traction stresses measured in Chapter 4. To address such issues, we require a more sophisticated model that incorporates contraction of the cells mechanical structure and the linkage of the intracellular space to the extracellular substrate. We now develop such a model in Chapter 3.

CHAPTER 3

Model Development

3.1 Introduction

In the previous chapter, our model described the intracellular material of *physarum* as a Newtonian fluid (albeit with high viscosity). This is admittedly a simplification of the rheological properties of intracellular cytoplasm. *Physarum* cytoplasm contains an wide multitude of proteins, ions, organelles, and other material that alter the mechanical properties of the intracellular space [LP00]. Critically, the cytoplasm is filled with an actin-myosin cytoskeleton that is important in a wide variety of cell functions. In addition to providing structural integrity to the cell, the actin cytoskeleton is known to be associated with transmembrane adhesion structures that mechanically link the cell interior to the extracellular matrix and/or substrate [Bri87]. Thus, the cytoskeletal structure of the cell interior is involved in transmitting stresses internally generated to external structures. As mentioned in the previous chapter, our peristaltic model of the cytoplasmic flow within *physarum* included only hydrodynamics of intracellular fluid. We did not address the matter of how such stresses may be transmitted to the substrate. In this chapter we develop a more detailed model that addresses this shortcoming.

The model that we develop incorporates the physics of four basic systems within *physarum* plasmodia: the intracellular fluid; the porous, elastic cytoskeleton; the membrane/cortex which encapsulates the plasmodium; and adhesions coupling the cell to the substrate. Our description of the intracellular fluid remains very similar to in Chapter 2. We still assume that the fluid which fills the interior of *physarum* is Newtonian. Because the system we are modelling is in a non-inertial regime, the fluid equations of interest remain the incompressible Stokes equations. As we have already discussed, there are a number of structures within the cell interior that give rise to more complex rheology, however we effectively lump all of them into our description of the cytoskeletal structure on the interior of the cell.

Our model of the intracellular structure takes the form of a porous, elastic material that is permeated by the intracellular fluid (or cytosol). We envision this elastic material as an approximation of the actin cytoskeleton of the physarum. However, in the context of our model it incorporates any other structures which may give the cell interior an elastic stress response. When combined with the Newtonian description of the interstitial cytosol, this effectively describes the interior of physarum as a poro-elastic material. Recent experimental work on blebbing cells has suggested that a poro-elastic description of the cytoplasm is required to properly capture the effects of pressure propogation through the cytoplasm [Cha05, Mit08, Cha09]. Because *physarum* appears to drive flow within the cell interior via contraction generated pressure gradients, it is important that our model properly capture these dynamics. For this reason, we develop a poro-elastic description of the cell interior. Furthermore, the elastic cytoskeleton (which we will often refer to as the "network") provides the mechanical structure that links the intracellular flow to adhesions that interact with the substrate.

Many cell species transmit stresses to the underlying substrate via highly localized aggregates of integrins and accessory proteins known as focal adhesions [Bur88]. By contrast, *physarum* does not appear to transmit stresses in such a highly localized manner. Instead, traction stresses on the substrate are diffuse, and applied across the ventral surface of the cell (see Chapter 4 for the traction stress patterns exerted by migrating *physarum*). The details of the mechanical structure that *physarum* uses to apply these stresses are not known. It is not even known if *physarum* expresses integrin-like transmembrane proteins, though some candidate proteins have been identified [Hay08]. However, the period of the deformations and flow patterns observed in *physarum* is long ($\sim$ 100 sec) compared to the timescale of the life of an integrin bond [Kon09]. Over longer time scales and large ensembles of bonds, one can represent the dynamics of adhesion via a viscous drag law [Sri09]. Because of this, our model assumes the adhesive complexes of *physarum* interact with the cytoskeletal network elastically and with the substrate viscously. Furthermore, given the lack of data on the precise nature of adhesion mechanics in *physarum*, we are unable to develop a mechanistic model of how the strength of adhesion to the substrate may be regulated. Our model allows for the modulation (in space and time) of the strength of viscous interaction with the substrate. However, the form of this modulation will be somewhat phenomenological and will, in fact, be an input of the model in Chapter 4.

Finally, our model reflects the fact that a *physarum* plasmodium is enclosed in a cell membrane. This membrane is a bilipid layer, together with various embedded proteins, and delineates the cell interior from the extracellular space. Immediately adjacent to the interior surface of the cellular membrane is the cortex [Kuk87]. The cortex is a specialized layer of cytoskeleton comprised mostly of dense cortical actin, as well as various accessory proteins. This layer functions to provide structural support to the cellular membrane and is responsible for much of the elastic properties of the membrane in our model. We represent the membrane and cortex *together* as a single one dimensional structure, which we will refer to as the "membrane" for brevity. The underlying cortex of *physarum* is mechanically coupled to the bulk cytoskeleton by an array of linking proteins [Hor86, Ise92]. As a first approximation, we model this coupling with a Hookean force law linking a material point on the membrane with the corresponding point on the boundary of the cytoskeleton.

In this chapter, we develop a model of a crawling *physarum* plasmodium that incorporates all of the aforementioned physics. Concurrently, we develop a computational framework with which to simulate a crawling cell. This computational framework will be based on the Immersed Boundary method. Since the Immersed Boundary method is a rather general framework, and not specific to the problem at hand, we describe its machinery first. In later sections we describe the mathematical model of the poro-elastic cytoskeleton, the viscous adhesion to the substrate, and the elastic membrane surrounding the cell. As we do so, we outline how each may be simulated via our Immersed Boundary framework.

3.2 Immersed Boundary Framework

We now develop a computation framework with which to simulate a crawling cell with a poro-elastic interior. To do this, we first note that the equations of fluid mechanics are most naturally formulated in a fixed Eulerian coordinate system. Conversely, elastic constitutive laws are more naturally treated in moving Lagrangian coordinates. Our method leverages each of these "natural" representations and uses both coordinate systems where appropriate. The Immersed Boundary (IB) method is a computational method that was developed to exploit the convenience of both coordinate systems in simulating fluid-structure interaction problems [Pes77]. For this reason, we develop a model based on the IB method.

The IB method was originally developed to simulate blood flow [Pes77] but has since been adopted to address an array of fluid-structure interaction problems in biology and engineering [Mit05]. The key feature of the IB method is that the equations of fluid mechanics are solved in a fixed Eulerian coordinate system, while the equations of the immersed solid structure are represented on a moving Lagrangian coordinate system [Pes02]. Transformations between the two coordinate systems are accomplished by the so-called “spread” and “interpolation” operators, which are both convolutions against a delta distribution kernel. Novel use of the spread and interpolation operators allows numerical simulation of fluid equations in complex geometries (often defined by the immersed structures) without the use of geometry conforming meshes. In the traditional IB formulation, the immersed structure is assumed to be neutrally buoyant so that all stresses on the boundary are transmitted to the fluid. It is also assumed that a no-slip boundary condition is satisfied at the fluid-structure interface. One of these assumptions is inappropriate for the simulation of a poro-elastic material, as the immersed solid does not move with the local fluid velocity. Rather, relative motion of the porous solid and the fluid results in a drag force density. However, the basic machinery of the IB method is not restricted to the above assumptions, and we will see that it may be leveraged to simulate the coupled poro-elastic equations in a single unified framework.

We now introduce some notation. For the remainder of this work, $\boldsymbol{x}$ will represent the Eulerian coordinate (with domain Ω). We use $\boldsymbol{s}$ as the Lagrangian coordinate (with domain Γ_{net}) that parametrizes a volume-filling material that we call the “network”. This will model the cytoskeleton on the cell interior. The variable θ will be a second Lagrangian coordinate (with domain Γ_{mem}) that parametrizes a co-dimension one material which models the cell membrane and cortex. In Section 3.3.1, we will describe how we reduce our cell model to two dimensions. Therefore, θ will parametrize a one-dimensional membrane, while $\boldsymbol{s}$ will parametrize a two-dimensional cytoskeleton. Wherever possible, we will use the convention that quantities that are defined in the Eulerian frame will be denoted with lower case letters, while Lagrangian quantities will be denoted in upper case. For example, $\boldsymbol{X}_{\text{net}}(\boldsymbol{s}, t)$ will denote the physical position of the material point of network $\boldsymbol{s}$ at time t. See Figure 3.1 for an illustration. The key insight of the IB method is that we are free to compute in either coordinate system provided we have the appropriate coordinate transform. The operator which maps from the Lagrangian coordinate $\boldsymbol{s}$ to Eulerian coordinate $\boldsymbol{x}$ is known as the spreading operator, is denoted $\mathcal{S}_{\text{net}}$, and is given by

$$\boldsymbol{v}(\boldsymbol{x}) = \mathcal{S}_{\text{net}}\left[\boldsymbol{V}(\boldsymbol{s})\right] = \int\limits_{\Gamma_{\text{net}}} \boldsymbol{V}(\boldsymbol{s})\, \delta\left(\boldsymbol{X}_{\text{net}}(\boldsymbol{s}, t) - \boldsymbol{x}\right)\, d\boldsymbol{s}. \tag{3.1}$$

Similarly, the interpolation operator, denoted by $\mathcal{S}^*_{\text{net}}$, maps from Eulerian coordinates to Lagrangian,

$$\boldsymbol{V}(\boldsymbol{s}) = \mathcal{S}^*_{\text{net}}\left[\boldsymbol{v}(\boldsymbol{x})\right] = \int\limits_{\Omega} \boldsymbol{v}(\boldsymbol{x})\, \delta\left(\boldsymbol{X}_{\text{net}}(\boldsymbol{s}, t) - \boldsymbol{x}\right)\, d\boldsymbol{x}. \tag{3.2}$$

We use this notation for interpolation because the spread and interpolation operators satisfy an adjoint property. For two scalar fields V_1 and v_2 defined in Lagrangian and Eulerian coordinates respectively,

$$\begin{aligned}
\langle S_{\text{net}} V_1, v_2 \rangle_\Omega &= \int\limits_\Omega v_2(\boldsymbol{x}) \left(\int\limits_{\Gamma_{\text{net}}} V_1(\boldsymbol{s}) \delta \left(\boldsymbol{X}_{\text{net}} \left(\boldsymbol{s}, t \right) - \boldsymbol{x} \right) \, d\boldsymbol{s} \right) \, d\boldsymbol{x} \\
&= \int\limits_\Omega \int\limits_{\Gamma_{\text{net}}} V_1(\boldsymbol{s}) v_2(\boldsymbol{x}) \delta \left(\boldsymbol{X}_{\text{net}} \left(\boldsymbol{s}, t \right) - \boldsymbol{x} \right) \, d\boldsymbol{s} \, d\boldsymbol{x} \\
&= \int\limits_{\Gamma_{\text{net}}} V_2(\boldsymbol{s}) \left(\int\limits_\Omega v_2(\boldsymbol{x}) \delta \left(\boldsymbol{X}_{\text{net}} \left(\boldsymbol{s}, t \right) - \boldsymbol{x} \right) \, d\boldsymbol{x} \right) \, d\boldsymbol{s} \\
&= \langle V_1, \mathcal{S}^*_{\text{net}} v_2 \rangle_{\Gamma_{\text{net}}}. \qquad (3.3)
\end{aligned}$$

An analogous result holds for vector fields. This calculation shows that the spread and interpolation operators preserve integrals when mapping between coordinate systems.

The spread and interpolation operators for one-dimensional Lagrangian structures are defined similarly:

$$\boldsymbol{v}(\boldsymbol{x}) = \mathcal{S}_{\text{mem}} \left[\boldsymbol{V}(\boldsymbol{X}) \right] = \int\limits_{\Gamma_{\text{mem}}} \boldsymbol{V}(\theta) \, \delta \left(\boldsymbol{X}_{\text{mem}} \left(\theta, t \right) - \boldsymbol{x} \right) \, d\theta, \qquad (3.4)$$

$$\boldsymbol{V}(\theta) = \mathcal{S}^*_{\text{mem}} \left[\boldsymbol{v}(\boldsymbol{x}) \right] = \int\limits_\Omega \boldsymbol{v}(\boldsymbol{x}) \, \delta \left(\boldsymbol{X}_{\text{mem}} \left(\theta, t \right) - \boldsymbol{x} \right) \, d\boldsymbol{x}, \qquad (3.5)$$

where $\boldsymbol{X}_{\text{mem}}(\theta, t)$ is the location of material point θ. A simple calculation shows that $\mathcal{S}_{\text{mem}}$ and $\mathcal{S}^*_{\text{mem}}$ satisfy an adjoint property analogous to Equation (3.3). To perform numerical simulations, we necessarily must discretize these integral operators. However, when we do so, we will take care to ensure that this adjoint property is preserved discretely. This will ensure that we do not violate physical constraints, such as the balance of forces on the system.

Having defined the operators that map between coordinate systems, we now formulate our IB-like method. Given a configuration of the immersed material $\boldsymbol{X}_{\text{net}}(\boldsymbol{s}, t)$, we may calculate the force density this structure exerts on the fluid:

$$\boldsymbol{F}_{\text{net}} \left(\boldsymbol{X}_{\text{net}} \left(\boldsymbol{s}, t \right) \right). \qquad (3.6)$$

We perform a similar calculation for the immersed membrane

$$\boldsymbol{F}_{\text{mem}} \left(\boldsymbol{X}_{\text{mem}} \left(\theta, t \right) \right). \qquad (3.7)$$

For now, we will not discuss the constitutive laws that give rise to these forces. Once the forces each structure exerts on the fluid are known (as a function of Lagrangian coordinate), we spread these forces to the Eulerian coordinate system:

$$\boldsymbol{f}_{\text{net}}(\boldsymbol{x}) = \mathcal{S}_{\text{net}}\left[\boldsymbol{F}_{\text{net}}\right], \tag{3.8}$$

$$\boldsymbol{f}_{\text{mem}}(\boldsymbol{x}) = \mathcal{S}_{\text{mem}}\left[\boldsymbol{F}_{\text{mem}}\right]. \tag{3.9}$$

Note that due to the form of Equation (3.4) and the fact that θ parametrizes a one-dimensional membrane, $\boldsymbol{f}_{\text{mem}}$ is a delta-like distribution of force density, supported on the location of the membrane.

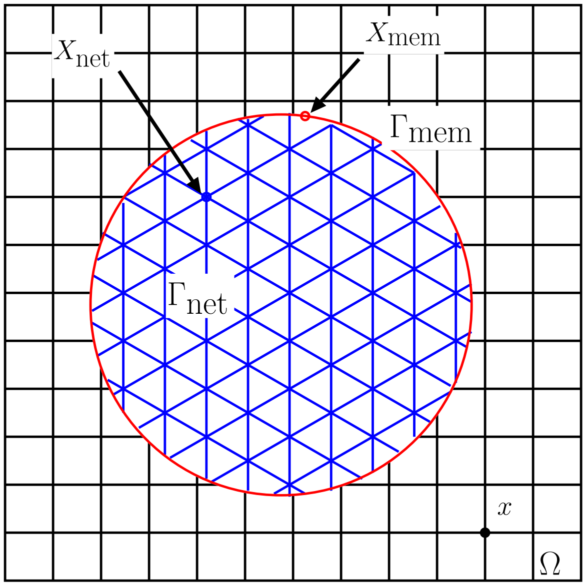

Figure 3.1: A generic scenario for poro-elastic simulations. The Eulerian variable is indicated by $\boldsymbol{x}$ with domain Ω. The position of the elastic network is given by $\boldsymbol{X}_{\text{net}}(\boldsymbol{s}, t)$, where $\boldsymbol{s}$ is the first Lagrangian coordinate with domain Γ_{net}. The position of the membrane is given by $\boldsymbol{X}_{\text{mem}}(\theta, t)$, where θ is the other Lagrangian coordinate with domain Γ_{mem}. The Eulerian domain is discretized with a uniform, structured mesh. The Lagrangian membrane is discretized with a simple curvilinear mesh. The Lagrangian network is discretized with an unstructured mesh using the software *DistMesh* [Per04].

Similarly, given the fluid velocity we can interpolate this velocity field to the Lagrangian structures. The fluid velocity, in general, will be given by the appropriate momentum balance equation. In this work we will assume that the fluid is Newtonian and described by Stokes equation (inertial effects are negligible); however, the method is not restricted to this case. We denote the fluid velocity (as a function of the Eulerian coordinate $\boldsymbol{x}$) by $\boldsymbol{u}$. Interpolating to the two Lagrangian structures, we have

$$\boldsymbol{U}(\boldsymbol{s}) = \mathcal{S}^*_{\text{net}}\left[\boldsymbol{u}\right], \tag{3.10}$$

$$\boldsymbol{U}(\theta) = \mathcal{S}^*_{\text{mem}}\left[\boldsymbol{u}\right]. \tag{3.11}$$

Here, $\boldsymbol{U}(\boldsymbol{s})$ is the fluid velocity evaluated at the location $\boldsymbol{X}_{\text{net}}\left(\boldsymbol{s}, t\right)$. The velocity $\boldsymbol{U}(\theta)$ has a similar interpretation. In the standard IB framework, a no slip boundary condition is imposed on the immersed structure by moving it with the interpolated fluid velocity [Pes02]. In this work, the membrane parametrized by θ will represent the impermeable lipid membrane bounding the cell (Section 3.5), where we will stipulate a no-slip condition. However, the structure parametrized by $\boldsymbol{s}$ will represent a porous material which may move relative to the interstitial fluid, and thus has its own velocity field. Regardless, we assume that the velocity field of the porous medium has some functional dependence (denoted G) on the local fluid velocity, and we will therefore need to evaluate $\boldsymbol{v}$ on the Lagrangian structures. We may now formulate the equations of the IB method.

$$\Delta\boldsymbol{u} - \nabla p + \boldsymbol{f}_{\text{net}} + \boldsymbol{f}_{\text{mem}} = 0, \tag{3.12}$$

$$\nabla \cdot \boldsymbol{u} = 0, \tag{3.13}$$

$$\boldsymbol{f}_{\text{net}}(\boldsymbol{x}) = \mathcal{S}_{\text{net}}\left[\boldsymbol{F}_{\text{net}}\right], \tag{3.14}$$

$$\boldsymbol{f}_{\text{mem}}(\boldsymbol{x}) = \mathcal{S}_{\text{mem}}\left[\boldsymbol{F}_{\text{mem}}\right], \tag{3.15}$$

$$\frac{\partial \boldsymbol{X}(\theta, t)}{\partial t} = \mathcal{S}^*_{\text{mem}}\left[\boldsymbol{u}\right], \tag{3.16}$$

$$\frac{\partial \boldsymbol{X}(\boldsymbol{s}, t)}{\partial t} = G\left(\mathcal{S}^*_{\text{net}}\left[\boldsymbol{u}\right]\right). \tag{3.17}$$

The constitutive laws which describe $\boldsymbol{F}_{\text{net}}$ and $\boldsymbol{F}_{\text{mem}}$, and the method of their calculation, will be discussed in Sections 3.3 & 3.5.

3.2.1 Discretization of the Immersed Boundary Method

For simulation of our model, we must discretize our IB framework. The Eulerian domain in which the immersed structures are embedded is assumed to be the unit square $[0, 1] \times [0, 1]$ with periodic boundaries (or more formally, the two-torus $\mathbb{T}^2$). This is done so that we may make use of relatively simple methods for solving the fluid equations in the Eulerian domain. We discretize the unit square with a standard, uniform mesh in the x- and y-directions. The grid spacing is given by $\Delta x = 1/M_x$ and $\Delta y = 1/M_y$. The grid points are given by

$$\{\boldsymbol{x}^{nm}\} = \{(x^n, y^m)\} = \left\{\left(n\left(\Delta x - \frac{1}{2}\right), m\left(\Delta y - \frac{1}{2}\right)\right)\right\}, \tag{3.18}$$

where $1 \leq n \leq M_x$, and $1 \leq m \leq M_y$. The fact that the Eulerian grid does not conform to the geometry imposed by any immersed elastic structures is the key feature which allows the use of standard methods to solve the fluid equations. The Langrangian structures are discretized separately, in a manner which will be discussed in Sections 3.3 & 3.5. For now, it suffices to say that after discretization we have collections of Lagrangian points, $\left\{\boldsymbol{s}^i\right\}_{i=1}^{M_{\text{net}}}$ and $\left\{\theta^j\right\}_{j=1}^{M_{\text{mem}}}$, which approximate the porous medium and membrane respectively. We also know the location of each of these Lagrangian points:

$$\boldsymbol{X}^i_{\text{net}} = \boldsymbol{X}_{\text{net}}\left(\boldsymbol{s}^i, t\right), \tag{3.19}$$

$$\boldsymbol{X}^j_{\text{mem}} = \boldsymbol{X}_{\text{mem}}(\theta^j, t). \tag{3.20}$$

We note that while these locations are within the Eulerian domain, they are *not* constrained to lie on the discrete Eulerian mesh. Finally, to each discrete Lagrangian point we assign a "volume." Each discrete point in the space-filling porous material has an area dA^i, while each point on the one-dimensional membrane has a length $d\ell^j$. The determination of these discrete volumes will be discussed later when we provide the specifics of the discretization of each Lagrangian material.

Discrete Spreading and Interpolation We now address the discretization of the spread and interpolation operators (Equations (3.1) & (3.2)). The following discussion is nearly identical to that in [Pes02], and is only included here for clarity. In order to approximate the integrals in Equations (3.1) & (3.2), we must first construct an appropriate approximation to the Dirac delta distribution. We begin by defining a function $\phi : \mathbb{R} \to \mathbb{R}$ in the following piecewise manner:

$$\phi(r) = \begin{cases} 0 & : \quad |r| \geq 2 \\ \frac{1}{8}\left(5 + 2r - \sqrt{-7 - 12r - 4r^2}\right) & : \quad -2 \leq r \leq -1 \\ \frac{1}{8}\left(3 + 2r + \sqrt{1 - 4r - 4r^2}\right) & : \quad -1 \leq r \leq -0 \\ \frac{1}{8}\left(3 - 2r + \sqrt{1 + 4r - 4r^2}\right) & : \quad 0 \leq r \leq 1 \\ \frac{1}{8}\left(5 - 2r - \sqrt{-7 + 12r - 4r^2}\right) & : \quad 1 \leq r \leq 2 \end{cases} \tag{3.21}$$

It is shown in [Pes02] that this function may be uniquely derived from a collection of five properties. We will not go into the details here, but for now it suffices to note that

1. $\phi(r) = 0$ for $r \geq 2$, and

2. $\sum\limits_{\ell \in \mathbb{N}} \phi(r - j) = 1$ for all $r \in \mathbb{R}$.

We now define approximate (one-dimensional) delta functions by scaling ϕ according to the spacing of our Eulerian mesh:

$$\delta_{\Delta x}(x) = \frac{1}{\Delta x}\phi\left(\frac{x}{\Delta x}\right), \text{ and } \delta_{\Delta y}(y) = \frac{1}{\Delta y}\phi\left(\frac{x}{\Delta y}\right). \tag{3.22}$$

In Figure 3.2, we illustrate the function ϕ as well as $\delta_{\Delta x}$ for $\Delta x = 1/2$ and $\Delta x = 1/4$. We pause here to remark on the aforementioned properties of ϕ and their implication for the approximate delta functions. First, Property 1 ensures that for any $r \in \mathbb{R}$, the translated function

$$\delta_{\Delta x}\left(x - r\right).$$

is supported on exactly four points x^n in our Eulerian discretization. This will greatly improve computational efficiency, as the vast majority of terms in the discrete convolution integrals will be zero. Second, Property 2 ensures that for any $r \in \mathbb{R}$,

$$\sum_{n=1}^{M_x} \delta_{\Delta x}(x^n - r)\,\Delta x = 1. \tag{3.23}$$

This fact will ensure that our discrete spread and interpolation operators satisfy a discrete form of the adjoint property demonstrated in Equation (3.3).

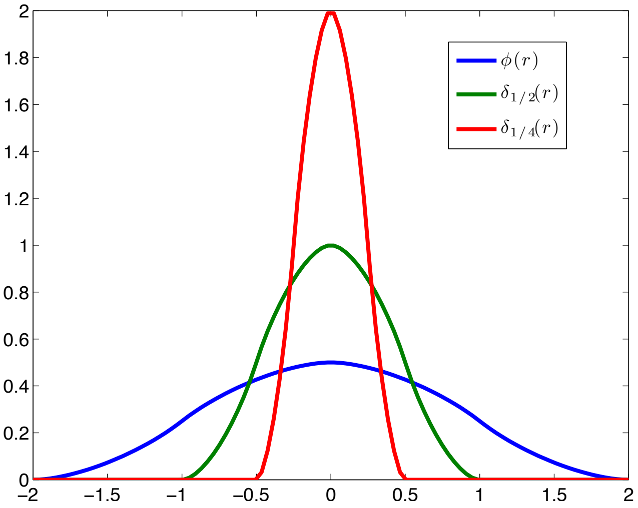

Figure 3.2: The function ϕ and two approximate delta functions $\delta_{\Delta x}$ are shown.

Finally, we define the *two-dimensional* approximate delta function via

$$\delta_2(\boldsymbol{x}) = \delta_{\Delta x}(\boldsymbol{x}\cdot\hat{x})\delta_{\Delta y}(\boldsymbol{x}\cdot\hat{y}). \tag{3.24}$$

This allows us to define the discrete spread and interpolation operators. For a field $\boldsymbol{F}_{\text{net}}$ defined on the Lagrangian material parametrized by $\boldsymbol{s}$, we define $\boldsymbol{F}^i_{\text{net}} = \boldsymbol{F}_{\text{net}}(\boldsymbol{s}^i)$. We spread this field to the Eulerian grid via

$$\boldsymbol{f}_{\text{net}}(x^n, y^m) = \boldsymbol{f}^{nm}_{\text{net}} = \mathcal{S}_{\text{net}}\boldsymbol{F}_{\text{net}} = \sum_{i=1}^{M_{\text{net}}} \boldsymbol{F}^i_{\text{net}}\delta_2\left(\boldsymbol{X}^i_{\text{net}} - \boldsymbol{x}^{nm}\right) dA^i. \tag{3.25}$$

Similarly, for any field $\boldsymbol{u}$ defined on the Eulerian grid, we have $\boldsymbol{u}^{nm} = \boldsymbol{u}(\boldsymbol{x}^{nm})$, and we interpolate this to the triangulated Lagrangian structure via

$$\boldsymbol{U}(\boldsymbol{s}^i) = \boldsymbol{U}^i = \mathcal{S}^*_{\text{net}}\boldsymbol{u} = \sum_{n=1,m=1}^{M_x,M_y} \boldsymbol{u}^{nm}\delta_2\left(\boldsymbol{x}^{nm} - \boldsymbol{X}^i_{\text{net}}\right)\Delta x\Delta y. \tag{3.26}$$

Due to the compact support of the function ϕ, the discrete sums in Equations (3.25) & (3.26) contain numerous zero terms and may be optimized for computation. For a given Lagrangian node at position $\boldsymbol{X}^i_{\text{net}}$, the two-dimensional approximate delta function is supported on a four-by-four patch of Eulerian grid points that surround $\boldsymbol{X}^i_{\text{net}}$. This is illustrated in Figure 3.3.

We may define the spread and interpolation operators for the one-dimensional membrane in a completely analogous way. For a force density exerted on the fluid by the membrane $\boldsymbol{F}_{\text{mem}}(\theta)$, we define $\boldsymbol{F}^j_{\text{mem}} = \boldsymbol{F}_{\text{mem}}(\theta^j)$, and

$$\boldsymbol{f}_{\text{mem}}(x^n, y^m) = \boldsymbol{f}^{nm}_{\text{mem}} = \mathcal{S}_{\text{mem}}\boldsymbol{F}_{\text{mem}} = \sum_{j=1}^{M_{\text{mem}}} \boldsymbol{F}^j_{\text{mem}}\delta_2\left(\boldsymbol{X}^j_{\text{mem}} - \boldsymbol{x}^{nm}\right) d\ell^j. \tag{3.27}$$

Similarly, the fluid velocity interpolated to the membrane location is given by

$$\boldsymbol{U}_{\text{mem}}(\theta^j) \approx \boldsymbol{U}^j_{\text{mem}} = \mathcal{S}^*_{\text{mem}}\boldsymbol{u} = \sum_{n=1,m=1}^{M_x,M_y} \boldsymbol{u}^{nm}\delta_2\left(\boldsymbol{x}^{nm} - \boldsymbol{X}^j_{\text{mem}}\right)\Delta x\Delta y. \tag{3.28}$$

Figure 3.3 depicts how information from a given Lagrangian node is spread to the surrounding four-by-four patch of Eulerian grid points. Similarly, information from the same patch of Eulerian grid that is interpolated to the Lagrangian node via a weighted average. Thus, through the two spreading operators, we can calculate the total force on the fluid

$$\boldsymbol{f} = \boldsymbol{f}_{\text{net}} + \boldsymbol{f}_{\text{mem}} = \mathcal{S}_{\text{net}}\boldsymbol{F}_{\text{net}} + \mathcal{S}_{\text{mem}}\boldsymbol{F}_{\text{mem}}. \tag{3.29}$$

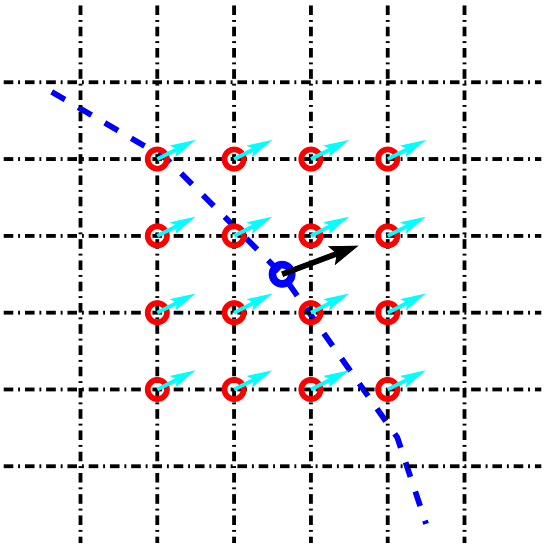

Figure 3.3: Footprint of the spreading and interpolating operators ($\mathcal{S}$ and $\mathcal{S}^*$). The Eulerian grid is shown in dashed black. A small set of the Lagrangian structure is shown in blue, with a single node highlighted. A vector quantiy at the Lagrangian node (illustrated as a black vector) may be spread to the neighboring Eulerian grid points shown in red. Similarly, data from these red nodes (illustrated as cyan vectors) may be interpolated to the highlighted Lagrangian node.

3.2.2 Solving the Fluid Equations

Now that we have the machinery to represent the forces that the immersed structures exert on the fluid, we must develop a method to solve for the velocity of the interstitial fluid. The governing equation of the fluid is the forced Stokes equation. Generically, this has the form

$$\mu \Delta \boldsymbol{u} - \nabla p = -\boldsymbol{f}, \quad \boldsymbol{x} \in \mathbb{T}^2 \tag{3.30}$$

$$\nabla \cdot \boldsymbol{u} = 0, \quad \boldsymbol{x} \in \mathbb{T}^2. \tag{3.31}$$

We solve this via a standard "Pressure Poisson" method. Taking the divergence of Equation (3.30) and invoking the incompressibility of the fluid, we arrive at the equation

$$\Delta p = \nabla \cdot \boldsymbol{f}, \quad \boldsymbol{x} \in \mathbb{T}^2. \tag{3.32}$$

This is known as the Pressure Poisson equation (PPE), and in the case of our domain may be readily solved for the pressure p. It is true that the pressure is only defined up to an arbitrary additive constant, but as the physics of our system only depend on the *gradient* of p, this constant is irrelevant. Given that p is determined, so is ∇p, and substituting back into Equation (3.30) we have

$$\Delta \boldsymbol{u} = \frac{1}{\mu} \left(\nabla p - \boldsymbol{f} \right), \quad \boldsymbol{x} \in \mathbb{T}^2. \tag{3.33}$$

Again, we must solve a Poisson equation to recover the fluid velocity $\boldsymbol{u}$.

Now, we will exploit the fact that both Equations (3.32) & (3.33) are rather simple to solve in Fourier space. If the function $\boldsymbol{f}$ has Fourier decomposition

$$\boldsymbol{f}(\boldsymbol{x}) = \sum_{\boldsymbol{k} \in \mathbb{N}^2} \hat{\boldsymbol{f}}_{\boldsymbol{k}} e^{i(\boldsymbol{x} \cdot \boldsymbol{k})}, \tag{3.34}$$

then a relatively simple calculation shows

$$\nabla \cdot \boldsymbol{f} = \sum_{\boldsymbol{k} \in \mathbb{N}^2} i\boldsymbol{k} \cdot \hat{\boldsymbol{f}}_{\boldsymbol{k}} e^{i(\boldsymbol{x} \cdot \boldsymbol{k})}. \tag{3.35}$$

Therefore, we may solve Equation (3.32) for the pressure

$$p(\boldsymbol{x}) = \sum_{\boldsymbol{k} \neq \boldsymbol{0}} -\frac{i\boldsymbol{k} \cdot \hat{\boldsymbol{f}}_{\boldsymbol{k}}}{|\boldsymbol{k}|^2} e^{i(\boldsymbol{x} \cdot \boldsymbol{k})}. \tag{3.36}$$

Notice that this Fourier representation of the pressure is valid as long as $\boldsymbol{k} \neq \boldsymbol{0}$ (the vector of all zeros). However, a simple calculation shows that Equation (3.30) is a well posed problem only if the forcing function $\boldsymbol{f}$ has zero integral. This is equivalent to the condition $\boldsymbol{f}_{\boldsymbol{0}} = \boldsymbol{0}$. Therefore, we may safely represent the pressure gradient as

$$\nabla p(\boldsymbol{x}) = \sum_{\boldsymbol{k} \neq \boldsymbol{0}} \frac{\boldsymbol{k}}{|\boldsymbol{k}|^2} \boldsymbol{k} \cdot \hat{\boldsymbol{f}}_{\boldsymbol{k}} e^{i(\boldsymbol{x} \cdot \boldsymbol{k})}. \tag{3.37}$$

Since we have a Fourier representation of $\boldsymbol{f}$ and ∇p, Equation (3.33) can readily be solved for the velocity $\boldsymbol{u}$:

$$\boldsymbol{u}(\boldsymbol{x}) = \frac{1}{\mu} \sum_{\boldsymbol{k} \neq \boldsymbol{0}} \left(\frac{\hat{\boldsymbol{f}}_{\boldsymbol{k}}}{|\boldsymbol{k}|^2} - \frac{\boldsymbol{k}}{|\boldsymbol{k}|^4} \boldsymbol{k} \cdot \hat{\boldsymbol{f}}_{\boldsymbol{k}} \right) e^{i(\boldsymbol{x} \cdot \boldsymbol{k})}. \tag{3.38}$$

For notational convinience, we define

$$\boldsymbol{u}_{\boldsymbol{k}} = \frac{1}{\mu} \left(\frac{\hat{\boldsymbol{f}}_{\boldsymbol{k}}}{|\boldsymbol{k}|^2} - \frac{\boldsymbol{k}}{|\boldsymbol{k}|^4} \boldsymbol{k} \cdot \hat{\boldsymbol{f}}_{\boldsymbol{k}} \right). \tag{3.39}$$

Now, our IB implementation gives us an approximation to the forces exerted on the fluid given by Equations (3.4) & (3.25). Given a discrete forcing function $\boldsymbol{f}^{nm}$ generated by the spread operator, we use a Fast Fourier Transform (FFT) to calculate $\hat{\boldsymbol{f}}_{\boldsymbol{k}}$ [Fri05]. This results in a truncated Fourier series representation of the forcing applied to the fluid in the Eulerian domain. Equation (3.38) may be used to calculate the truncated Fourier series of the fluid velocity that results from this forcing. Equation (3.36) may similarly be used to calculate the pressure. Finally, we use an Inverse FFT to recover the approximate fluid velocity and pressure at the nodes of the Eulerian grid

$$p^{nm} = p(x^n, y^m), \tag{3.40}$$

$$\boldsymbol{u}^{nm} = \boldsymbol{u}(x^n, y^m). \tag{3.41}$$

This is an example of a so-called spectral method [Tre00]. We will not discuss the various drawbacks and benefits of such a method in this work. However, the numerical convergence of this method for solving the forced Stokes equation is shown for a simple test problem in Appendix A.

3.3 Poro-Elastic Description of Cell Interior

To describe the mechanics of the cell interior, we begin with a two-phase flow model, which is often used to describe multicomponent mixtures (gels) that consist of an elastic network immersed in a viscous fluid [Cog10]. Both phases may exist simultaneously at all points within some spatial domain. The two phases are often referred to as the *network* and the *sol*. As the names imply, we will assume that the network phase behaves as an elastic solid, while the sol phase behaves as a viscous fluid. In the context of our model, the elastic network will represent the cytoskeleton of *physarum*, while the viscous fluid will represent interstitial cytosol. Each phase moves with its own velocity field, and at any point within the domain, the composition of the mixture is described by the volume fractions of the different phases. The velocity of the fluid sol is now denoted by $\boldsymbol{u}_f$. This is to distinguish it from the network velocity, $\boldsymbol{u}_{\text{net}}$. The volume fraction of the network phase is φ. Since the volume fraction of network and sol must sum to one, the volume fraction of the fluid is $1-\varphi$. We assume constant total density, and thus mass conservation leads to a volume-averaged incompressibility constraint. Due to our interest in describing phenomena on a cellular length scale, we assume that inertia is negligible. Therefore, the dynamics of both phases may be described by the appropriate force density balance law. The force density balance for each phase and the volume-averaged incompressibility constraint are given by

$$\nabla \cdot \underline{\boldsymbol{\sigma}}_f - (1-\varphi)\nabla p + \xi\left(\boldsymbol{u}_{\text{net}} - \boldsymbol{u}_f\right) = 0, \tag{3.42}$$

$$\nabla \cdot \underline{\boldsymbol{\sigma}}_e - \varphi \nabla p + \xi\left(\boldsymbol{u}_f - \boldsymbol{u}_{\text{net}}\right) = 0, \tag{3.43}$$

$$\nabla \cdot \left(\varphi \boldsymbol{u}_{\text{net}} + (1-\varphi)\,\boldsymbol{u}_f\right) = 0. \tag{3.44}$$

Here, $\boldsymbol{u}_f$ and $\boldsymbol{u}_{\text{net}}$ are the velocity field of the fluid and network phases respectively, while p denotes the pressure within the gel. The parameter ξ is a drag parameter that mechanically couples the network and sol, and quantifies the force density associated with relative motion of the two phases past one another. The tensors $\underline{\boldsymbol{\sigma}}_f$ and $\underline{\boldsymbol{\sigma}}_e$ represent the viscous fluid stress within the cytosol and the elastic stress within the cytoskeleton, respectively. The fluid stress is given by the standard Newtonian fluid stress

$$\underline{\boldsymbol{\sigma}}_f = \mu \left(\nabla \boldsymbol{u}_f + \nabla \boldsymbol{u}_f^T \right) + \lambda \left(\nabla \cdot \boldsymbol{u}_f \right) \mathbb{I}, \tag{3.45}$$

where μ is the fluid shear viscosity, λ is the second coefficient of viscosity, and $\mathbb{I}$ is the identity tensor. We will discuss $\underline{\boldsymbol{\sigma}}_e$ in more detail below, but for now, we note that it is derived from an approximation of the stress due to deformation in a linear elastic solid.

Following other theoretical works that have modeled cytoskeleton [Lev09], we make the simplifying assumption that $\varphi \ll 1$. In this limit, Equation (3.44) reduces to

$$\nabla \cdot \boldsymbol{u}_f = 0, \tag{3.46}$$

which is the well known incompressibility constraint applied to the interstitial fluid. The constraint that the fluid velocity is incompressible simplifies the form of the fluid stress. Also, in the limit that $\varphi \ll 1$, the pressure gradient disappears from the force density balance on the network, Equation (3.43). In this case, the equations that describe the dynamics of the gel reduce to

$$\Delta \boldsymbol{u}_f - \nabla p + \xi \left(\boldsymbol{u}_{\text{net}} - \boldsymbol{u}_f \right) = 0, \tag{3.47}$$

$$\nabla \cdot \underline{\boldsymbol{\sigma}}_e + \xi \left(\boldsymbol{u}_f - \boldsymbol{u}_{\text{net}} \right) = 0, \tag{3.48}$$

$$\nabla \cdot \boldsymbol{u}_f = 0. \tag{3.49}$$

Notice that Equations (3.47)–(3.49) effectively describe the cell interior as a poro-elastic material. These equations do *appear* to differ somewhat from the classical description of poro-elasticity, as discussed in [Bio41]. However, by assuming that viscous effects on the fluid are negligible and by adding Equations (3.42) & (3.43), one may eliminate the drag term from the force density balance equations. In this case, elastic stresses within the network are balanced by the pressure within the gel. Finally, through a rearrangement of Equation (3.42), one may derive an equation which resembles Darcy's law governing the fluid velocity. This exercise yields the system

$$\nabla \cdot \underline{\boldsymbol{\sigma}}_e - \nabla p = 0$$

$$\mu \left(\boldsymbol{u}_f - \boldsymbol{u}_{\text{net}} \right) = -\kappa \nabla p.$$

These equations are equivalent to the poro-elastic theory derived by Biot [Bio41], and the parameter $\kappa = \mu(1 - \varphi)/\xi$ is the Darcy permeability of the network. In Chapter 4, when we choose the paramter ξ for simulation of the model, it will be done by choosing a permeability consistent with the literature and evaluating ξ via this relation. The Darcy permeability of cytoskeletal actin networks has been estimated [Ker09], and we will calculate ξ to be consistent with permeability values in the literature. We finally note that this reduction is purely expository; we will not be using the poro-elastic model of Biot. We may wish to simulate scenarios where regions of viscous fluid are in close proximity to porous media, and as such, it would be inappropriate to omit the viscous term from Equation (3.47).

3.3.1 Two-Dimensional Reduction

In the experimental setup used in [Mat08], as well as that used by our collaborators (Dr. Juan Carlos del Álamo and Shun Zhang, UC San Diego), the migrating *physarum* plasodium is confined to a narrow gap. The length scale in the z-direction ($\sim$ 20 µm) is significantly smaller than the standard length scales in the x- and y-directions ($\sim$ 400 µm and $\sim$ 50 µm respectively). For this reason, we average across the z-direction and reduce the dimensionality of the model. This will have the added benefit of greatly simplifying computation, as simulation of three dimensional dynamics is more computationally expensive. We begin by expanding Equation (3.48) into its three constitutive equations. In the region $0 < z < d$, we have

$$\partial_x \sigma^{xx} + \partial_y \sigma^{yx} + \partial_z \sigma^{zx} + \xi \left(u_f^x - u_{\text{net}}^x \right) = 0, \tag{3.50}$$

$$\partial_x \sigma^{xy} + \partial_y \sigma^{yy} + \partial_z \sigma^{zy} + \xi \left(u_f^y - u_{\text{net}}^y \right) = 0, \tag{3.51}$$

$$\partial_x \sigma^{xz} + \partial_y \sigma^{yz} + \partial_z \sigma^{zz} + \xi \left(u_f^z - u_{\text{net}}^z \right) = 0. \tag{3.52}$$

Here, superscripts denote components of the vector and tensor quantities in the x-, y-, and z-directions. Later, in Section 3.4, we envision a *surface force* applied to the basal boundary of the cytoskeleton by adhesive structures linked to the substrate. This leads to a boundary condition on the force balance law

$$\underline{\boldsymbol{\sigma}} \cdot \hat{z} = \boldsymbol{f} \ \text{ at } z = 0. \tag{3.53}$$

For simplicity, we will assume a no stress condition ($\underline{\boldsymbol{\sigma}} \cdot \hat{z} = \mathbf{0}$) at $z = d$. We could assume a symmetric stress at the boundary $z = d$, but it would not alter the analysis. We also make the assumption that there is no fluid or network displacement in the z-direction.

From these simplifying assumptions, we may simply discard Equation (3.52). We now integrate Equations (3.50) & (3.51) in the z-direction,

$$\int_0^d \left(\partial_x \sigma^{xx} + \partial_y \sigma^{yx} + \partial_z \sigma^{zx} + \xi \left(u_f^x - u_{\text{net}}^x\right)\right) dz = 0, \tag{3.54}$$

$$\int_0^d \left(\partial_x \sigma^{xy} + \partial_y \sigma^{yy} + \partial_z \sigma^{zy} + \xi \left(u_f^y - u_{\text{net}}^y\right)\right) dz = 0. \tag{3.55}$$

Assuming that all components of σ are sufficiently smooth, we may exchange the order of integration and differentiation and write

$$d \times \left(\partial_x \overline{\sigma}^{xx} + \partial_y \overline{\sigma}^{yx} + \xi \left(\overline{u}_f^x - \overline{u}_{\text{net}}^x\right)\right) + f^x = 0, \tag{3.56}$$

$$d \times \left(\partial_x \overline{\sigma}^{xy} + \partial_y \overline{\sigma}^{yy} + \xi \left(\overline{u}_f^y - \overline{u}_{\text{net}}^y\right)\right) + f^y = 0. \tag{3.57}$$

Here, the notation $\overline{*}$ denotes the average over the z-direction

$$\overline{*} = \frac{1}{d} \int_0^d * \, dz. \tag{3.58}$$

Equations (3.56) & (3.57) are equivalent to the two-dimensional vector equation

$$\nabla_{2D} \cdot \left(\underline{\boldsymbol{\sigma}}_{2D}\right) + \boldsymbol{f}_{2D} + \xi_{2D} \left(\overline{\boldsymbol{u}}_f - \overline{\boldsymbol{u}}_{\text{net}}\right) = 0. \tag{3.59}$$

Here, ∇_{2D} is the two-dimensional divergence, $\underline{\boldsymbol{\sigma}}_{2D}$ is the two-dimensional stress, with units of *force per unit length*, and $\overline{\boldsymbol{u}}_f$ and $\overline{\boldsymbol{u}}_{\text{net}}$ are the average fluid and network velocities *in the plane.* $\boldsymbol{f}_{2D}$ is simply the projection of $\boldsymbol{f}$ onto the xy-plane. Note that in Equation (3.53), $\boldsymbol{f}$ represented a *surface force* applied to the boundary of the cytoskeleton. However, in the two-dimensional averaged model, this boundary force enters the force balance directly. Finally, $\xi_{2D} = d \times \xi$ is the two-dimensional drag parameter with units of momentum per unit volume. We draw particular attention to the units of ξ_{2D} due to the fact that we will calculate a desired drag parameter ξ given the Darcy permeability of a particular network. However, in order to analyze our two-dimensional model, we must then calculate the appropriate ξ_{2D} using the characteristic thickness of the gel (d).

As in Chapter 2, we will assume that the two-dimensional average fluid velocity is incompressible (this is a result of our thin gap approximation). Therefore, Equation (3.47) has a relatively straightforward reduction to two dimension, and we will not go through the calculation. It is a simple exercise to arrive at our full system of equations

$$\mu_{2D}\Delta_{2D}\overline{\boldsymbol{u}}_f - \nabla p_{2D} + \xi_{2D}\left(\overline{\boldsymbol{u}}_{\text{net}} - \overline{\boldsymbol{u}}_f\right) = 0, \tag{3.60}$$

$$\nabla_{2D} \cdot \underline{\boldsymbol{\sigma}}_{2D} + \xi_{2D}\left(\overline{\boldsymbol{u}}_f - \overline{\boldsymbol{u}}_{\text{net}}\right) + \boldsymbol{f}_{2D} = 0, \tag{3.61}$$

$$\nabla_{2D} \cdot \overline{\boldsymbol{u}}_f = 0. \tag{3.62}$$

At this point, we will drop the subscripts and overline notations that distinguish the two-dimensional reduction of our model. All work from this point will be done with the understanding that we are discussing the reduced model. The only exception to this will be when assigning values to parameters in Chapter 4. In this case, distinguishing notation will be used.

3.3.2 Elastic Forces

We now focus on the treatment of the elastic network that is immersed in the fluid. Assuming (for the moment) no boundary force, we may rewrite Equations (3.60), (3.62) and (3.62) as

$$\Delta \boldsymbol{u}_f - \nabla p - \boldsymbol{f}_{\text{drag}} = 0, \tag{3.63}$$

$$\boldsymbol{f}_e + \boldsymbol{f}_{\text{drag}} = 0, \tag{3.64}$$

$$\nabla \cdot \boldsymbol{u}_f = 0. \tag{3.65}$$

Here, the force due to elasticity is denoted $\boldsymbol{f}_e = \nabla \cdot \underline{\boldsymbol{\sigma}}_e$, while the drag force due to relative motion is denoted $\boldsymbol{f}_{\text{drag}} = \xi\left(\boldsymbol{u}_f - \boldsymbol{u}_{\text{net}}\right)$. Furthermore, we note that the balance of forces on the immersed network (Equation (3.64)) must hold in the Lagrangian coordinate system as well. This allows us to formulate our model in a mixed coordinate system:

$$\Delta \boldsymbol{u}_f - \nabla p - \boldsymbol{f}_{\text{drag}} = 0, \tag{3.66}$$

$$\boldsymbol{F}_e + \boldsymbol{F}_{\text{drag}} = 0, \tag{3.67}$$

$$\nabla \cdot \boldsymbol{u}_f = 0, \tag{3.68}$$

where $\boldsymbol{F}_{\text{drag}} = \xi\left(\mathcal{S}^*_{\text{net}}\boldsymbol{u}_f - \boldsymbol{U}_{\text{net}}\right)$.

Having rewritten the equations of motion in this mixed framework, all that remains is to specify the constitutive law for the elastic forces within the network $\boldsymbol{F}_e$. We assume that the elastic response of the network is characterized by an elastic energy density functional $W(\mathcal{E})$, which depends only on the strain in the network $\mathcal{E}$. From this point, we could define the elastic stress within the network via

$$\underline{\boldsymbol{\sigma}}_e = \frac{\partial W}{\partial \mathcal{E}}. \tag{3.69}$$

However, it will be more convenient to directly calculate the elastic forces from a variational derivative. From the elastic energy density, we may compute the total elastic energy in the network

$$E_e = \int\limits_{\Gamma_{\text{net}}} W \, d\boldsymbol{s}. \tag{3.70}$$

Finally, we may calculate the elastic force density in the network

$$\boldsymbol{F}_e = -\frac{\mathfrak{d} E^e}{\mathfrak{d} X}. \tag{3.71}$$

Here we have used the symbol $\mathfrak{d}$ to denote a variational derivative, as the symbol δ is used to denote a Dirac delta distribution.

Thus far, the model makes no assumptions as to the form of the elastic energy density W. Given the lack of knowledge about the elastic response of the intracellular cytoskeleton of migrating plasmodia, we do not attempt to choose a particular constitutive law based on experimental observation. Instead, we will develop a nonlinear elastic model in the following section and show that in the limit of small deformation, our model reproduces a linearly elastic material. In the limit of infinitesimal strain, a linearly elastic material is defined by

$$W(\mathcal{E}) = \mu_{\text{E}} \text{tr}(\mathcal{E}^2) + \frac{\lambda_{\text{E}}}{2} \left[\text{tr}(\mathcal{E})\right]^2. \tag{3.72}$$

Here, μ_{E} denotes the elastic shear modulus of the network, and λ_{E} is the second Lamè constant. In the small strain limit, the strain $\mathcal{E}$ is given by the symmetric part of the displacement gradient

$$\mathcal{E} = \frac{1}{2}\left(\nabla \boldsymbol{q} + \nabla \boldsymbol{q}^T\right), \tag{3.73}$$

where $\boldsymbol{q} = \boldsymbol{X}_{\text{net}}(\boldsymbol{s}, t) - \boldsymbol{s}$ is the displacement vector of the Lagrangian material from reference. We end by noting that our elasticity model is limited in the materials that it may reproduce, and in the following sections, $\mu_{\text{E}} = \lambda_{\text{E}}$ in all cases (See Appendix B).

3.3.3 Discretization of Poro-Elastic Material

We now discuss how we will discretize our poro-elastic model (Equations (3.66)–(3.68)), and the methods by which the approximate elastic force is calculated. Naively, one may assume that the simplest way to discretize a continuum of elastic material is by representing it as a discrete collection of material points connected by elastic springs. Representing Lagrangian mechanics via a network of springs is common in immersed boundary applications [Pes02]. This is indeed the way in which we develop our model of the cell interior. However, it should be noted that this is not a general method of modeling elastic solids, and may not be suitable in all cases.

Representing elastic continuum mechanics via a network of springs has been used in Lattice-Spring Models (LSMs) [OS02, Hre41]. Due to the fact that ruptures can be simply captured by breaking elastic links (or setting parameters to zero locally), the use of LSMs has traditionally been popular in studies of fracture in solid mechanics [Mea87, Cur90, Ter86, Her89]. However, a known limitation of LSM stems from the use of springs which produce force in the direction of strain. Because of this, only a one parameter family of elastic solids with a fixed Poisson ratio can be modeled. Choosing either μ_E or λ_E in Equation (3.72) dictates the other based on network topology. This limitation can be removed through several methods, including the introduction of bending springs or shear springs connecting material points, but care must be taken to maintain rotational invariance of the model [Has89, Zha12]. A relatively recent literature review of LSMs can be found in [OS02]. The stiffness coefficients and the resting lengths of these springs can be related to the elastic moduli of an isotropic linear elastic material by comparing the discrete and continuous strain energies. Such calculations for linear elastic materials discretized with regular square and triangular lattices can be found in [OS02]. In Appendix B we go through a similar calculation for the network topology we use in our model.

Since we will model elasticity of the cytoskeleton in a cell with arbitrary geometry, we extend a Lattice-Spring-like model to an unstructured mesh. A special meshing procedure is used to guarantee isotropy of the elastic material. We use the Distmesh algorithm because it generates unstructured meshes where the side length of the triangular elements is almost equal [Per04]. To compute a triangulation, the algorithm assumes the points are connected by springs with repulsive forces. An iterative procedure for minimizing the associated energy generates a set of points that are triangulated by a Delaunay algorithm. The result of this equilibration process is a spring network that approximates an isotropic material (at least initially). For large deformations, we do not necessarily expect this initial mesh to remain isotropic. The meshing algorithm produces a set of Lagrangian material points, $\left\{\boldsymbol{s}^i\right\}_{i=1}^{M_{\text{net}}}$, and a triangulation on those points, $\left\{\Delta S^k\right\}$. Recall that we defined the Eulerian position of each material point

$$\boldsymbol{X}^i_{\text{net}}(t) = \boldsymbol{X}_{\text{net}}(\boldsymbol{s}^i, t) \tag{3.74}$$

and assume that initially, $\boldsymbol{X}^i_{\text{net}}(0) = \boldsymbol{s}^i$ (that is, the material is initially in reference configuration). To each discrete point, we associate a discrete area dA^i, which is defined to be the sum of one third the area of each triangle for which $\boldsymbol{s}^i$ is a vertex,

$$dA^i = \frac{1}{3} \sum_{s_i \in \Delta S^k} \left| \Delta S_k \right|. \tag{3.75}$$

Finally, to each edge in the triangulation, we assign a reference length. For the link connecting points $\boldsymbol{s}^i$ and $\boldsymbol{s}^j$, we have

$$d\ell^{ij} = \left| \boldsymbol{X}^i_{\text{net}}(0) - \boldsymbol{X}^j_{\text{net}}(0) \right|. \tag{3.76}$$

With these quantities we are able to calculate the discrete approximation of the elastic force within the network.

Discrete Elastic Force The edges of the triangulation $\{\Delta S_k\}$ are modeled as discrete springs with coefficients k^{ij} and resting lengths $d\ell^{ij}$. The strain energy in the elastic link connecting $\boldsymbol{X}^i_{\text{net}}$ to $\boldsymbol{X}^j_{\text{net}}$ is given by

$$e^{ij} = \frac{k^{ij}\, d\ell^{ij}}{2} \left(\frac{|\boldsymbol{X}^i_{\text{net}} - \boldsymbol{X}^j_{\text{net}}| - d\ell^{ij}}{d\ell^{ij}} \right)^2, \tag{3.77}$$

and we refer to this quantity as the *link energy*. We note here that the parameter k^{ij} has units of force. The total elastic energy at a point $\boldsymbol{X}^i_{\text{net}}$ is

$$E^i = \frac{1}{2} \sum_j e^{ij}, \tag{3.78}$$

where it is understood that e^{ij} is zero unless $\boldsymbol{X}^j_{\text{net}}$ is connected to $\boldsymbol{X}^i_{\text{net}}$ by the triangulation. We refer to this E^i as the node energy. The factor of $1/2$ which appears in Equation (3.78) is included to ensure that summing the link energies or node energies over the network results in same total discrete elastic energy,

$$E_e = \sum_i E^i = \sum_{i,j} e^{ij}. \tag{3.79}$$

From Equation (3.79), we compute the elastic force at the node $\boldsymbol{X}^i_{\text{net}}$ as

$$\widehat{\boldsymbol{F}^i} = -\frac{\partial E_e}{\partial \boldsymbol{X}^i_{\text{net}}} = \sum_j -\frac{\partial e^{ij}}{\partial \boldsymbol{X}_i}. \tag{3.80}$$

Finally, we define the force *density* at node $\boldsymbol{X}^i_{\text{net}}$ by dividing force by the associated area of the node,

$$\boldsymbol{F}^i = \frac{1}{dA^i}\hat{\boldsymbol{F}}^i. \tag{3.81}$$

Note that this force density is analogous to a discrete form of the variational derivative given in Equation (3.71). From Equation (3.77), we may calculate the force density exerted on node $\boldsymbol{X}^i_{\text{net}}$ by the single elastic spring connected to node $\boldsymbol{X}^j_{\text{net}}$,

$$-\frac{1}{dA^i}\frac{\partial e^{ij}}{\partial \boldsymbol{X}^i_{\text{net}}} = -\frac{k^{ij}}{dA^i}\left(\frac{|\boldsymbol{X}^i_{\text{net}} - \boldsymbol{X}^j_{\text{net}}| - d\ell^{ij}}{d\ell^{ij}}\right)\frac{\boldsymbol{X}^j_{\text{net}} - \boldsymbol{X}^i_{\text{net}}}{|\boldsymbol{X}^i_{\text{net}} - \boldsymbol{X}^j_{\text{net}}|}. \tag{3.82}$$

We note that the spring constant k^{ij} must be chosen so that the discrete strain energy density from our lattice-spring-like model is consistent with the continuous strain energy density for linear elasticity, Equation (3.72). We set each spring constant within the network according to the formula

$$k^{ij} = \frac{8\lambda_E}{3\,d\ell^{ij}}\left(\frac{dA^i + dA^j}{2}\right). \tag{3.83}$$

A detailed derivation of the above formula can be found in Appendix B. Note that this expression assumes a 2-D elastic material, but an analogous formula could be derived for 3-D.

Time Integration We now have the framework to simulate a poro-elastic material. Before we describe the time stepping scheme used, we note that by rearrangement of Equation (3.67) and substituting the defintion of $\boldsymbol{F}_{\text{drag}}$, we arrive at a formula for the time evolution of the elastic network

$$\frac{d\boldsymbol{X}_{\text{net}}}{dt} = \boldsymbol{U}_{\text{net}} = \frac{1}{\xi}\boldsymbol{F}_e + \mathcal{S}^*_{\text{net}}\boldsymbol{u}_f. \tag{3.84}$$

After discretization of the Lagrangian and Eulerian domains, the system consisting of Equations (3.66)–(3.68) is evolved in the following way:

1. Given a configuration $\boldsymbol{X}^i$ of the network, evaluate the elastic force $\boldsymbol{F}_e(\boldsymbol{s}^i)$ via Equations (3.80) & (3.81).
2. Given the elastic force on the network, solve for the force due to drag via Equation (3.67).
3. Given the force due to drag ($\boldsymbol{F}_{\text{drag}}$), spread it to the Eulerian grid: $\boldsymbol{f}_{\text{drag}} = \mathcal{S}_{\text{net}}\boldsymbol{F}_{\text{drag}}$.

4. Given the force due to drag on the fluid, solve the Stokes problem for fluid velocity via Equation (3.38).
5. Interpolate the fluid velocity back to the Lagrangian grid.
6. Evaluate the network velocity $\boldsymbol{U}^i_{\text{net}}$ via Equation (3.84).
7. Evolve the network configuration via the forward Euler scheme $\boldsymbol{X}^i_{\text{net}}(t+\Delta t) = \boldsymbol{X}^i_{\text{net}}(t) + \Delta t \boldsymbol{U}^i_{\text{net}}$.

3.3.4 Numerical Validation

We now simulate a simple test problem to validate our IB formulation of the equations of poro-elasticity Equations (3.60)–(3.62). For our test problem, we consider a circular elastic network of radius R that is expanded uniformly in the radial direction. We will compare the results of our IB simulation to the solution of the equations of linear elasticity in the small strain limit.

For a linearly elastic material deformed as described, we know that the displacement vector $\boldsymbol{q}$ will have only radial component and will be a function of only the radial coordinate

$$\boldsymbol{q} = q(r)\hat{r}. \tag{3.85}$$

From this, we may calculate the displacement gradient, which will have components in the θ direction

$$\nabla \boldsymbol{q} = q'(r)\hat{r}\hat{r} + \frac{q(r)}{r}\hat{\theta}\hat{\theta}. \tag{3.86}$$

Since this is a symmetric tensor, we immediately know the linear strain

$$\mathcal{E} = q'(r)\hat{r}\hat{r} + \frac{q(r)}{r}\hat{\theta}\hat{\theta}. \tag{3.87}$$

From Equation (3.69), we may calculate the stress due to this deformation

$$\underline{\boldsymbol{\sigma}}_e = 2\mu_{\text{E}}\left(q'(r)\hat{r}\hat{r} + \frac{q(r)}{r}\hat{\theta}\hat{\theta}\right) + \lambda_{\text{E}}\left(q'(r) + \frac{q(r)}{r}\right)\mathbb{I}. \tag{3.88}$$

Finally, a calculation yields the Eulerian elastic force density

$$\boldsymbol{f}_e = \nabla \cdot \underline{\boldsymbol{\sigma}}_e = (2\mu_{\text{E}} + \lambda_{\text{E}})\left(q''(r) + \frac{q'(r)}{r} - \frac{q}{r^2}\right)\hat{r}. \tag{3.89}$$

From this and Equation (3.61), we can immediately see the that force applied to the fluid will be radially symmetric, and thus the incompressibility condition will result in zero flow of the fluid ($\boldsymbol{u}_f = 0$). This reduces the equations of motion to a single equation for the evolution of the network

$$\nabla \cdot \underline{\boldsymbol{\sigma}}_e - \xi \boldsymbol{u}_{\text{net}} = 0. \tag{3.90}$$

Rearranging this equation, utilizing Equation (3.89), and noting that $\boldsymbol{u}_{\text{net}} \approx \partial \boldsymbol{q}/\partial t$ (in the small strain limit), we arrive at an evolution equation for the radial component of displacement

$$\frac{\partial q}{\partial t} = \frac{(2\mu_{\text{E}} + \lambda_{\text{E}})}{\xi} \left(\frac{\partial^2 q}{\partial r^2} + \frac{1}{r}\frac{\partial q}{\partial r} - \frac{q}{r^2} \right). \tag{3.91}$$

In this validating experiment, we will not be applying any external loading to the elastic network. This produces a zero-stress boundary condition of the form

$$\underline{\boldsymbol{\sigma}} \cdot \hat{r}\big|_{r=R} = 0, \tag{3.92}$$

which may be expressed as

$$2\mu_{\text{E}} \frac{\partial q}{\partial r} + \lambda_{\text{E}} \left(\frac{\partial q}{\partial r} + \frac{q}{r} \right)\bigg|_{r=R} = 0. \tag{3.93}$$

Finally, we use the initial condition $q(r, 0) = 0.2r$. This corresponds to expanding the circle by 20% initially, and then allowing it to relax freely. This initial condition was chosen to stretch the limits of the small strain assumption and test our methodology.

To validate our IB implementation of poro-elasticity, we would ideally like to compare to a known solution of Equations (3.91) & (3.93). However, we do not have an analytic solution to this problem. Fortunately, Equations (3.91) & (3.93) represent a one-dimensional diffusion-like equation with Robin boundary conditions. This problem may readily be simulated by simple finite difference schemes. Furthermore, these finite difference simulations may be carried out with very high resolution in a single spacial dimension. We simulate these equations on a one-dimensional cell centered grid using standard second-order finite difference stencils. We also use a backward Euler discretization in time. The parameters used are shown in Table 3.1. All values are in numerical units. The resulting displacement $q(r, t)$ is illustrated in Figure 3.4.

We now compare the behavior of our full IB simulation to the predictions of the finite difference simulation. IB simulations are run using the same parameters listed in Table 3.1. We take a circle of immersed elastic network similar to that shown in Figure 3.1, expand it by 20%, and allow it to relax. The only difference between our IB simulations and the finite difference simulation is the spatial and temporal resolution. Due to the increased computational cost of the IB simulations, we run them at signficantly lower resolutions. Simulations were run on Eulerian grid resolutions of size $M_x = M_y$ and M_y equal to

Table 3.1: Parameters for relaxing circle simulation.

Parameter	Numerical Value	Description
R	0.3	Radius of Circle
μ_{E}	0.05	Shear Modulus
λ_{E}	0.05	Lame Constant
ξ	1	Drag Coefficient
μ	1	Fluid Viscosity
γ	0.2	Initial Radial Displacement
N	600	Size of Finite Difference Mesh
dt	10^{-4}	Size of Time Step

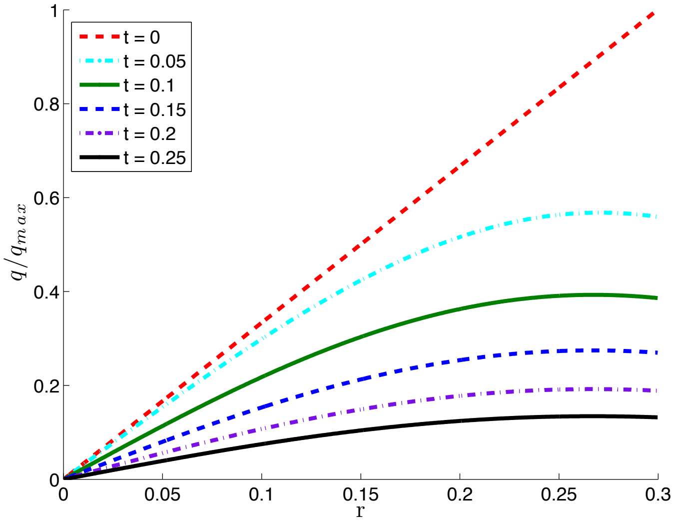

Figure 3.4: Evolution of the displacement $q(r,t)$. Values are reported in units of $q_{max} = \gamma R = 0.06$.

32, 64, and 128. The Lagrangian triangulation was chosen so that the average side length of each triangle was roughly equal to the Eulerian grid spacing. This resulted in Lagrangian meshes of M_{net} equal to 203, 801, and 3266 nodes respectively. For illustration, Figure 3.5 shows several snapshots (which correspond to the time points shown in Figure 3.4) of the outer radius of the elastic network relaxing back to its original radius of 0.3 (these were produced using the most refined mesh in our experiments).

At each time point of our IB simulation, we calculate the radial coordinate of each point in the Lagrangian mesh. This allows us to compute the radial displacement from rest configuration, which we will denote q_{IB}. At time $t = 0.1$, we compare the displacement computed using the IB simulation to that computed using the finite difference scheme on the radially symmetric problem. Our measure of relative

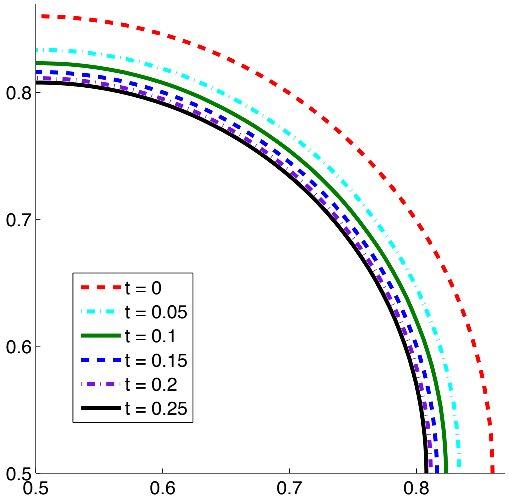

Figure 3.5: Time sequence of the outer radius of a circular elastic network with reference radius $R = 0.3$. The material was expanded by an amount $\gamma = 0.2$ and allowed to relax back towards reference configuration. The time points shown correspond to those illustrated in Figure 3.4.

error is

$$e_{IB}(r) = \frac{q(r, 0.1) - q_{IB}(r, 0.1)}{q_{max}}. \tag{3.94}$$

Figure 3.6 shows the $\mathbb{L}^2$ and $\mathbb{L}^\infty$ norms of the error e_{IB}. It is clear that as the grid is refined, the IB simulation converges to the solution predicted by the finite difference simulation at approximately first order. Thus, we see that our IB model does reproduce the behavior of a porous, linearly elastic material immersed in a viscous fluid.

3.4 Adhesion Model

As we previously mentioned, one of the major motivations for developing a more complex computation framework is to mechanically represent the transmission of stresses to the substrate during locomotion of *physarum*, and to explore how these may affect motility. Therefore we incorporate a model of cell-substrate adhesion into our existing poro-elastic description of the cell cytoplasm.

We begin by defining a new Lagrangian structure, which we refer to as the adhesive complexes. The adhesion complexes will be parametrized by the same Lagrangian coordinate $\boldsymbol{s}$ with domain Γ. We denote the location of the material complexes at time t by $\boldsymbol{X}_{\text{adh}}(\boldsymbol{s}, t)$ to distinguish them from the location of the elastic network $\boldsymbol{X}_{\text{net}}(\boldsymbol{s}, t)$. We assume that each material point of the adhesive complexes interacts with the corresponding material point of the cytoskeleton via a Hookean elastic law. The force density of this

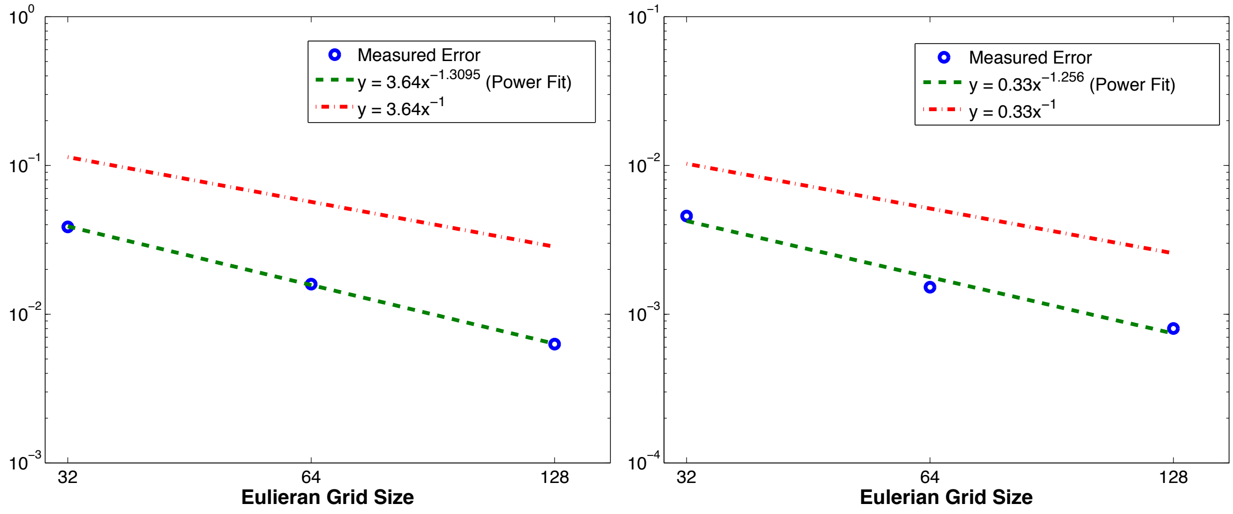

(a) $\|er_{IB}\|_{\mathbb{L}^\infty}$

(b) $\|er_{IB}\|_{\mathbb{L}^2}$

Figure 3.6: Relative error $e_{IB} = (q - q_{IB})/q_{max}$ for three IB simulations. Blue circles indicate the actual measured error. Green dashed lines indicate a power law fit to the measured error and red dashed lines show first order convergence for comparison. The resolution of Eulerian grids shown correspond to immersed networks of 203, 801, and 3266 nodes.

interaction is given by

$$\boldsymbol{F}_{\text{adh}} = k_{\text{adh}} \left(\boldsymbol{X}_{\text{adh}} - \boldsymbol{X}_{\text{net}}\right). \tag{3.95}$$

Similarly, the adhesive complexes experience a force density due to interaction with the substrate that the system is migrating across. As previously stated, we choose to model the adhesive complex/substrate interaction via *modulated* viscous drag. The form of this interaction is given by

$$\boldsymbol{F}_{\text{subs}} = \zeta(\boldsymbol{s},t)\left(\boldsymbol{U}_{\text{subs}} - \frac{\partial \boldsymbol{X}_{\text{adh}}}{\partial t}\right) = \zeta(\boldsymbol{s},t)\left(\boldsymbol{U}_{\text{subs}} - \boldsymbol{U}_{\text{adh}}\right). \tag{3.96}$$

Here, the drag parameter ζ will be referred to as the adhesion coefficient. The functional form of ζ will be discussed in more detail in Chapter 4

The new variable $\boldsymbol{U}_{\text{subs}}$ is the velocity of the substrate that is assumed to be spatially constant. It might seem natural to define all velocities in the “lab” frame, and thus impose that $\boldsymbol{U}_{\text{subs}} = 0$. However, there is no technical need to do so, and in the next section, we will see that $\boldsymbol{U}_{\text{subs}}$ plays an important role in simulation.

With Equations (3.95) & (3.96), we can formulate a new, augmented set of equations that describe the dynamics of our model. Obviously, the force density that the adhesion complexes exert on the cytoskeleton must be equal and opposite to the force density that the cytoskelton exerts on the adhesive complexes.

Finally, all forces on the adhesive complexes must balance. Therefore Equations (3.66)–(3.68) are altered to include the adhesive force density:

$$\Delta \boldsymbol{u}_f - \nabla p - \boldsymbol{f}_{\text{drag}} = 0, \tag{3.97}$$

$$\nabla \cdot \boldsymbol{u}_f = 0, \tag{3.98}$$

$$\boldsymbol{F}_e + \boldsymbol{F}_{\text{drag}} + \boldsymbol{F}_{\text{adh}} = 0, \tag{3.99}$$

$$\boldsymbol{F}_{\text{subs}} - \boldsymbol{F}_{\text{adh}} = 0. \tag{3.100}$$

We may rearrange these equations to give the equations of motion for the two Lagrangian structures. The equation of motion for the network now becomes

$$\frac{d\boldsymbol{X}_{\text{net}}}{dt} = \boldsymbol{U}_{\text{net}} = \frac{1}{\xi}\left(\boldsymbol{F}_e + \boldsymbol{F}_{\text{adh}}\right) + \mathcal{S}^*_{\text{net}} \boldsymbol{u}_f. \tag{3.101}$$

Meanwhile, the equation of motion for the adhesive points is given by

$$\frac{\partial \boldsymbol{X}_{\text{adh}}}{\partial t} = \boldsymbol{U}_{\text{adh}} = \boldsymbol{U}_{\text{subs}} - \frac{\boldsymbol{F}_{\text{adh}}}{\zeta(\boldsymbol{s}, t)}. \tag{3.102}$$

3.4.1 Determining the Substrate Velocity

We now address the issue of determining the unknown velocity $\boldsymbol{U}_{\text{subs}}$. Elastically tethering IB structures to secondary structures that do not directly interact with the fluid (as we have done in our adhesion model) is a technique that has been used in an array of immersed boundary applications [Ter08, Fau92]. However, in the non-inertial regime, this presents complications. When solving Equation (3.97) in a periodic domain, we are subject to the mathematical constrain that the forces applied to the fluid must sum to zero. That is,

$$\int_{\Omega} \boldsymbol{f}_{\text{drag}} \, d\boldsymbol{x} = 0, \tag{3.103}$$

in order for the equation to be solvable. There is no *a priori* reason to believe that the forces introduced by the adhesion model will satisfy this constraint. Furthermore, the average fluid velocity in the domain is determined only up to a constant. For any given $\boldsymbol{f}_{\text{drag}}$, if $\boldsymbol{u}^*(\boldsymbol{x})$ solves Equation (3.97), then so does $\boldsymbol{u}^*(\boldsymbol{x}) + \boldsymbol{u}^C$. In [Ter09], the authors developed a method to exploit this undetermined velocity, in order to ensure that forces remain in balance and that the fluid equation remains solvable. However, in [Ter09], the motion of the secondary Lagrangian structure (called the tether points) was known *a priori*. That is not the case in this work, as our adhesive complexes evolve according to their own force balance law. Nevertheless, we adapt the method of [Ter09] to enforce the solveability condition Equation (3.103) and to simultaneously determine $\boldsymbol{U}_{\text{subs}}$.

We begin by assuming that $\boldsymbol{u}^*$ solves

$$\Delta \boldsymbol{u}^* - \nabla p - \boldsymbol{f}_{\text{drag}} = 0. \tag{3.104}$$

As we have previously stated, this implies that $\boldsymbol{f}_{\text{drag}}$ satisfies the solveability condition, and therefore

$$\begin{aligned} 0 &= \int\limits_{\Omega} \boldsymbol{f}_{\text{drag}}\, d\boldsymbol{x} \\ &= \int\limits_{\Omega} \mathcal{S}_{\text{net}} \boldsymbol{F}_{\text{drag}}\, d\boldsymbol{X} \\ &= \int\limits_{\Gamma_{\text{net}}} \boldsymbol{F}_{\text{drag}}\, d\boldsymbol{s}. \end{aligned} \tag{3.105}$$

Using Equation (3.99), we may substitute and find that

$$0 = -\int\limits_{\Gamma_{\text{net}}} \boldsymbol{F}_e\, d\boldsymbol{s} - \int\limits_{\Gamma_{\text{net}}} \boldsymbol{F}_{\text{adh}}\, d\boldsymbol{s}. \tag{3.106}$$

Because $\boldsymbol{F}_e$ is derived as a variation of an energy function, it integrates to zero. This implies that $\boldsymbol{F}_{\text{adh}}$ must integrate to zero as well, which is the relationship we will attempt to enforce:

$$\int\limits_{\Gamma_{\text{net}}} \boldsymbol{F}_{\text{adh}}\, d\boldsymbol{s} = 0. \tag{3.107}$$

We now assume that this constraint is satisfied initially. In order for the fluid equation to remain solveable, we must have that

$$\frac{d}{dt} \int\limits_{\Gamma_{\text{net}}} \boldsymbol{F}_{\text{adh}}\, d\boldsymbol{s} = 0. \tag{3.108}$$

Expanding $\boldsymbol{F}_{\text{adh}}$ and rearranging terms we have

$$\begin{aligned} 0 =& \frac{d}{dt} \int\limits_{\Gamma_{\text{net}}} \boldsymbol{F}_{\text{adh}}\, d\boldsymbol{s} \\ &= \int\limits_{\Gamma_{\text{net}}} \frac{d}{dt} k_{\text{adh}} \left(\boldsymbol{X}_{\text{adh}} - \boldsymbol{X}_{\text{net}} \right) d\boldsymbol{s} \\ &= \int\limits_{\Gamma_{\text{net}}} k_{\text{adh}} \left(\frac{d\boldsymbol{X}_{\text{adh}}}{dt} - \frac{d\boldsymbol{X}_{\text{net}}}{dt} \right) d\boldsymbol{s}. \end{aligned} \tag{3.109}$$

We may now use the evolution equations of the adhesive points and the network (Equations (3.101) &

(3.102)) to write

$$0 = \int\limits_{\Gamma_{\text{net}}} k_{\text{adh}} \left(\boldsymbol{U}_{\text{subs}} - \frac{\boldsymbol{F}_{\text{adh}}}{\zeta(\boldsymbol{s},t)} - \frac{1}{\xi}\left(\boldsymbol{F}_e + \boldsymbol{F}_{\text{adh}}\right) - \mathcal{S}^*\boldsymbol{u}^* \right) d\boldsymbol{s}. \tag{3.110}$$

Rearranging terms and realizing that $\boldsymbol{U}_{\text{subs}}$ is a constant that may be pulled from the integral, we have

$$\boldsymbol{U}_{\text{subs}} = \frac{1}{\int_{\Gamma_{\text{net}}} k_{\text{adh}}\, d\boldsymbol{s}} \int\limits_{\Gamma_{\text{net}}} \left(\left(\frac{k_{\text{adh}}}{\xi} + \frac{k_{\text{adh}}}{\zeta(\boldsymbol{s},t)} \right) \boldsymbol{F}_{\text{adh}} + \frac{k_{\text{adh}}}{\xi}\boldsymbol{F}_e + \mathcal{S}^*\boldsymbol{u}^* \right) d\boldsymbol{s}. \tag{3.111}$$

This expression uniquely determines the substrate velocity $\boldsymbol{U}_{\text{subs}}$, which ensures that all forces within the system *remain* in balance as the system evolves and that the solveability constraint is maintained.

Finally we note that not only is the fluid equation unchanged when the fluid velocity is altered by a constant, but none of the forces within the model change under this transformation either. More precisely, if $\boldsymbol{u}_f$, $\boldsymbol{U}_{\text{net}}$, $\boldsymbol{U}_{\text{adh}}$, and $\boldsymbol{U}_{\text{subs}}$ satisfy the force balance (Equations (3.97)–(3.100)), then so do $\boldsymbol{u}_f + \boldsymbol{u}^C$, $\boldsymbol{U}_{\text{net}} + \boldsymbol{u}^C$, $\boldsymbol{U}_{\text{adh}} + \boldsymbol{u}^C$, and $\boldsymbol{U}_{\text{subs}} + \boldsymbol{u}^C$. We will exploit this and set $\boldsymbol{u}^C = -\boldsymbol{U}_{\text{subs}}$, where $\boldsymbol{U}_{\text{subs}}$ is calculated via Equation (3.111). In addition to ensuring that all forces remain in balance, this will have the added benefit of keeping the "lab frame" fixed throughout a simulation. This is beneficial when attempting to analyze results, as no further changes of frame are necessary.

During simulation, the method follows a relatively simple time stepping algorithm similar to that outlined in Section 3.3.3. However, the integral in Equation (3.111) is replaced with a discrete sum over Lagrangian nodes. The method proceeds as follows:

1. Given the configurations $\boldsymbol{X}_{\text{net}}$ of the network and $\boldsymbol{X}_{\text{adh}}$ of the adhesive complexes, evaluate the elastic force $\boldsymbol{F}_e$ via Equation (3.80) and the adhesive force $\boldsymbol{F}_{\text{adh}}$ via Equation (3.95).
2. Given the elastic and adhesive force on the network, solve for the force due to drag via Equation (3.99).
3. Given the force due to drag $\boldsymbol{F}_{\text{drag}}$, spread it to the Eulerian grid: $\boldsymbol{f}_{\text{drag}} = \mathcal{S}_{\text{net}}\boldsymbol{F}_{\text{drag}}$.
4. Given the force due to drag on the fluid, solve the Stokes problem for the intermediate fluid velocity ($\boldsymbol{u}^*$) via Equation (3.97).
5. Interpolate the intermediate fluid velocity back to the Lagrangian grid ($\mathcal{S}^*\boldsymbol{u}^*$).
6. Evaluate the substrate velocity $\boldsymbol{U}_{\text{subs}}$ via Equation (3.111).

7. Evaluate the *intermediate* network velocity $\boldsymbol{U}^*_{\text{net}}$ via Equation (3.101), and the intermediate adhesion velocity $\boldsymbol{U}^*_{\text{adh}}$ via Equation (3.102).

8. Evaluate the true velocities by setting $\boldsymbol{u}_f = \boldsymbol{u}^* - \boldsymbol{U}_{\text{subs}}$, $\boldsymbol{U}_{\text{net}} = \boldsymbol{U}^*_{\text{net}} - \boldsymbol{U}_{\text{subs}}$, $\boldsymbol{U}_{\text{adh}} = \boldsymbol{U}^*_{\text{adh}} - \boldsymbol{U}_{\text{subs}}$.

9. Evolve the network configuration via the forward Euler scheme $\boldsymbol{X}_{\text{net}}(t + \Delta t) = \boldsymbol{X}_{\text{net}}(t) + \Delta t \boldsymbol{U}_{\text{net}}$. Similarly evolve the adhesive points according to $\boldsymbol{X}_{\text{adh}}(t + \Delta t) = \boldsymbol{X}_{\text{adh}}(t) + \Delta t \boldsymbol{U}_{\text{adh}}$.

We will not discuss the spatial discretization of the adhesion model until Section 3.5.2.

3.5 Membrane & Cortex Model

We now develop the final component of our model of a crawling cell: the enclosing membrane. The following discussion of the membrane dynamics is relatively standard in the Immersed Boundary literature [Pes02]. It is included here for completeness.

Recall that the membrane is parametrized by its own Lagrangian coordinate θ with domain Γ_{mem}, and its spacial position is given by $\boldsymbol{X}_{\text{mem}}(\theta, t)$. This configuration determines the elastic potential energy of the membrane

$$E_{\text{mem}} = \int\limits_{\Gamma_{\text{mem}}} W_{\text{mem}} d\theta, \tag{3.112}$$

where $W_{\text{mem}}(\boldsymbol{X}_{\text{mem}})$ is the elastic energy density. The elastic force density on the membrane is calculated as the variational derivative of the potential energy

$$\boldsymbol{F}_{\text{mem},e} = -\frac{\mathfrak{d} E_{\text{mem}}}{\mathfrak{d} \boldsymbol{X}_{\text{mem}}}. \tag{3.113}$$

We note that since the membrane is a one-dimensional structure, the term "force density" should be understood to imply *force per unit length* in this context. The elastic energy density is assumed to be a function of the local strain of the membrane and to penalize deviations from a given reference configuration $\boldsymbol{X}_0(\theta)$. This can be formulated as

$$W_{\text{mem}} = W_{\text{mem}}\left(\left|\frac{\partial \boldsymbol{X}_{\text{mem}}}{\partial \theta}\right|\right) = \frac{k_{\text{mem}}}{2}\left(\frac{\left|\frac{\partial \boldsymbol{X}_{\text{mem}}}{\partial \theta}\right| - \left|\frac{\partial \boldsymbol{X}_0}{\partial \theta}\right|}{\left|\frac{\partial \boldsymbol{X}_0}{\partial \theta}\right|}\right)^2. \tag{3.114}$$

Carrying out the variational derivative, we see that the force density is given by

$$\boldsymbol{F}_{\text{mem},e} = \frac{\partial}{\partial \theta}\left(k_{\text{mem}} \frac{\left|\frac{\partial \boldsymbol{X}_{\text{mem}}}{\partial \theta}\right| - \left|\frac{\partial \boldsymbol{X}_0}{\partial \theta}\right|}{\left|\frac{\partial \boldsymbol{X}_0}{\partial \theta}\right|} \frac{\frac{\partial \boldsymbol{X}_{\text{mem}}}{\partial \theta}}{\left|\frac{\partial \boldsymbol{X}_{\text{mem}}}{\partial \theta}\right|}\right). \tag{3.115}$$

This expression can be simplified greatly if we identify the tension within the membrane as

$$T = k_{\text{mem}} \frac{\left| \frac{\partial \boldsymbol{X}_{\text{mem}}}{\partial \theta} \right| - \left| \frac{\partial \boldsymbol{X}_0}{\partial \theta} \right|}{\left| \frac{\partial \boldsymbol{X}_0}{\partial \theta} \right|}, \tag{3.116}$$

and note that

$$\hat{\tau} = \frac{\frac{\partial \boldsymbol{X}_{\text{mem}}}{\partial \theta}}{\left| \frac{\partial \boldsymbol{X}_{\text{mem}}}{\partial \theta} \right|}, \tag{3.117}$$

where $\hat{\tau}$ is the unit tangent to the membrane. In this case, Equation (3.115) can be interpreted as

$$\boldsymbol{F}_{\text{mem},e} = \frac{\partial}{\partial \theta} \left(T \hat{\tau} \right). \tag{3.118}$$

This model also allows us to represent a membrane under tension (at rest) by the addition of a single term. In Chapter 4, we will model a cell membrane under resting tension. Therefore, we alter Equation (3.116) to

$$T = k_{\text{mem}} \frac{\left| \frac{\partial \boldsymbol{X}_{\text{mem}}}{\partial \theta} \right| - \left| \frac{\partial \boldsymbol{X}_0}{\partial \theta} \right|}{\left| \frac{\partial \boldsymbol{X}_0}{\partial \theta} \right|} + \gamma. \tag{3.119}$$

We assume that initially at time $t = 0$, the membrane configuration is equal to the reference configuration

$$\boldsymbol{X}_{\text{mem}}(\theta, 0) = \boldsymbol{X}_0(\theta). \tag{3.120}$$

We further assume that this configuration coincides with the boundary of the elastic cytoskeletal network. Therefore, each material point θ is associated with a material point $\boldsymbol{s}_\theta$ on the boundary of the network and

$$\boldsymbol{X}_{\text{mem}}(\theta, 0) = \boldsymbol{X}_{\text{net}}(\boldsymbol{s}_\theta, 0), \text{ for some } \boldsymbol{s}_\theta = \boldsymbol{s}_\theta(\theta). \tag{3.121}$$

This should not be misconstrued to say that the membrane is defined to be the boundary of the network. Indeed, the membrane will evolve with a velocity field distinct to that of the network, as we shall see.

We assume that the membrane is mechanically linked to the interior network through an elastic force law. The membrane experiences a force density (per unit length) given by

$$\boldsymbol{F}_{\text{mem,attach}} = k_{\text{attach}} \left(\boldsymbol{X}_{\text{net}}(\boldsymbol{s}_\theta, t) - \boldsymbol{X}_{\text{mem}}(\theta, t) \right). \tag{3.122}$$

Consequently, the cytoskeletal network experiences a force per unit length on the *boundary* given by

$$\boldsymbol{F}_{\text{net,attach}} = k_{\text{attach}} \left(\boldsymbol{X}_{\text{mem}}(\theta, t) - \boldsymbol{X}_{\text{net}}(\boldsymbol{s}_\theta, t) \right). \tag{3.123}$$

We may now write the total force density on the membrane due to elastic effects as

$$\boldsymbol{F}_{\text{mem}} = \boldsymbol{F}_{\text{mem},e} + \boldsymbol{F}_{\text{mem,attach}}. \tag{3.124}$$

Finally, we identify the membrane as an impermeable boundary within the fluid domain. At this boundary we assume a no-slip boundary condition. Since the membrane is neutrally buoyant, all forces acting on the membrane are transmitted directly to the fluid. This implies that the membrane does not require its own force balance equation, but rather the force density on the membrane appears as an extra term in the fluid equation. Again, the transmission of these stresses to the fluid is accomplished via a spreading operator, Equation (3.4). The no-slip boundary condition is satisfied by stipulating that the membrane must evolve with the local fluid velocity. This is accomplished via the interpolation operator, Equation (3.5),

$$\frac{\partial \boldsymbol{X}_{\text{mem}}}{\partial t} = \boldsymbol{U}_{\text{mem}} = \mathcal{S}^*_{\text{mem}} \boldsymbol{u}_f. \tag{3.125}$$

3.5.1 Full System of Equations

By combining our poro-elastic model of the cell interior, together with our adhesion model and the membrane that bounds the cell interior, we arrive at our full IB model of a crawling cell. The force density balances that define the system are

$$\Delta \boldsymbol{u}_f - \nabla p - \boldsymbol{f}_{\text{drag}} + \boldsymbol{f}_{\text{mem}} = 0, \tag{3.126}$$

$$\nabla \cdot \boldsymbol{u}_f = 0, \tag{3.127}$$

$$\boldsymbol{F}_e + \boldsymbol{F}_{\text{drag}} + \boldsymbol{F}_{\text{adh}} + [\boldsymbol{F}_{\text{net,attach}}] = 0, \tag{3.128}$$

$$\boldsymbol{F}_{\text{subs}} - \boldsymbol{F}_{\text{adh}} = 0. \tag{3.129}$$

Here, $[\boldsymbol{F}_{\text{net,attach}}]$ is a delta-like distribution of forces on the *boundary* of the network due to $\boldsymbol{F}_{\text{net,attach}}$. The equations of motion for the Lagrangian structures are

$$\frac{\partial \boldsymbol{X}_{\text{mem}}}{\partial t} = \mathcal{S}^*_{\text{mem}} \boldsymbol{u}_f, \tag{3.130}$$

$$\frac{\partial \boldsymbol{X}_{\text{net}}}{\partial t} = \mathcal{S}^* \boldsymbol{u}_f + \frac{1}{\xi}\left(\boldsymbol{F}_e + \boldsymbol{F}_{\text{adh}} + [\boldsymbol{F}_{\text{net,attach}}]\right), \tag{3.131}$$

$$\frac{\partial \boldsymbol{X}_{\text{adh}}}{\partial t} = \boldsymbol{U}_{\text{subs}} - \frac{\boldsymbol{F}_{\text{adh}}}{\zeta(\boldsymbol{s},t)}. \tag{3.132}$$

3.5.2 Discretization

We discretize the full model in the following way. The poro-elastic cell interior is triangulated via the method described in Section 3.3.3. After discretization, the adhesive points are assumed to be equal (initially) to the corresponding network nodes, and we set $\boldsymbol{X}^i_{\text{adh}} = \boldsymbol{X}^i_{\text{net}}$. Lagrangian points on the *boundary* are identified and ordered geometrically to assign a membrane Lagrangian coordinate θ^j. We then construct the mapping $\theta^j \rightarrow \boldsymbol{s}^i$ and set $\boldsymbol{X}^j_{\text{mem}} = \boldsymbol{X}^i_{\text{net}}$ for the appropriate points. This yields the initial position of the membrane $\boldsymbol{X}_0(\theta^j) = \boldsymbol{X}^j_0$.

Having this discrete parametrization allows us to approximate the derivatives in Equation (3.115) via finite differences. We define the quantities

$$\Delta\theta^{j+} = \left|\boldsymbol{X}^{j+1}_0 - \boldsymbol{X}^j_0\right|, \tag{3.133}$$

$$\Delta\theta^{j-} = \left|\boldsymbol{X}^{j}_0 - \boldsymbol{X}^{j-1}_0\right|, \tag{3.134}$$

$$\Delta\theta^{j} = \frac{1}{2}\left(\Delta\theta^{j+} + \Delta\theta^{j-}\right). \tag{3.135}$$

Note that these difference quantities are calculated using the *reference* membrane configuration. We also define the one-dimensional volume of each point θ^j to be $d\ell^j = \Delta\theta^j$. Note that this quantity is indexed by a single integer and should not be confused with the reference length of the springs in our poro-elastic network defined in Equation (3.76) This is necessary for the discrete spread and interpolation operators from the membrane (Equations (3.27) & (3.28)).

We now may calculate approximate derivatives ($\partial \boldsymbol{X}_{\text{mem}}/\partial\theta$) via forward and backward finite difference schemes

$$\Delta\boldsymbol{X}^{j+}_{\text{mem}} = \frac{\boldsymbol{X}^{j+1}_{\text{mem}} - \boldsymbol{X}^{j}_{\text{mem}}}{\Delta\theta^{j+}}, \tag{3.136}$$

$$\Delta\boldsymbol{X}^{j-}_{\text{mem}} = \frac{\boldsymbol{X}^{j}_{\text{mem}} - \boldsymbol{X}^{j-2}_{\text{mem}}}{\Delta\theta^{j-}}. \tag{3.137}$$

Derivatives of the reference configuration ($\Delta\boldsymbol{X}^{j+}_0$ and $\Delta\boldsymbol{X}^{j-}_0$) may be calculated in a completely analogous manner. Using our finite differences, we can approximate the tangent vector to the membrane, as well as the tension in the membrane via discrete analogues of Equations (3.116) & (3.117):

$$\hat{\tau}^{j+} = \frac{\Delta \boldsymbol{X}^{j+}_{\text{mem}}}{\left|\Delta \boldsymbol{X}^{j+}_{\text{mem}}\right|}, \tag{3.138}$$

$$\hat{\tau}^{j-} = \frac{\Delta \boldsymbol{X}^{j-}_{\text{mem}}}{\left|\Delta \boldsymbol{X}^{j-}_{\text{mem}}\right|}, \tag{3.139}$$

$$T^{j+} = k_{\text{mem}} \frac{\left|\Delta \boldsymbol{X}^{j+}_{\text{mem}}\right| - \left|\Delta \boldsymbol{X}^{j+}_{0}\right|}{\left|\Delta \boldsymbol{X}^{j+}_{0}\right|}, \tag{3.140}$$

$$T^{j-} = k_{\text{mem}} \frac{\left|\Delta \boldsymbol{X}^{j-}_{\text{mem}}\right| - \left|\Delta \boldsymbol{X}^{j-}_{0}\right|}{\left|\Delta \boldsymbol{X}^{j-}_{0}\right|}. \tag{3.141}$$

Finally, we are able to define the discrete elastic energy at a membrane node via the centered finite difference

$$\boldsymbol{F}^{j}_{\text{mem},e} = \frac{T^{j+}\hat{\tau}^{j+} - T^{j-}\hat{\tau}^{j-}}{\Delta \theta^{j}}. \tag{3.142}$$

We now address the attachment force that links the membrane to the cytoskeletal network. As previously mentioned, these attachments result in a *boundary* force on the network, which given our dimensional reduction, has units of force per *length*. Mathematically, this results in a jump boundary condition on the force balance equation for the network. However, we wish to avoid boundary conditions, and integrate this effect directly into the force balance (Equation (3.67)), resulting in Equation (3.128). This can be done by approximating the boundary force with a force density supported only at the boundary nodes of the cytoskeletal network. However, some care must be taken to maintain proper scaling of forces. We begin by defining the attachment *force*, which acts between the membrane and cortex

$$\widehat{\boldsymbol{F}^{j}}_{\text{mem,attach}} = k_{\text{attach}} \left(\boldsymbol{X}^{i}_{\text{net}} - \boldsymbol{X}^{j}_{\text{mem}}\right), \tag{3.143}$$

$$\widehat{\boldsymbol{F}^{i}}_{\text{net,attach}} = k_{\text{attach}} \left(\boldsymbol{X}^{j}_{\text{mem}} - \boldsymbol{X}^{i}_{\text{net}}\right), \tag{3.144}$$

where it is understood that the membrane Lagrangian point θ^{j} maps to the network Lagrangian node $\boldsymbol{s}^{i}$. We then define the force densities as

$$\boldsymbol{F}^{j}_{\text{mem,attach}} = \frac{\widehat{\boldsymbol{F}^{j}}_{\text{mem,attach}}}{\Delta \theta^{j}}, \tag{3.145}$$

$$\boldsymbol{F}^{i}_{\text{net,attach}} = \frac{\widehat{\boldsymbol{F}^{i}}_{\text{net,attach}}}{\Delta A^{i}}. \tag{3.146}$$

This scaling ensures that forces remain in balance as the discrete Lagrangian structures are refined. It also ensures that when the contribution from these two force densities are spread to the fluid (from the membrane and network respectively), they balance and do not violate the solveability constraint of the fluid equation. More precisely, this enforces

$$\int_{\Omega} \left(\mathcal{S}_{\text{net}}\boldsymbol{F}_{\text{net,attach}} + \mathcal{S}_{\text{mem}}\boldsymbol{F}_{\text{mem,attach}}\right) \, d\boldsymbol{x} = 0, \tag{3.147}$$

which discretely has the form

$$\sum_{n=1,m=1}^{M_x,M_y} \left(\sum_{i=1}^{M_{\text{net}}} \boldsymbol{F}_{\text{net,attach}} \delta_2 \left(\boldsymbol{X}_{\text{net}}^{i} - x^{nm}\right) dA^i \right. \\ \left. + \sum_{j=1}^{M_{\text{mem}}} \boldsymbol{F}^{j}_{\text{mem,attach}} \delta_2 \left(\boldsymbol{X}^{j}_{\text{mem}} - x^{nm}\right) d\ell^j \right) \Delta x \Delta y = 0. \tag{3.148}$$

The scaling defined above ensures that this equality holds discretely for all levels of refinement.

3.6 Discussion

We now have a fully developed modeling framework with which to describe a crawling *physarum* plasmodium. This framework incorporates a poro-elastic cell interior, with a solid elastic cytoskeleton permeated with Newtonian fluid. It also incorporates adhesive interactions to the substrate that are mechanically linked to the cells internal structure, as well as an elastic membrane/cortex bounding the cell exterior. This entire model has been embeded into an Immersed Boundary framework for ease of simulation. In the following chapter, we will use this model to address the crawling of *physarum* observed in [Mat08]. Specifically, we will address questions about how the observed flow of fluid may drive locomotion, and how the stresses associated with this flow are transmitted to the substrate.

Chapter 4

Simulating Crawling *Physarum*

4.1 Introduction

In this chapter we investigate the coordination of cytoskeletal contraction, substrate adhesion and cytoplasmic flow in migrating amoebae of the slime mold *Physarum polycephalum*. As discussed in Chapter 2, a purely hydrodynamic explanation of motile *physarum* plasmodia ignores the transmission of stresses to the underlying substrate, which are necessary for cellular migration to take place. It is unclear if passive, uncoordinated cell-substrate interactions are sufficient for *physarum* plasmodia to effectively “flow” across a substrate. Alternately, the motility of *physarum* plasmodium may be dependent upon cell-substrate adhesion which is dynamically coordinated relative to the stresses generated by the flow. It is known that substrate bound structures within the cell are mechanically linked the to actomysosin network within the plasmodium [Bri87]. However, the precise nature of these structures is not well studied, and there currently exists no quantitative description of the stresses which the cell exerts on the substrate as it migrates, nor how these stresses are correlated to the cytoplasmic flow measured in [Mat08].

To address these questions we use the model devloped in Chapter 3 to examine how cytoskeletal contraction, cyotosolic flow, and cell-substrate adhesion work together to generate cell locomotion. We also compare the model predictions to Particle Image Velocimetry (PIV) and Traction Force Microscopy (TFM) experiments performed on migrating *physarum* plasmodia by our collaborators Dr. Juan Carlos del Álamo and Shun Zhang. TFM is an experimental method specifically designed to measure the stresses migrating cells exert on the underlying substrate. TFM has been used to study the spatiotemporal patterns of cell-substrate interactions in a diverse array of unicellular and multicellular organisms ranging from a few microns to a few centimeters in size [Dem99, But02, Rie05, DA07, Lai10]. In particular, TFM has been applied to multiple migrating cell types including fibroblasts, neutrophils, and *dictyostelium*.

Our collaborators' measurements show that traction stresses in migrating *physarum* amoebae are mainly distributed along the cell periphery forming an inward contractile pattern. These stresses are spatiotemporally modulated to establish a rythmic contraction wave that travels in the direction of cell migration (see Figures 4.3, 4.5 and 4.10). The contractile wave has the same time period as the intracellular flow waves previously described, and a phase lag of approximately 1/3 of a cycle. By measuring the spatiotemporal patterns of both flow waves and stresses applied to the substrate, we are able to quantify the correlation between the flows previously reported and the stresses that drive the cell across the substrate. We see that the pattern of stress on the substrate is time periodic, with a well defined timing relative to rhythmic streaming of cytoplasm.

Within our modeling framework, we propose an idealized phenomenological mode of adhesion strength, also consisting of a traveling wave. We then compare numerical simulation of our model developed in Chapter 3 to flows and tractions stresses observed *in vivo*. These spatiotemporal flow and stress patterns are reproduced by the numerical simulations using the model. Using the numerical model, we investigate a range of parameters which characterize the strength of adhesion and the coordination of adhesion *relative* to the rhythmic flow of cytoplasm. Specific coordination patterns are identified which are consistent with experimental data. These parameters are seen to be optimal in that they (nearly) maximize migration velocity of the model cell for a given strength of actomyosin contraction. Finally, we perform numerical simulations of the model cell crawling across randomly heterogeneous substrates and show that the speed of migration is only mildly perturbed. These simulations imply that the proposed model of motility is robust to perturbations of adhesiveness of the extracellular substrate.

4.2 Model Parameters and Inputs

4.2.1 Cell Geometry and Discretization

We first define a cell geometry inspired by the plasmodia observed in [Mat08] and our collaborators' experiments. The model cell is composed of long rectangular region with semicircular "caps" at either end. The width of the model cell (and diameter of the semicircular caps) is denoted L_y. To be consistent with experiments we set $L_y = 66.6$ µm. The overall length of the cell (L_x) is 400 µm. This gives the cell an aspect ratio of $6 : 1$. The cell interior is discretized with $M_{\text{net}} = 706$ Lagrangian network nodes. This results in a triagulation of 1270 faces with an average area of 24.1 µm^2 and an average side length of

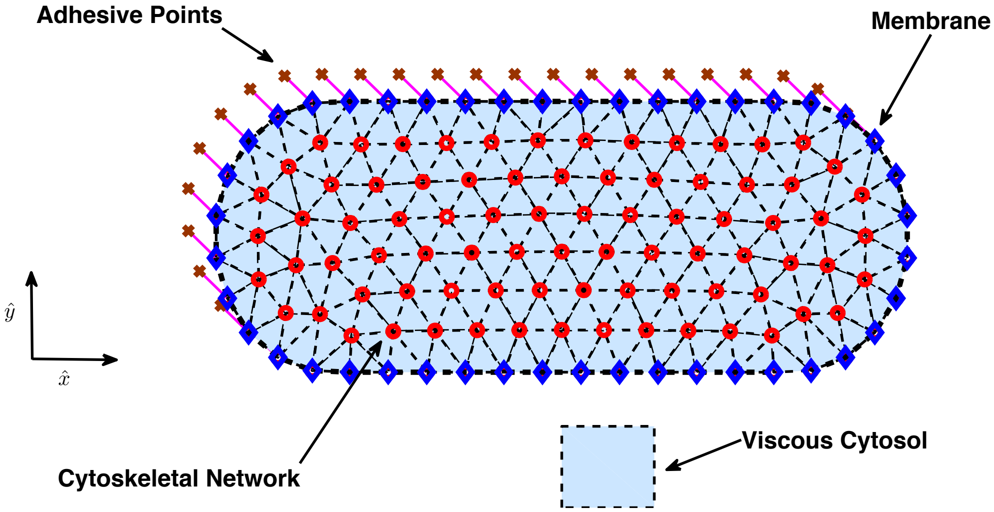

Figure 4.1: A schematic of our full computation model of a *physarum* plasmodium. Cytoskeletal network points are shown in red. Membrane points are shown in deep blue. Adhesive points are illustrated in brown. Finally, the viscous cytosol that permeates the porous media is shown in light blue.

7.5 μm. The boundary of the cell contains $M_{\text{mem}} = 140$ points which are used to initialized the discrete membrane. A schematic of numerical cell is shown in Figure 4.1. The adhesive points are moved slightly for illustrative purposed, but are initialized as per the description in Section 3.5.2. The Eulerian domain is a periodic square of length 640 μm. It is discretized with a grid of size $M_x = 64$ by $M_y = 128$. The y-direction was discretized more finely to resolve the fluid velocity field within the relatively narrow cell body.

4.2.2 Model Inputs

We now discuss the inputs of our model that will drive the simulation. The deformations in *physarum* that drive the observed flows are generated by an actin-myosin contraction within the cell interior. This contraction has been linked to a Ca^{2+} oscillation on the cytoplasm [Yos10]. However, we do not include a description of chemical kinetics in our modeling framework. Rather, we add a term due to contractile stress to the force balance equation of the cytoskeleton, and use a phenomenological description of this contractile stress.

We modify Equation (3.128) to include a force due to active cytoskeletal contraction

$$\boldsymbol{F}_a + \boldsymbol{F}_e + \boldsymbol{F}_{\text{drag}} + \boldsymbol{F}_{\text{adh}} + \boldsymbol{F}_{\text{net,attach}} = 0. \tag{4.1}$$

The term $\boldsymbol{F}_a$ is the active contractile force density, and is assumed to be a result of an active stress

$$\boldsymbol{F}_a = \nabla \cdot \underline{\boldsymbol{\sigma}}_a. \tag{4.2}$$

We do not have experimental measurements of the spatio-temporal form of contraction within the cytoskeleton of *physarum*. However, we assume that this contraction is correlated with the observed deformation which has been measured. For this reason, we prescribe the contraction within the network to be a traveling sinusoidal function of the cell body coordinate,

$$\underline{\boldsymbol{\sigma}}_a = \frac{\sigma_{\text{max}}}{2}\left(\cos\left(\frac{2\pi}{\ell_{\text{cont}}}\boldsymbol{s}\cdot\hat{x} - \frac{2\pi}{T}t\right) + 1\right)\mathbb{I}. \tag{4.3}$$

This functional form of $\underline{\boldsymbol{\sigma}}_a$ results in an isotropic contractile stress with maximum magnitude σ_{max} and a minimum magnitude of zero. This is to ensure that the cytoskeleton is never generating an active *expansive* stress.

In order to represent this *force density* due to contractile stress in our simulations, we apply a contractile loading *force* in our discrete cytoskeletal network. After discretization, the network is defined by a triangulation of the cell interior. Upon each edge of this triangulation, we calculate a force on the two discrete points defined by that edge. For each discrete Lagrangian point $\boldsymbol{s}^i$ with an edge connecting it to point $\boldsymbol{s}^j$, the orientation of that edge is defined by the unit vector $\hat{r}^{ij}$. The sinusoidal wave of loading force within the network is again a function of the longitudinal cell coordinate. For each link, the magnitude of the force is defined by the Lagrangian coordinate of the link center. Therefore, we have

$$\widehat{\boldsymbol{F}_a^{ij}} = \frac{C}{2}\left(\cos\left(\frac{2\pi}{\ell_{\text{cont}}}\left(\frac{\boldsymbol{s}^i + \boldsymbol{s}^j}{2}\right)\cdot\hat{x} - \frac{2\pi}{T}t\right) + 1\right)\hat{r}^{ij}, \tag{4.4}$$

This is a traveling sinusoidal wave of maximum amplitude C and minimum amplitude zero, again to avoid any expansive forces. The total force at the point $\boldsymbol{s}^i$ is given by the sum of these forces over all edges emanating from that point

$$\widehat{\boldsymbol{F}_a}(\boldsymbol{s}_i) = \widehat{\boldsymbol{F}_a^i} = \sum_j \widehat{\boldsymbol{F}_a^{ij}}. \tag{4.5}$$

And finally the force density at point $\boldsymbol{s}^i$ is obtained by dividing by discrete area of the point

$$\boldsymbol{F}_a^i = \frac{\widehat{\boldsymbol{F}_a^i}}{dA^i}. \tag{4.6}$$

Thus, we drive our simulations with a propagating wave of contractile force of amplitude C, which travels in the x-direction (from posterior to anterior) with velocity ℓ_{cont}/T. The parameter C is related to the magnitude of isotropic stress by the relation

$$\sigma_{\max} = \frac{3C}{2}\frac{\overline{d\ell}}{\overline{dA}}, \tag{4.7}$$

where $\overline{d\ell}$ is the *average* length of the triangulation edges, and $\overline{dA}$ is the average area of the faces in the triangulation. This relation is arrived at in a similar fashion to Equation (3.83) by comparing the discrete and continuum models of elasticity. For more details see Appendix C.

As discussed in Chapter 3, we must now specify a form of the adhesion coefficient $\zeta(\boldsymbol{s}, t)$ to complete the inputs of the model. As we've previously mentioned, the nature of the of the mechanism with which *physarum* adheres to the substrate is not known, though some candidate integrin-like proteins have been identified [Hay08]. The period of the deformations observed in *physarum* is long ($\sim$ 100 sec) compared to the timescale of the dynamics of a cell-substrate bond, and so we represent the dynamics of adhesion via a viscous drag law [Sri09]. The functional form of this viscous drag is phenomenological. In this chapter we investigate an idealized model of adhesion of the form

$$\zeta(\boldsymbol{s}, t) = \frac{A}{2}\left(\cos\left(\frac{2\pi}{\ell_{\text{adh}}}\boldsymbol{s}\cdot\hat{x} - \frac{2\pi}{T}t + \phi\right) + 1\right) + \epsilon. \tag{4.8}$$

This choice of ζ is inspired by the observation that both the deformation of, and associated flow within *physarum* propagate from the posterior to the anterior as a phase wave. Furthermore, the traction stresses exerted on the substrate by the migrating plasmodium appear to have a phase wave character (discussed in more detail in Section 4.7). Therefore we make the assumption that the strength of adhesive interaction with the substrate is characterized by a phase wave of maximum amplitude $A + \epsilon$ and minimum amplitude ϵ. This is done to prevent simulation of a negative viscous drag coefficient. The amplitude parameter A is a measure of the strength of active coordinated adhesion, and will often be referred to as the "coefficient of adhesion" in the following text. The parameter ϵ represents nonspecific adhesive interactions between the substrate and the basal surface of the cell. We will often report coefficient of adhesion in nondimensional units of $[A/\epsilon]$ in later sections. The wavelength ℓ_{adh} and period T of the adhesion modulation are assumed to be the same as the those of the contractile wave. The parameter ϕ represents the phase of the coordinated adhesion *relative* to the traveling wave of contraction strength (Equation (4.4)). This will be a parameter of interest in later sections, as we will investigate the biological significance of the coordination of contraction, flow, and adhesion.

4.2.3 Model Parameters

We perform simulation of the model using the parameter values listed in Table 4.1. Where possible, parameter values are chosen to be consistent with measured or estimated values in the literature. However, some model parameters are simply not experimentally measurable, or were arrived at through numerical experimentation. Below we give a brief discussion of our estimates for these parameters.

Specifics of Phase Waves The wavelength and period of the cytoskeletal contraction (ℓ_{cont} and T) are not directly measurable, but the wavelength and period of the resulting deformation are relatively straightforward to measure. We assume that the resulting deformation wave of the cell shape is directly correlated with the underlying cytoskeletal contraction. We choose $\ell_{\text{cont}} = 1600$ µm (four body lengths) and $T = 100$ sec, which is consistent with the wavelength and period of deformation reported in [Mat08] and in our collaborators' experiments. As previously mentioned, the wavelength and period of the adhesion wave are assumed to be the same.

Contraction and Adhesion The amplitude of cytoskeletal contraction was chosen to approximately reproduce the magnitude of deformations seen in the experiments of our collaborators (about 25% of cell width). The coefficient of specific adhesion A was chosen to range over values less than to much greater than the coefficient of nonspecific adhesion ϵ. The value of ϵ listed in Table 4.1 was chosen to reproduce traction stresses of approximately the scale observed in the experiments.

Cytoskeletal Drag The ratio of cytosol viscosity and drag coefficient (μ/ξ) is the Darcy permeability of the cytoskeleton (See Section 3.3). The permeability of cytoskeletal network has been estimated in other cell types [Ker09, Cha05]. However, these estimates were based on dense actin networks and result in permeability bounds as low as 10^{-5} µm^2. *Physarum*, conversely, pumps fluid through well formed flow channels with relatively unformed cytoskeletal meshwork. Through a thin gap flow approximation, we estimate a permeability of 33.3 µm^2 in flow channels. In this work, we are representing the rheology of the cell interior as a uniformly network with a single permeability of 3.28 µm^2, derived from homogenizing a flow channel surrounded by a dense actin network. The value of ξ listed in Table 4.1 was calculated from this permeability as discussed in Section 3.3. Details of the homogenization are provided in Section 4.2.4.

Cytoskeletal Elasticity Elastic moduli of living cells have been measured to vary over a vast range (10 Pa – 40 kPa) depending on cell type and experimental setup [Yam00, Bau98, Wan93]. The elastic moduli of the cytoskeleton has not been measured for *physarum* plasmodia on this scale. Therefore, we choose a moderate value of λ_E which falls well within the range of previously reported values. It has been previously observed that the posterior end of the cell comprised of a much more developed actin cytoskeleton, while the anterior end of the cell exhibits much less dense intracellular structure [Sto94]. For this reason, we assume that the front 20% of the model cell has an elastic modulus half as large as the posterior 80%. Similarly, the strength of contraction in this anterior region is half as strong to model the relatively lower capacity for contractile stress generation the less developed cytoskeleton.

Table 4.1: Model parameters for crawling simulation.

Parameter	Numerical Value	Description
L_x	400 µm	Cell Length
L_y	66.6 µm	Cell Width
d	20 µm	Cell Gap Height
μ	0.75 Pa sec	Cytosol Viscosity
ξ	2.29×10^{11} Pa sec/m^2	Drag Coefficient
λ_E	781 Pa	Cytoskeletal Elastic Modulus
C	120 pN	Amplitude of Active Contraction
k	10^{-2} Pa	Membrane/Cortex Elastic Stiffness
γ	1.6×10^{-2} Pa	Membrane Resting Tension
ϵ	2.29×10^{6} Pa sec/m	Coefficient of Nonspecific Adhesion
A	4.58×10^{4} – 2.29×10^{10} Pa sec/m	Coefficient of Specific Adhesion
T	100 sec	Contraction Period
ℓ_{cont}	1600 µm	Contraction Wavelength

4.2.4 Permeability Bound

We have access to some estimated values of cytoskeletal permeabilities [Ker09, Cha05]. However, these efforts have often focused on dense actin networks (for example, in lamellapodia of migrating keratocytes) and have produced low permeability values on the order of 10^{-5}–10^{-3} µm^2. We regard these estimates as something of a lower bound on reasonable values for the permeability in our model. In well formed flow channels in *physarum*, it is unlikely that a permeability this low accurately describes the intracellular rheology. Under the assumption of a purely Newtonian cell interior (no cytoskeleton), it is possible to estimate an effective permeability which we will regard as an upper bound of reasonable values for our model. We reiterate that the basal-dorsal thickness of *physarum* plasmodia in our preparation is approximately

20 μm, which much less than the posterior-anterior length of the cell. Just as in Chapter 2, we make a thin gap approximation to arrive at the expression

$$\mu \frac{\partial^2 u}{\partial z} = -\frac{\partial p}{\partial x}, \tag{4.9}$$

where z and x are the coordinates in the basal-dorsal and posterior-anterior directions respectively, u is the fluid velocity in the x-direction, and p is the intracellular pressure. Assuming that the pressure is not a function of z, integrating, and imposing the no slip boundary condition at $z = 0$ and $z = 20$ μm allows us to derive the Darcy relation for the z-averaged flow

$$\mu \overline{u} = -\kappa_{\text{eff}} p_x, \tag{4.10}$$

where the permeability $\kappa_{\text{eff}} = (20\ \mu\text{m})^2/12 \approx 33.3\ \mu\text{m}^2$. This may be interpreted as the effective permeability felt by the two dimensional flow in the xy-plane. We reiterate that our model assumes a specially homogeneous drag parameter, while the actual cell interior is heterogeneous. In fully formed flow channels, the permeability of the cell interior may range up to values suggested by the Newtonian approximation, while regions of dense cytoskeleton may exhibit permeabilities in line with those reported in lemellapodia actin networks. For this reason, we estimate a homogenized permeability through the whole cell body. The basic geometry of the cell body is illustrated in Figure 4.2. We assume a cell width of h_{out} and that along the centerline of the cell, there exists a flow channel of width h_{in}. Within the flow channel, viscous effects are relevant, and the average fluid velocity profile obeys the equation

$$\mu \frac{\partial^2 \overline{u}}{\partial y^2} - \frac{\mu}{\kappa_{\text{eff}}} \overline{u} - p_x = 0. \tag{4.11}$$

In the rest of the cell body, which is comprised of denser cortical actin meshwork, the physics are drag dominated and the fluid profile is assumed to obey the Darcy-like equation

$$\mu \overline{u} = \kappa_{\text{cort}} p_x. \tag{4.12}$$

We solve both equations with a matching condition at the flow channel wall ($y = \pm h_{\text{in}}/2$) for the complete flow profile $\overline{u}(y)$. We then calculate the flux through a cross section of the cell due to the given pressure gradient p_x by

$$\overline{Q} = \int_{-h_{\text{out}}/2}^{h_{\text{out}}/2} \overline{u}(y)\, dy. \tag{4.13}$$

Alternately, we calculate the flux due to a flow profile which results when we assume the entire cell interior is composed of a porous material with homogeneous permeability,

$$\tilde{Q} = \int_{-h_{\text{out}}/2}^{h_{\text{out}}/2} \tilde{u}(y)\, dy = -\int_{-h_{\text{out}}/2}^{h_{\text{out}}/2} \frac{\kappa_{\text{tot}}}{\mu} p_x \, dy. \tag{4.14}$$

Finally, we equate $\overline{Q}$ and $\tilde{Q}$ and solve for the unknown homogenized permeability κ_{tot}. We have chosen the values of viscosity and cytoskeletal drag listed in Table 4.1 to be consistent with a homogenized permeability of $\kappa_{\text{tot}} = 3.28\ \mu\text{m}^2$. This resulted from assuming the parameter values listed in Table 4.2.

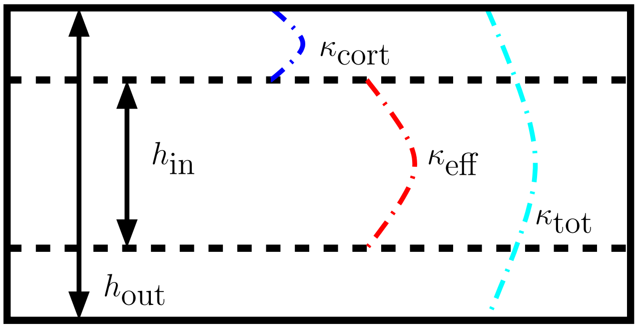

Figure 4.2: Schematic drawing of our homogenization calculation. The inner channel of width h_{in} and permeability κ_{eff} is shown, as well as the outer layer with permeability κ_{cort}. The value κ_{tot}, which we calculate, is shown to hold in the entire domain.

Table 4.2: Parameters for permeability homogenization.

Parameter	Numerical Value	Description
h_{out}	66.6 µm	Cell Width
h_{in}	17 µm	Flow Channel Width
κ_{eff}	$33.3\ \mu\text{m}^2$	Effective Permeability In Flow Channel
κ_{cort}	$10^{-4}\ \mu\text{m}^2$	Cortical Permeability Outside Flow Channel

4.3 Cell Behavior

We begin with a qualitative description of the behavior of migrating *physarum* plasmodia observed by our collaborators Shun Zhang and Juan Carlos del Álamo. Except where noted, this behavior is consistent with the experiments reported in [Mat08], and is included here only for completeness. Upon reaching an adequate size (approximately 100 µm across), our collaborators observe the cells elongate into a tadpole-like shape. Concurrent with this shape change, our collaborators observe the onset of a rhythmic, pulsating flow of cytosol within the cell interior, similar to that reported in [Mat08]. This flow is primarily directed along the cell centerline from the anterior to posterior end of the elongated cell (longitudinal cell axis). The flow has a distinct periodicity of approximately 100.4 ± 14.2 sec (measured over six cells). A region of cytoplasmic flow directed forward develops at the posterior end of the cell. This pattern of forward flow becomes more prominent and travels forward along the cell axis towards the anterior of the cell. Eventually, a region of flow directed backwards will emerge at the posterior end. This rearward flow will also propagate along the cell axis towards the anterior end of the cell, before the entire pattern repeats. Figure 4.3a shows three instantaneous measured velocity fields: a fully developed forward flow pattern, the early formation of a backward directed flow pattern, and a more fully developed backward flow pattern which has propagated most of the length of the cell.

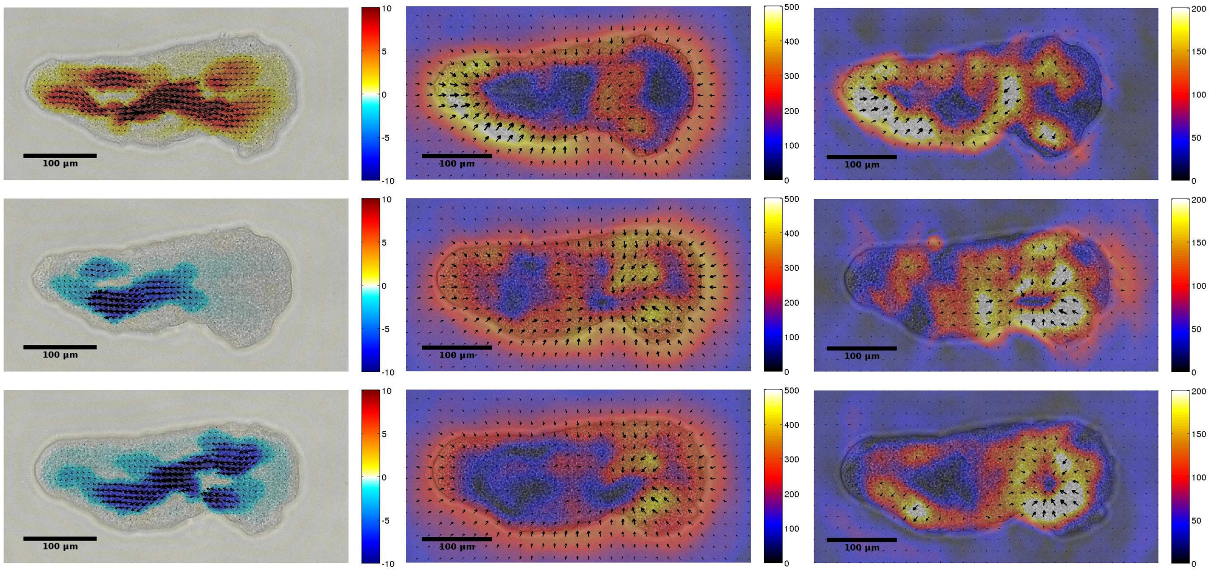

(a) Intracellular flow along the cell axis [µm/sec].

(b) Experimentally measured traction stresses [Pa].

(c) Traction stresses with moving average removed [Pa].

Figure 4.3: Instantaneous intracellular flow and traction stresses observed in migrating *physarum*. In (a) arrows indicate the direction of flow. Colormap indicates the projection of flow velocity onto the cell axis. In (b) & (c) arrows indicate the direction of traction stress field. Colormap indicates the magnitude of stress field. Provided courtesy of Shun Zhang and Juan Carlos del Álamo.

The emergence of this periodic wave of back-and-forth flow is observed to coincide with a dramatic increase in the migration velocity of the cell, as in [Koy98]. The migration of the cell is necessarily accompanied by the application of traction stresses to the underlying substrate. Figure 4.3b shows a sequence of the stresses applied to the substrate by *physarum* at three time points which are approximately those reported in Figure 4.3a. There is a slight delay between the images of Figures 4.3a & 4.3b due to changing the imaging channel of the microscope from bright field to florescent field.

The dominant feature of this traction stress pattern is purely contractile, and the larger traction stresses are found near the cell periphery. This behavior has been observed in other cell types, and it has been hypothesized that this effect is due to strong stresses associated with the cell cortex and directed out of the plane of the substrate [DA13]. Our collaborators remove this average "cortical" stress pattern from the measured traction field. This will aid in comparison to our model, as the model is restricted to representing forces generated in-plane. The average traction stress field is calculated by averaging the instantaneous traction stress field mentioned above for at least two complete periods of the observed behavior. The average contractile stress is then removed from the instantaneous traction stress field. The resulting stress patterns are shown in Figure 4.3c. Once the average cortical stress is removed, we observe that the dominant feature of the stress field is a locus of contractile stress which develops near the rear of the cell. This locus travels forward along the longitudinal axis of the cell before a weaker locus of *expansive* stress begins to develop at the posterior of the cell. This apparently phase wave behavior of traction stress supports our assumption of the functional form of adhesion strength Equation (4.8).

4.4 Model Behavior

In Figure 4.4a we show instantaneous fluid velocity fields obtained from the model at time intervals roughly analogous to Figure 4.3. In these simulations, the phase and amplitude of the adhesion wave were set to $\phi = 3\pi/2$ and $A = 100\epsilon$, respectively. In Sections 4.6 & 4.7 we will return to consider other adhesion parameters. The three panels illustrate a fully formed forward flow, the onset of a backward flow, and a fully developed backward flow pattern which has travelled towards the anterior of the cell. Qualitatively, they are very similar to the behavior shown in Figure 4.3a. We also calculate the traction stresses applied to the substrate by our model cell ($\boldsymbol{F}_{\text{trac}}$). These stresses must necessarily balance the stress exerted by the substrate on the adhesive points in our model. Therefore

$$\boldsymbol{F}_{\text{trac}} = -\boldsymbol{F}_{\text{subs}}. \tag{4.15}$$

In Figure 4.4b we provide illustrations of traction stress fields generated by our model cell during the same simulation shown in Figure 4.4a. The three panels show the forward propagation of a contractile locus of stress through the cell body, followed by the emergence of a weaker expansive locus of stress at the posterior end of the cell. In this regard, the model again reproduces the qualitative behavior observed in live *physarum*.

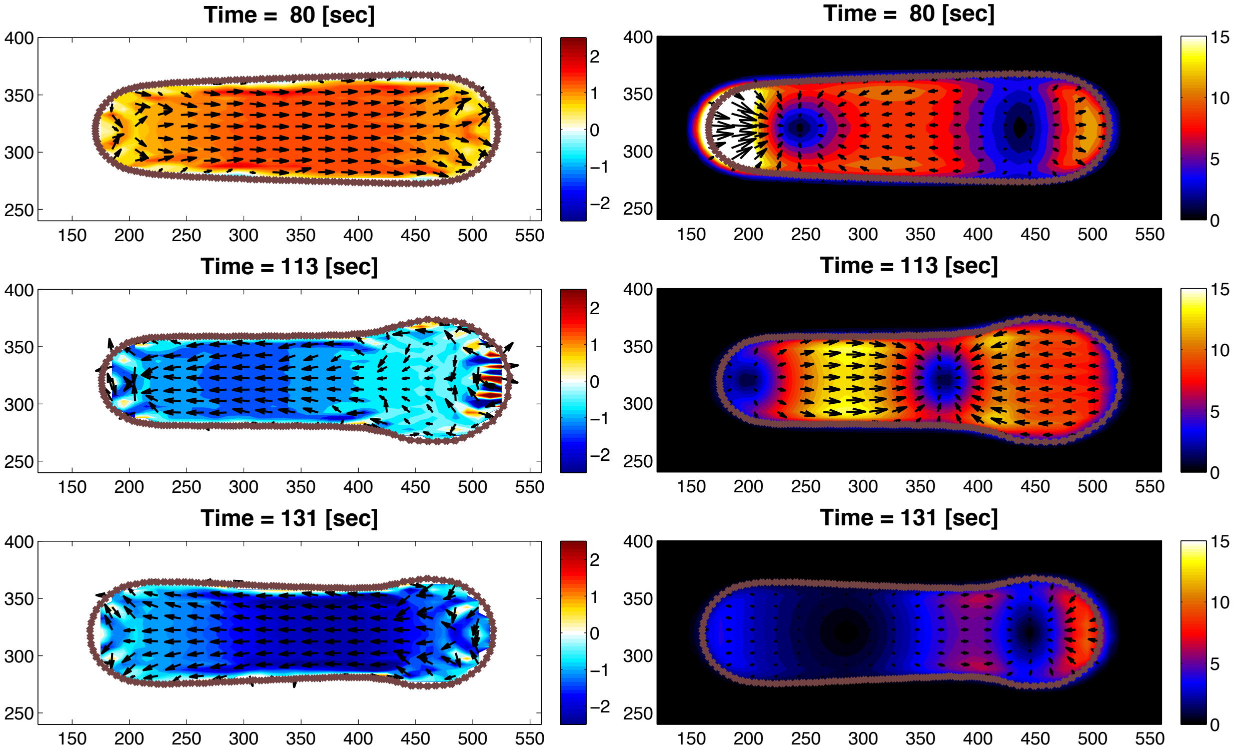

(a) Computed cytosol velocity field [µm/sec].

(b) Computed traction stress field [Pa].

Figure 4.4: Instantaneous intracellular flow and traction stresses computed in model cell. In (a) arrows indicate the direction of flow. Colormap indicates the projection of flow velocity onto the cell axis. In (b) arrows indicate the direction of stress field. Colormap indicates the magnitude of stress field.

To further analyze the flow patterns that we observe, we generate kymographs of the intracellular flow. This is done by averaging the calculated longitudinal flow over each lateral cross section of the cell. That is, we calculate the "mean longitudinal flow,"

$$\bar{U}(x,t) = \frac{\int_{\Omega_c} \boldsymbol{u}_f \cdot \hat{x}\, dy}{\int_{\Omega_c} dy}, \tag{4.16}$$

where Ω_c denotes the interior of the cell, x is the Eulerian coordinate parallel to the longitudinal cell axis, and y is the coordinate orthogonal to the longitudinal axis. Figure 4.5a shows experimentally obtained measurements of $\bar{U}$ while Figure 4.5b shows those produced by the model cell shown in Figure 4.4. Given the lack of precise values for much of the intracellular rheology of *physarum*, it is not our goal to achieve precise agreement between the model and experiment. Regardless, the model agrees qualitatively with the flow patterns observed experimentally in live *physarum*, and reproduces the correct magnitude of flow speed within one order.

In our numerical simulations of the model, we observe flows in good agreement with those reported

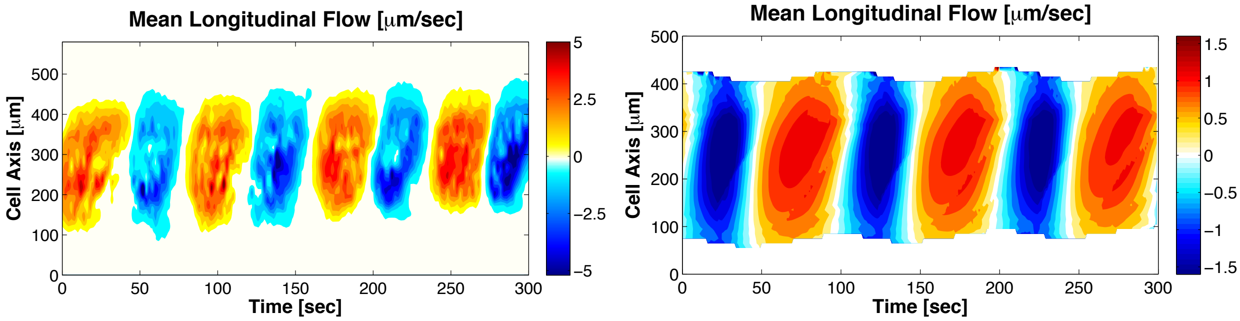

(a) Experimentally measured values.

(b) Numerically calculated values.

Figure 4.5: Kymographs of mean longitudinal flow $\bar{U}$. Experimental values are unpublished data courtesy of Shun Zhang and Juan Carlos del Álamo. Model calculations performed with $\phi = 3\pi/2$ and $A/\epsilon = 100$.

by our collaborators and in [Mat08]. A phase wave pattern is clearly evident, where regions of forward and rearward flow are generated at the tail of the cell, and propagate toward the head in an approximately linear fashion. Forward and rearward flow patterns are separated by a "stagnation" point which also travels quickly from the posterior to the anterior end the cell. This phase wave propagates through the cell at the "phase velocity", which we will denote c_ϕ. In [Mat08], c_ϕ was referred to as the "shifting velocity," and was speculated to play a central role in motility. We note here the phase velocity is distinct from any actual fluid velocity observed within the cell. In previous experiments this phase velocity has been reported as $c_\phi = 12 \pm 1$ μm/sec [Mat08]. However, our colaborators observe larger phase velocities in their experiments. For the cell shown in Figure 4.5a, the phase velocity is measured to be $c_\phi = 29.4$ μm/sec. In general, they measure phase velocities of $c_\phi = 23.8 \pm 12.0$ μm/sec across their experiments. We perform model simulations varying the phase parameter (ϕ) over eight equally spaced values from 0 to 2π, and the coefficient of adhesion (A) over 6 orders of magnitude. Regardless of the form of adhesion, our model predicts phase waves of flow in good agreement with experimental observations. We measure phase velocities in the range $24 \leq c_\phi \leq 38$ μm/sec (See Figure 4.6).

4.5 Role of Flow

It is argued in [Mat08] that the asymmetry of displacement by particle moving in such a phase wave flow pattern is directly responsible for the net displacement of the cell over one period. Following this argument, Figure 4.7a illustrates particle paths in an idealized flow where regions of forward (red) and backward (blue) flow (of a constant velocity) propagate through the cell body as a phase wave. A particle within the fluid will translate a distance D_f forward over one period of the flow, and a distance D_b backward. As the

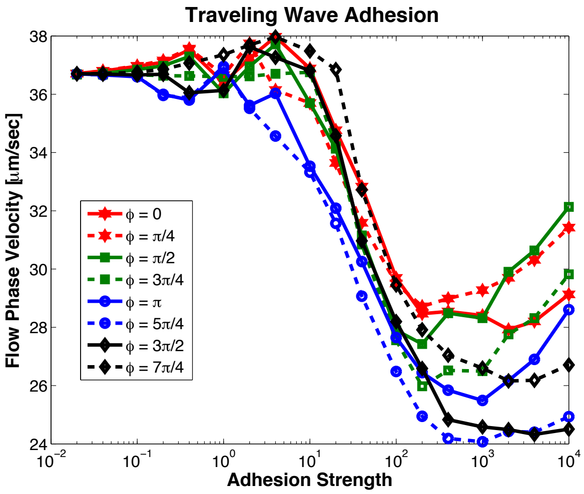

Figure 4.6: Phase velocity of calculated intracellular flow as a function of adhesion strength.

particle is in a region of forward flow for more than half the period of the oscillation, D_f will be greater than D_b. That is, there will be a net forward displacement of the particle over one period of the wave. We define the asymmetry in the flow to be the ratio D_f/D_b. Figure 4.7b shows the displacement of the centroid of a *physarum* specimen provided by our collaborators. The distance that the cell centroid moves forward (backward) over one period of the wave is labelled L_f (L_b). The ratio L_f/L_b is the centroid displacement asymmetry. In Figure 4.7c, we plot the asymmetry in the flow as a function of the centroid displacement asymmetry. This data is provided by our collaborators, and was measured over 118 periods of flow for 9 cells. Each point of data represents one period of the flow wave measured in a single cell. If the flux of mass due to the intracellular flow wave were solely responsible for the migration of the cell center of mass, then the data in Figure 4.7c would lie on the green dashed line with slope 1. However, we see that this line is in fact a poor fit to the data. The solid blue line shows the best linear fit to the data, and it has a much lower slope of approximately 0.16.

Examining Figure 4.7c more closely reveals a critical phenomenon. We divide the figure into quadrants defined by the lines $D_f/D_b = 1$ and $L_f/L_b = 1$ (shown in grey). There are 55 data points with a flow asymmetry less than 1. This implies that $D_f < D_d$ for those periods of the wave-like behavior. However, 53 of these data points lie in the region where the centroid displacement asymmetry is greater than 1. Therefore the particle displacement due to flow suggests a net *backward* translation of mass, even though the cell has moved forwards. While flow is likely to play a major role in the migration of *physarum*, our collaborators' experiments (and our model predictions in Section 4.6) indicate that hydrodynamics alone cannot determine the migration of the cell. Some other mechanism is responsible for the net forward displacement of the cell center.

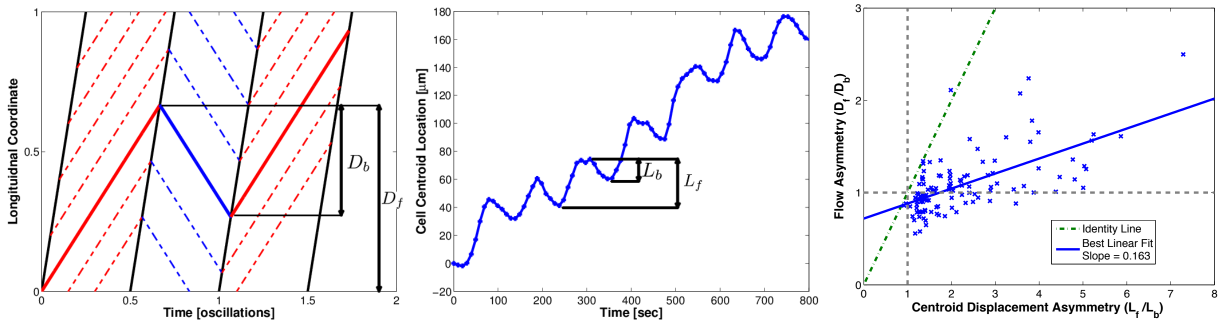

(a) (b) (c)

Figure 4.7: In (a) we provide an illustration of the particle paths associated with a constant phase wave. The two components of flow asymmetry (D_f and D_b) are shown. In (b) we show the time series of the centroid of a migrating *physarum*. The two components of centroid displacement asymmetry (L_f and L_b) are indicated. In (c) we show experimentally measured values of flow and centroid displacement asymmetry over 118 periods and 9 cells. The best linear fit is shown in blue. A perfect one to one correspondence is shown in green for comparison. Unpublished data courtesy of Shun Zhang and Juan Carlos del Álamo.

4.6 Adhesion Coordination and Crawling Speed

Figure 4.8a shows the translation of the centroids of three cells simulated with the model using different forms adhesion coordination. Figure 4.8b shows the flow patterns calculated in these three cells. Cell A utilizes a phase parameter of $\phi = 3\pi/2$ and an adhesion coefficient of $A = 100\epsilon$. Cell C utilizes the same adhesion coefficient, and a reversed phase parameter of $\phi = \pi/2$. Cell B was simulated with $\phi = 3\pi/2$ and adhesion coefficient $A = 0$. All three of these cells are driven with the same contraction pattern, but more importantly exhibit very similar flow patterns (See Figure 4.6) which are all consistent with both our experiments and experiments of others [MAT08, KOY98]. However, while cell A migrates forward consistent with experimental observations, cell B shows no net translation over the course of the simulation, and cell C migrates *backwards*. The implication is that while hydrodynamic effects may generate stresses integral to motility, it is the coordination of the transmission of those stresses to the substrate that ultimately determines motility. Furthermore, from Cell B we see that *coordinated* adhesion is critical to motility. A cell migrating using just the nonspecific, uncoordinated adhesion (ϵ) fails to migrate.

For comparison, Figure 4.7b provides a time course of the center of a *physarum* specimen migrating in the lab. Qualitatively, the predicted migration behavior of model cell A closely matches that observed in our

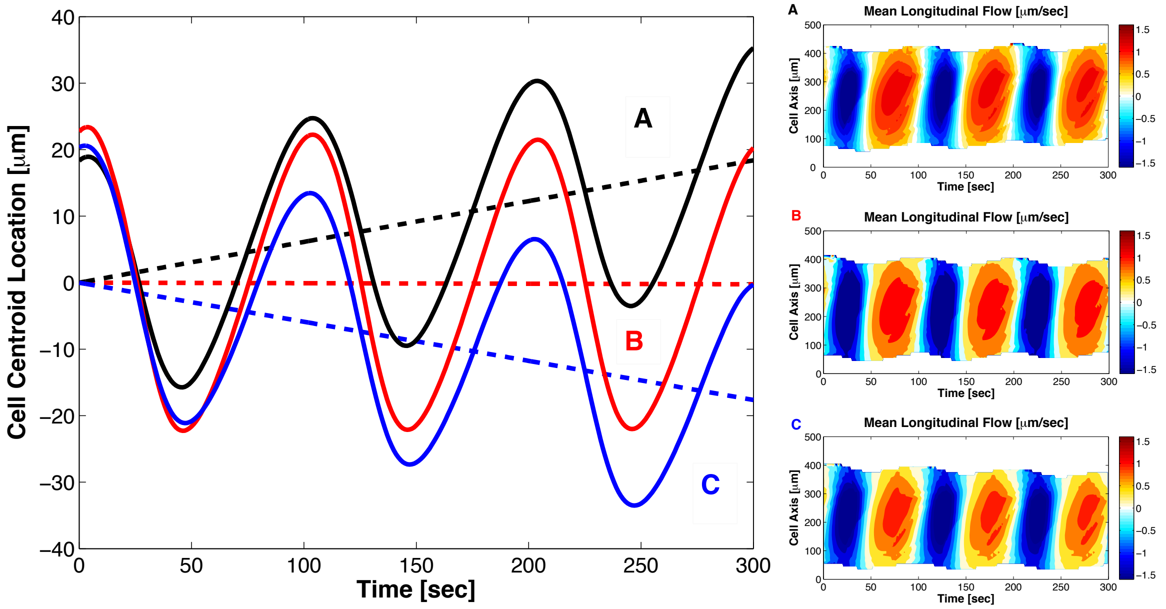

(a) Model cell centroid displacements

(b) Flow kymographs

Figure 4.8: Numerically calculated time evolution of cell centroid is shown in (a). The solid lines indicate the centroids of individual cells, while the corresponding dashed lines indicates a best (least squares) linear fit. Migration speeds reported are given by the slope of this fit. Flow velocity kymographs for the same model cells are shown in (b).

experiments. We see a distinct, periodic translation forward and backward. However, there is a pronounced asymmetry to the two translations, ($L_f \neq L_b$) and the result is a net forward displacement of the cell over one full period. For the simulation shown, the net displacement of the model cell is approximately 6 μm per period of the oscillation. This is equivalent to an average migration velocity of approximately 0.06 μm/sec. In the laboratory, we measure *physarum* migrating at speeds of 0.16 ± 0.04 μm/sec across the 9 cells which exhibit peristaltic behavior. Thus, our model predicts cellular migration of a character and scale in reasonable agreement with experiments. This also suggests that coordination of adhesion and contraction is essential for efficient locomotion.

We now explore the speeds of migration predicted by the model as a function of adhesion strength and coordination. We perform simulations varying the phase parameter (ϕ) over eight equally spaced values from 0 to 2π, and the coefficient of adhesion (A) over 6 orders of magnitude. All parameter values give rise to similar periodic displacements the cell centroid (as shown in Figure 4.8a). However, depending on the phase and strength of adhesion, our model predicts various translation velocities and *directions* of migration. The results are summarized in Figure 4.9.

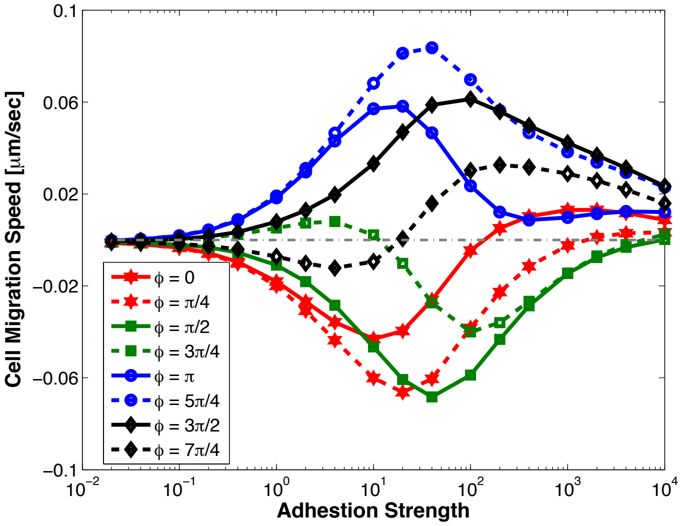

Figure 4.9: Average cell crawling speed as a function of adhesion coefficient and adhesion phase. Adhesion coefficient is reported in non-dimensional units $[A/\epsilon]$.

We observe that the migration velocity of the model cell is a non-monotonic function of adhesion coordination and strength. Indeed, the cell speed is maximal at moderate values of coordinated adhesion strength, while weakly or strongly adherent cells display negligible migration. In the limit $A << \epsilon$, the coordinated adhesion is negligible compared to the uniform, uncoordinated adhesion. In this case, the cell cannot move with a directional bias, despite generating periodic flows and displacements (see cell B in Figure 4.8a). In the limit of strong adhesion $A >> \epsilon$, the cell is effectively stuck to the substrate and cannot move, regardless of how this adhesion is coordinated. This result is similar to investigations which claim that migration of other cell types is maximized at intermediate values of other adhesion parameters. Theoretical modeling has indicated a biphasic relationship between velocity and integrin density in mesenchymal cells [DiM91]. Also, experiments have shown a similar biphasic dependence on substrate compliance in embryonic neurons [Cha08a]. To our knowledge, no experiments have been performed with *physarum* which demonstrate this optimal range of adhesion, however our model suggests that the results of such an experiment would be qualitatively similar to the existing literature.

We also note that the velocity of cell migration is approximately symmetric in the phase parameter ϕ. For a cell migrating with velocity v, altering the phase of the adhesion wave $\phi \to \phi + \pi$ (keeping all other parameters fixed) results in a new migration velocity approximately $-v$. Intuitively, this can be understood as "reversing" the coordination of adhesion relative to contraction, resulting in locomotion in the opposite direction. As we have discussed, this implies the hydrodynamic mechanism of motility hypothesized in [Mat08] is not sufficient to explain directed *physarum* migration.

As each simulation is driven with active contractions of the same amplitude and form, we may consider migration speed of the cell as a measure of efficiency. The cell translates most efficiently with an active adhesion coefficient of $A/\epsilon \approx 10$–100, and a coordination phase of $\phi \approx \pi$–$3\pi/2$. Thus, the model predicts an optimal parameter regime in which to drive motility.

4.7 Adhesion Correlation

Our model indicates that a traveling wave of adhesion coordination may produce locomotion on biologically relevant scales. However, there is no *a priori* evidence that *physarum* is coordinating adhesion stresses in this manner to generate the motility observed. In order to address this question, we investigate the characteristic adhesion stresses that the model cell applies to the substrate during locomotion, and compare these to experimentally measured values.

4.7.1 Traction Stress Patterns

For comparison with experimental data, we generate kymographs of adhesion stresses by defining the quantity

$$T(x,t) = \frac{\int_{\Omega_c} \boldsymbol{F}_{\text{trac}} \cdot \hat{x}\, dy}{\int_{\Omega_c} dy}. \tag{4.17}$$

T is a measure of the average traction stress *in the direction of motion* applied to the substrate at each cross section of the cell body. Figure 4.10a shows a kymograph of traction stresses measured in our collaborators' experiments (with average cortical stresses removed). The data displayed are qualitatively representative their experiments. In the kymograph we see a distinct phase wave of traction stress similar to the flow kymographs in Figure 4.5. We now qualitatively compare the traction stress kymographs experimentally measure to those produced by numerical simulations. Figure 4.10b shows a traction stress kymograph for a numerical cell migrating with a phase parameter $\phi = 3\pi/2$, and adhesion strength $A = 100\epsilon$. This simulation was chosen because the cell migrates with a velocity of the correct scale (approximately 0.06 µm/sec), and exhibits the maximum migration velocity among other cells utilizing the same phase parameter. The simulated cell produces a phase wave of traction stress that has a district character, with intervals of relatively low stress disrupting the pattern each period of the wave (for example at ~ 130 sec), however

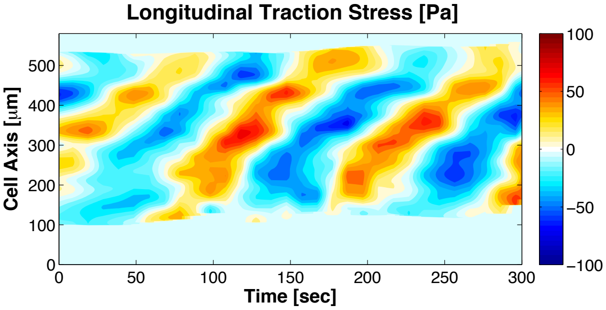

(a) Measured traction stresses exerted by live *physarum* with moving average removed.

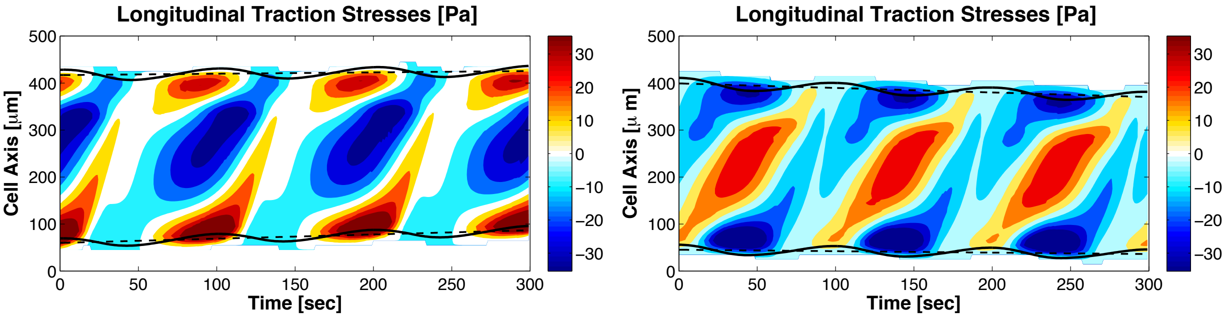

(b) Model traction stresses with $\phi{=}3\pi/2$, and $A/\epsilon{=}100$. (c) Model traction stresses with $\phi{=}\pi/2$, and $A/\epsilon{=}100$.

Figure 4.10: Average traction stresses applied to substrate by migrating cells and numerical simulations. Experimental values are unpublished data courtesy of Shun Zhang and Juan Carlos del Álamo.

the traveling wave pattern is clearly evident. While the numerically calculated traction kymograph reproduces some features of the traction stresses observed in live *physarum*, it is at this point unfair to say that it fully captures the observed stresses generated by migrating cells. Furthermore, Figure 4.10c shows the traction stress pattern generated by a model simulation with the same strength of adhesion, but a phase parameter $\phi = \pi/2$. This simulation also produces a distinct phase wave of traction stress with a similar character. However, this parameter set results in migration in the *opposite* direction. It is difficult to identify which adhesion parameters most closely reproduce the spatio-temporal pattern of the traction stress kymographs observed in our collaborators' experiments. For this reason we develop a more quantitative analysis of the coordination of adhesion to compare experiments and our model results.

4.7.2 Flow and Energy Correlation

We now calculate the total elastic energy of adhesion associated with the traction stress,

$$E_{elas} = \int\limits_{\Omega_c} \frac{1}{2} \left(\boldsymbol{F}_{\text{trac}} \cdot \boldsymbol{c} \right) \, d\boldsymbol{s} \tag{4.18}$$

where $\boldsymbol{c}$ is the local elastic displacement. In our collaborators' experiments, $\boldsymbol{c}$ measures the elastic deformation of the substrate. In our numerical model, $\boldsymbol{c}$ measures the deformation in the elastic elements which connect the cytoskeleton to the adhesive points. First, we examine the time evolution of the experimentally measured elastic strain energy produced by live migrating *physarum*, and compare it with the evolution of the average intracellular flow velocity. The first panel of Figure 4.11a shows the time course of both average flow velocity within the cell interior, and total elastic energy due deformation of the substrate. We observe a distinct periodic pattern in both the flow velocity, as well as the adhesion energy, with the flow wave preceding the adhesion wave by approximately a 30% of a period (Figure 4.11a, left panel). This behavior is robust across the 9 reported experiments. To more precisely quantify this phase relationship between flow and adhesion energy, we calculate the cross correlation of the two time series. The cross correlation of two functions is defined to be

$$(f \star g)(\tau) = \int_{-\infty}^{\infty} f(t) g(t+\tau) dt. \tag{4.19}$$

However, for ease of interpretation, we first remove the mean of each signal before performing the cross correlation. We also normalize so that $(f \star f)(0) = 1$. The left panel of Figure 4.11a shows the cross correlation of flow and adhesion energy, as well as the cross correlation of the flow wave with itself (autocorrelation). The time between peaks of the autocorrelation function is interpreted as the period T of the flow wave oscillation (illustrated in Figure 4.11b). The position peaks of the cross correlation function indicate the relative timing of the flow and energy waves. We define the occurrence of the first local maximum of the cross correlation function (restricted to times $t > 0$) as our measure of relative timing. This quantity is denoted θ and is illustrated in Figure 4.11a. The ratio θ/T defines the relative phase (between 0 and 1), which our collaborators measured to be 0.34 ± 0.07 in their experiments.

We perform the same analysis for the model simulations. In Figure 4.11b, we report the average intracellular fluid velocity and elastic strain energy within the model adhesions, as well as the auto and cross correlation of these two time sequences. The data shown is for a cell with phase parameter $\phi = 3\pi/2$ and adhesion strength $A = 100\epsilon$. This is the same parameter set for Cell A in Figure 4.8 and the kymograph in Figure 4.10b. For this phenomenological idealized model of adhesion, and for these parameters, the model seems to accurately reproduce the observed phase relationship between flow and energy waves. We see a clear phase lag of approximately a quarter period. In contrast, Figure 4.11c shows the correlation we obtain with $\phi = \pi/2$ and adhesion strength $A = 100\epsilon$. This is the same parameter set for Cell C in

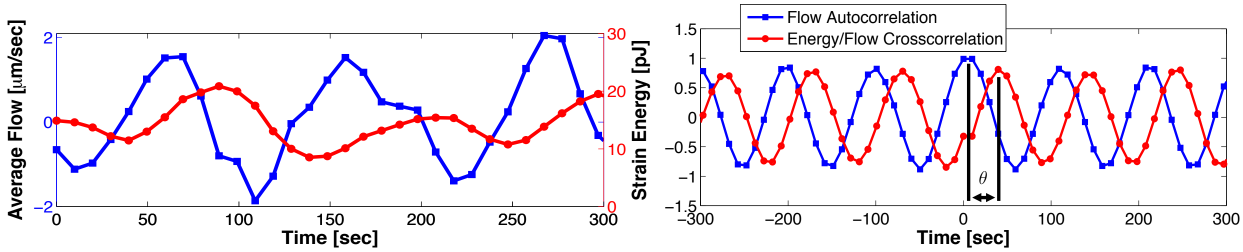

(a) Experimentally measured flow and energy.

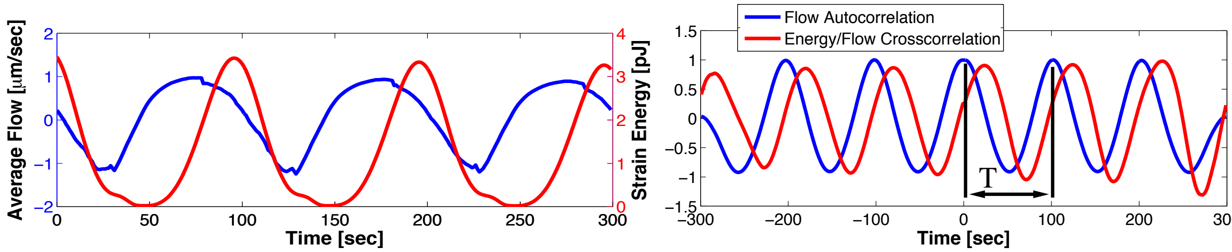

(b) Numerically calculated flow and energy for ϕ=$3\pi/2$ and A/ϵ=100.

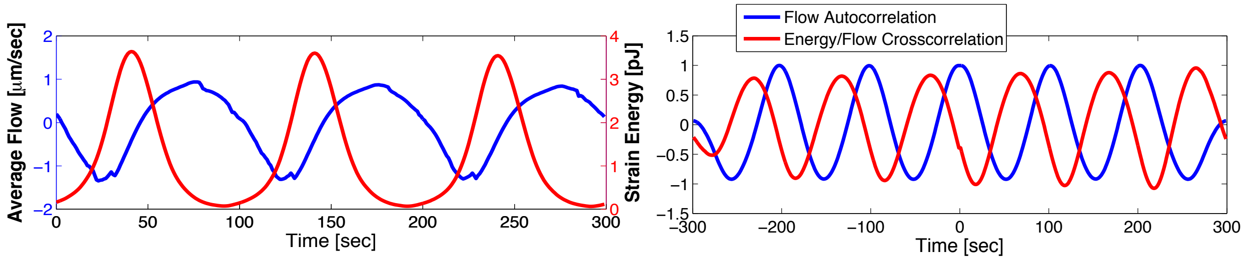

(c) Numerically calculated flow and energy for ϕ=$\pi/2$ and A/ϵ=100.

Figure 4.11: Left panel shows average flow velocity within the cell interior, as well as total strain energy of adhesion as a function of time. Right panel shows auto and cross correlation of flow and energy. Experimental values are unpublished data courtesy of Shun Zhang and Juan Carlos del Álamo.

Figure 4.8 and the kymograph in Figure 4.10c. We see a clear phase *advance* of the energy wave, relative to the flow wave. This is inconsistent with experiments.

We now utilize the phase relationship between flow and energy to identify plausible adhesion parameters for our model. We calculate the peak correlation for all simulations shown in Figure 4.9. The results are shown in Figure 4.12a, where we report the ratio θ/T for all adhesion parameters. For reference, the relative phase observed in experiments (0.34 ± 0.07) is illustrated with the solid and dashed grey lines. We see that the relative phase of adhesion energy appears to be highly sensitive to ϕ, and relatively insensitive to adhesion strength. The exception to this is for weak coordinated adhesion (below the range $A \approx \epsilon$). In this case, all phase parameters ϕ appear to give the same relative timing in the limit of small A. This is to be expected, as the phase of coordinated adhesion is unimportant in the limit of purely uncoordinated adhesion. Values of ϕ in the range $3\pi/2$–2π (2π and 0 are equivalent) produce a relative timing which is consistent with experimental measurements. Of these parameter values, $\phi = 3\pi/2$ is the only one which produces migration in the forward direction regardless of the strength of coordinated adhesion (See Figure 4.9). For cells using a phase parameter $\phi = 3\pi/2$, the measured phase lag between flow and strain energy remains in the range 0.21–0.33 when varying the adhesion strength over 6 orders of magnitude. Specifically, in the case of highest migration velocity (the parameter set used to produce Figure 4.10b), we measure a phase lag of 0.25. In Figure 4.12b we plot the maximum measured migration speed as a function of the average timing of flow and energy (θ/T) for each value of ϕ. This illustrates that of the three phase parameters which reasonably consistent with experimentally observed timing, $\phi = 3\pi/2$ produces the maximal migration speed.

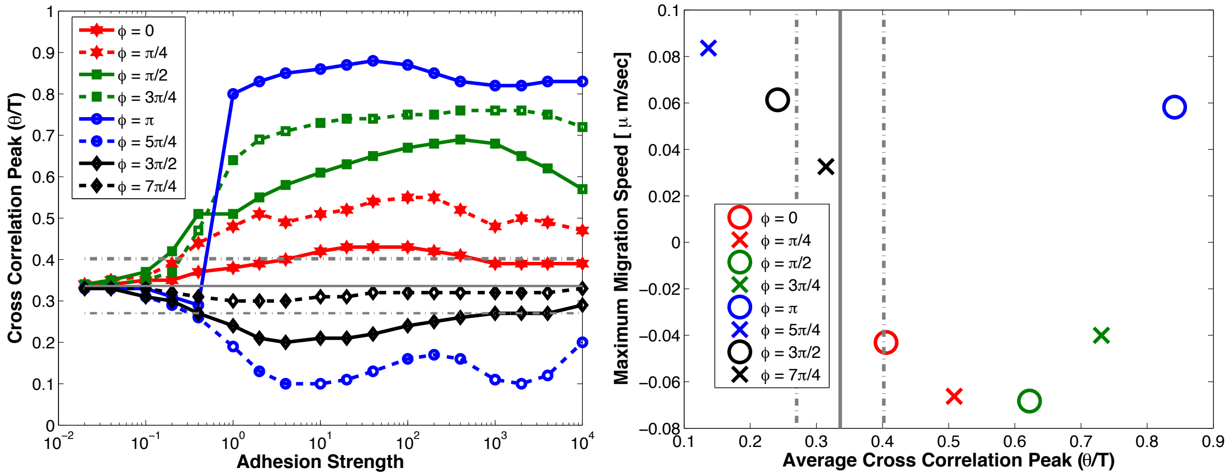

(a)

(b)

Figure 4.12: (a)Maximum cross correlation of elastic energy of adhesion and average cytoplasmic flow. Adhesion coefficient is reported in non dimensional units $[A/\epsilon]$. Horizontal grey lines indicates experimentally measured phase of 0.34 ± 0.07. (b) Maximum migration speed as a function of average cross correlation peak (average calculated for for adhesion coefficient $A \geq \epsilon$). Vertical grey lines indicates experimentally measured phase of 0.34 ± 0.07

4.8 Robustness

From the criteria discussed in the previous section, the spatio-temporal pattern of adhesion which is most consistent with experimental evidence corresponds to a phase parameter of $\phi \approx 3\pi/2$ and a strength of $A \approx 100\epsilon$. It is also the case that these parameters predict nearly optimal migration velocity within the constraints of the model. Moreover, it is noteworthy that this the migration velocity for the phase parameter is not very sensitive to the strength of adhesion. Returning to Figure 4.9, we see that the cell migrates maximally at approximately 0.06 µm/sec. However, the model predicts a migration velocity above 0.03 µm/sec (roughly 50% of optimal) over more than *two decades* of adhesion strength. This suggests that the migration velocity is quite robust with respect to the strength at which the cell is adhering to the substrate. We seek to further quantify this notion.

The simulations in Figure 4.9 do not fully address robustness with respect to adhesion strength because they only consider spatially uniform substrate. In relevant environments, the strength of adhesive interactions between the cell and substrate is not homogeneous, as numerous environmental and intracellular factors may affect such interactions. Therefore, we use our model to quantify the robustness of migration with respect to spatial variations in adhesion strength. We alter the model of cell adhesion to the substrate in order to incorporate spatial heterogeneity. We replace our existing model of adhesion (equation (4.8)) with the following:

$$\zeta(\boldsymbol{s}, t) = \frac{A}{2} g(x, y) \left(\cos\left(\frac{2\pi}{\ell_{\text{adh}}} (\boldsymbol{s} \cdot \hat{x}) - \frac{2\pi}{T} t + \phi \right) + 1 \right) + \epsilon, \tag{4.20}$$

where $g(x, y)$ is a randomly constructed function of mean of $\mu_r = 1$ and standard deviation of $\sigma_r = 0.34$ (for further details, see Appendix D). This has the effect of spatially modulating the strength with which the cell adheres to the substrate. The inset of Figure 4.13a shows a single randomly generated example of the spatial heterogeneity $g(x, y)$.

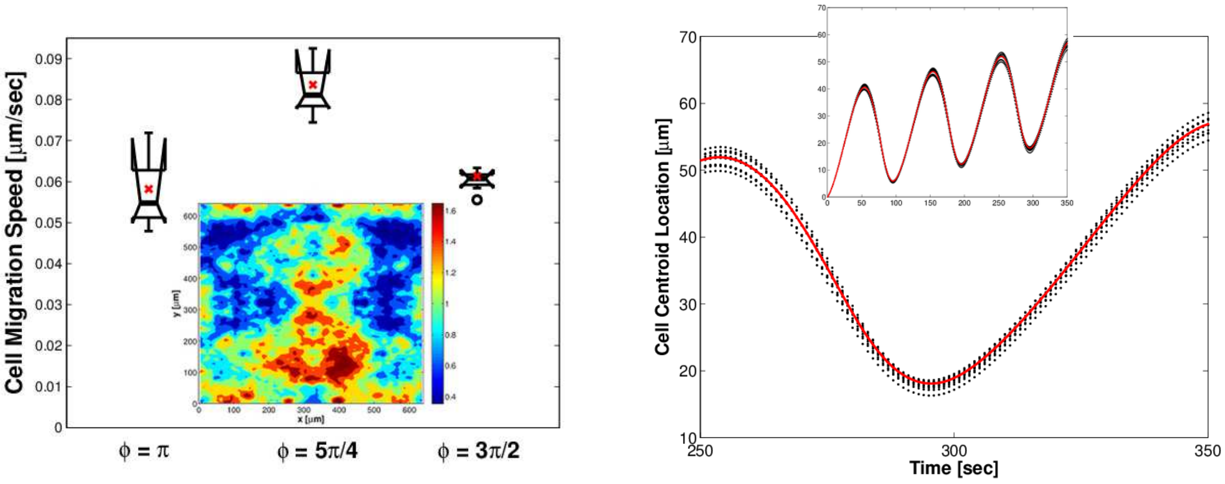

(a)

(b)

Figure 4.13: (a) Open circles indicate outliers in data set. Filled red points indicate the migration velocity calculated for a cell migrating across a homogeneous substrate. The inset shows a single randomly generated substrate. (b) Dashed black lines indicate time course of centroids of cells migrating across random substrate. Solid red line indicates cell migrating across homogeneous substrate. $\phi = 3\pi/2$ in all cases.

Using the randomly constructed function g to represent a heterogeneous substrate, we simulated cells migrating across ten different substrates. We performed these simulations for the three values of ϕ which generically resulted in forward migration, and values of coordinated adhesion that results in the greatest migration velocity for each phase parameter. These values were $\phi = \pi$, $5\pi/4$, and $3\pi/2$, with $A = 20\epsilon$, 40ϵ, and 100ϵ respectively. The migration velocities of each set of model cells was calculated and the results are summarized in the box plot in Figure 4.13a. The spread of the data shows that migration speed is relatively insensitive to substrate heterogeneity for the considered values of ϕ. We measure mean and standard deviations of 0.058 ± 0.009, 0.083 ± 0.006, and 0.060 ± 0.002 µm /sec for $\phi = \pi$, $5\pi/4$, and $3\pi/2$ respectively. Notice that the value $\phi = 3\pi/2$, which is most consistent with our collaborators' live *physarum* experiments produces a substantially lower spread in migration speed, with fully half the data falling within $\pm 2.5\%$ of the median value. Thus, we see that this mode of adhesion coordination is highly robust with respect to local variations in the strength of adhesive interaction with the substrate.

The observed robustness is consistent through the whole migration period of the cells. Figure 4.13b shows the time evolution of the centroid of the 10 cells (migrating across 10 random substrates) with $\phi = 3\pi/2$ (black). For comparison, we also show the time evolution of a cell migrating across homogeneous substrate (red). The insets show the full time course, while the main panels show just the final 100 sec of migration. Over time, the location of the cells migrating across random substrates begins to deviate from that of the cell migrating across the homogeneous substrate. This is to be expected, as random effects accumulate over time. However, these deviations are quite small compared to the scale of cell migration. Our model indicates that, for the set of model parameters that reproduce the experimental measurements, the overall speed of migration is remarkably insensitive to the spatial heterogeneity of the substrate.

4.9 Discussion

In this chapter, we compared simultaneous measurements of cytoplasmic flow and the traction stresses exerted on the substrate by migrating *physarum* microplasmodia with detailed computational models of amoeboid migration that resolve the mechanics of cellular deformation and substrate adhesion. Our collaborators' measurements allow the correlation the stresses applied to the substrate with the previously observed wave of flow. They reveal that *physarum* amoebae move by creating traveling waves of contractile traction stresses with a well defined period of ~ 100 sec. The traction stress waves are similar in character to the previously observed waves of intracellular flow, but the stress waves consistently precede the flow waves by $\sim 1/3$ cycle. Inspired by this observation, we use our numerical model to investigate the consequences of migration using traveling waves of coordinated contraction and adhesion. These investigations show that the directionality of the flow wave does not determine migration of the cell. Rather, by altering the timing of adhesion relative to the flow wave, the cell is able to migrate with different velocities and in different directions. These findings alter the previously established view that directional migration of *physarum* amoebae is caused by the directionality of the flow waves [Mat08].

By juxtaposing our modeling and our collaborators' experimental work, we have identified specific forms of stress generation and transmission which plausibly drive the migration of *physarum* amoebae. Within the context of our phenomenological adhesion model, our simulations and collaborators' experiments indicate a small range of phase relationships ($\phi \approx 3\pi/2$) between contraction and adhesion which is consistent with experimental measurements in the following ways: the magnitude and qualitative character of the cytoplasmic flows, the magnitude and qualitative character of traction stresses, the correlation of adhesion energy to intracellular flow, and the scale of cell migration speed. This coordination pattern consists of a phase lag of $3/4$ cycle between adhesion and contraction ($\phi \approx 3\pi/2$). This result validates the model, but also provides insight into the underlying mechanism of amoeboid motility. The particular adhesion coordination pattern we highlight is extremely robust to perturbations in adhesive interactions with the extracellular environment, and results in nearly optimal migration within the context of the model. It should be noted that the adhesion coordination pattern that produces maximum migration speed ($\phi = 5\pi/4$) indicated by our model is not totally consistent with experimental observations. In particular, this adhesion coordination does not properly reproduce the relative timing of flow and strain energy (See Figure 4.12a). Furthermore, as shown in Figure 4.13a, the most efficient form of adhesion is *not* the most robust one. This insight into the potential compromises of different adhesion coordination would not have been possible through experimental investigations alone. Our model allows us a direct control over the coordination of adhesion that we are unable to reproduce in a laboratory setting.

We note that our frictional adhesion model is in some sense independent of the precise nature of the molecular level cell-substrate interactions. While our friction based adhesion model was justified as a time-averaged effect of integrin-like molecular binding, this assumption is not necessary to arrive at the precise mathematical form that we use. Indeed, it is not precisely known how *physarum* exerts stresses on its surroundings. Cell-substrate stresses may be a result of purely passive frictional interactions. This is consistent with our modeling framework, as the modulation of the strength of friction (which we *call* coordinated adhesion, purely as a naming convention) may be a result of a variety of factors (such as intracellular pressure generating forces normal to the substrate). We also note that it is unlikely that *physarum* migrate *in vivo* utilizing adhesive patterns as simple as our idealized model of wave adhesion. In general, the modulation of interactions with the substrate may be an emergent behavior of complex interplay of mechanical and chemical signaling [Ber06], and most likely cannot be perfectly described in such a simple functional form. However, given the well documented traveling wave of flow within *physarum*, it is reasonable to assume that the effective signal propagation is correlated with the wave of flow.

While somewhat unique, the motility of *physarum* microplasmodia we investigate in this work shares fundamental characteristics with other forms of amoeboid migration. Rythmic cellular contractions of period $\sim$ 100 sec are known to drive the motion of neutrophil-like and *Dictyostelium* amoeboid cells [DA07, Bas14]. In particular, while hydrodynamics do not fully determine the motility of *physarum*, it appears that cellular contractions are used to generate intracellular flows and cell locomotion. The use of pressure-driven flows of cytoplasm to generate translation has been widely observed in the context of motile cells [Läm09, Toz13, Bas14]. Furthermore, we reiterate that the observed motility of *physarum* is consistent with a model of cell-ECM interaction hat does not require specific integrin-like binding molecules. It has been shown that neutrophils undergo amoeboid migration in three dimensional environments in the absence of specific binding molecules [Läm08]. This contributes to the growing notion that friction mediated motility is biologically advantageous, as it is robust to geometric and mechanical changes in the ECM [Cha08b, Toz13].

The form of amoeboid motility we observe in *physarum* also shares many characteristics with locomotion in higher organisms. The traveling wave of contraction is similar to contraction patterns observed in migrating gastropods, annelids, and *dictyostelium* slugs. In both experimental and theoretical investigations of these organisms, it has been seen that the direction of contraction wave propagation is not the critical factor in determining migration direction. Rather, migration results from the timing of interactions between the organism and substrate [Lai10, Tan12]. As we have previously discussed, this same behavior is observed in our model. Figure 4.9 clearly indicates that it is the *relative timing* of adhesive interactions, not the direction of the contraction or flow waves, which determines migration direction.

While *physarum* locomotion shares this behavior with various gastropods and annelids, we note that the amoeba moves on a vastly different scale than these organisms. The slugs observed in [Lai10] ranged from 0.7-28 cm in length, while *physarum* microplasmodia begin to migrate in this fashion after reaching a size of approximately 100 µm. This seems to indicate that a motility mechanism predicated on traveling waves of strain and appropriately timed adhesive interactions represents a robust design principle; one which is viable across length scales from cellular to macro. Indeed, the advantageous characteristics of *physarum* have not gone unnoticed by the robotics community, where the organism has been the inspiration for biomimetic design [Pio12, Ume13].

CHAPTER 5

Conclusions

5.1 Summary

In this work we have used two distinct modeling frameworks to investigate the contributions that flow of cytoplasm and hydrodynamic effects may make to the amoeboid motility observed in *physarum* microplasmodium. Specifically, we have focused on the phase wave of cytoplasmic flow observed by many investigators but qualitatively characterized in [MAT08]. In that work, it was argued that the phase-wave characteristics of the measured flows were responsible for cell motility through two effects: One, the relative phase of the peristaltic wave of cell contraction and the phase wave of fluid flow resulted in a net forward flux of fluid; and two, each individual material point of fluid in a (simplified) phase wave experiences a net forward displacement over each period of the wave. In both cases, the overall result is a net transport of mass in the direction of the phase wave, and thus, a net forward displacement of the plasmodium. It has been a major goal of this work to test these explanations, and to provide a more mechanistic understanding of how the observed peristaltic contraction of the plasmodium, the flow of internal cytoplasm, and the transmission of stresses to the substrate may be coordinated to result in cellular motility.

In Chapter 2, we analyzed a model of *physarum* microplasmodia that represented the cell as a peristaltic chamber filled with Newtonian fluid. We primarily investigated two limiting cases: a closed chamber that allowed no flux of fluid through the "head" of the cell and an open chamber that allowed fluid to flow out of the head without penalty. The results of this investigation showed that the viscous stresses associated with peristaltically driven cytoplasmic flow were of a scale that conceivably could be used to aid in cellular motility. Moreover, the model indicated that a spacial asymmetry in the peristaltic chamber (i.e. the open head) greatly increased the potential stress generation due to flow. Finally, we saw that the phase relationships between contraction and flow observed in experiments were not reproduced by either case of our model. However, our results suggested that the experimental observations might plausibly be explained by a model that included an elastic, compliant head that interpolated between our two cases. If true, this would imply that the phase relationships observed in [Mat08] are not, as hypothesized, to allow the forward flux of cytoplasmic material, but rather a necessary consequence of peristaltic pumping in a finite length chamber.

In Chapter 3, we developed a more complex model of crawling *physarum* that was more capable of describing the complex intracellular rheology of the plasmodium. Concurrently, we developed a numerical method to efficiently simulate the model in a dynamic geometry. The framework leveraged ideas from the Immersed Boundary method to represent the elastic structure of the cytoskeleton and membrane/cortex of the plasmodium, together with viscous cytosol that permeates the cell interior. This resulted in a poro-elastic description of the interior of the plasmodium, which was enclosed in an elastic membrane. Critically, our modeling framework included adhesive structures that mechanically linked the internal cytoskeleton of the plasmodium to the substrate across which the cell migrates. We also discussed discretization of our model and showed that the representation of the cytoskeleton as a discrete collection of nodes and springs approximates a linearly elastic continuum.

Finally, in Chapter 4 we used the modeling framework developed in Chapter 3 to simulate a *physarum* microplasmodium migrating across a substrate. A critical result of these investigations were that the measured phase wave of cytoplasmic flow was not responsible for determining the translation of the cell center of mass. By altering the timing of adhesive interactions with the substrate, our model cell could migrate at various speeds and in *either direction* while still displaying cytoplasmic flows consistent with experiments. Furthermore, we identified a small subset of model parameters, pertaining to adhesive interactions, that were most consistent with traction stresses and energies generated by *physarum* plasmodia in our collaborators' experiments. This subset of model parameters was shown to predict extremely efficient motility, producing a nearly optimal speed of migration within the assumptions of our model. Finally, by simulating crawling across a heterogeneous domain with spatially varying adhesiveness, we showed that this subset of model parameters was extremely robust to perturbations in cell-substrate interactions.

5.2 Future Research and Outlook

The two distinct modeling frameworks that we have used derive from several simplifying assumptions that necessarily impose modeling drawbacks. In Chapter 2, the most obvious simplifying assumption was our choice to omit a description of any elastic effects from the model. There are two components of the model where this assumption was manifest: the stress within the cytoplasmic fluid, and our treatment of the cell "head." Our assumptions pertaining to the behavior of the cell head were in part chosen to allow easy analysis of the model. While the precise elastic structure of *physarum* plasmodia is not totally understood, it seems clear that the cytoskeletal structure near the head of the microplasmodia studied here is different than the rest of the cell body. This structure is a precursor to the fan-like structure at the leading edge of fully developed plasmodia and is likely to have distinct elastic properties from the main plasmodium body. Our model does not account for elastic compliance at the leading edge of the cell. More importantly, our model indicates that this phenomenon may be *critical* to understanding motility driven by peristaltic flow. At the very least, this mechanical asymmetry in the cell is necessary to explain the observed phase relationships between deformation and flow in [Mat08]. This suggests that the directionality of the deformation wave is not the only asymmetry within the system which contributes to directed motion of the cell. The more complicated model discussed in Chapter 3 was developed in part to address this issue.

Our assumption of Newtonian stress within the cytoplasm did not actually affect the "fluid equation," as that was derived directly from an incompressibility constraint. However, it did allow us to easily calculate the characteristic stresses associated with the flow. As noted in Chapter 2, the time average viscous stresses associated with the peristaltic flow of cytoplasm are rather small, 50 or more times smaller than the maximal stresses generated during the wave. This is in part due to the "memory-less" viscous fluid that we assumed filled the chamber interior. A visco-elastic treatment of intracellular rheology may not have this issue, and depending on the visco-elastic model chosen, would be more likely to faithfully reproduce the intracellular rheology of *physarum* plasmodia. Analysis of a visco-elastic model would be necessarily more complicated. However, it is possible that such a treatment of intracellular rheology would predict larger characteristic stresses and that the "memory" of the fluid would result in much less stress lost when averaging over one period of the wave. In either the case of the leading edge of the cell head or the intracellular rheology of cytoplasm, we have good reason to suspect that elastic effects may be important in increasing the characteristic stresses of peristaltic pumping. A model that could quantify precisely *how* important elasticity is would be of scientific and biological interest.

Our computational model of crawling *physarum* developed in Chapter 3 relied on a somewhat limiting assumption regarding the elasticity of the cytoskeleton. Our goal was to discretely represent the cytoskeleton as a collection of nodes connected by springs in order to simulate the model within an IB framework. This fundamentally limited the elastic constitutive laws that we were able to represent within our model. Specifically, we were limited to a family of elastic materials parametrized by a single elastic modulus. In [Dev12], the authors develop a similar method representing elastic materials within an IB framework. However, their method does not evaluate elastic stresses in a way reminiscent of Lattice Spring Methods and can accurately represent any hyperelastic constitutive law. In addition to being less restrictive, the framework outlined in [Dev12] is derived directly from an elastic energy density functional and may therefore be relatively easy to modify to represent a visco-elastic cytoskeleton. As we have previously noted, the timescale of concern in our model is on the order of several hundred seconds. On timescales of this length, the filamentous actin that makes up a large portion of the cytoskeleton is unlikely to be a permanent structure. Individual monomers may polymerize and depolymerize as the actin network "turns over" on timescales of about a minute. This phenomenon is well studied in other motile cells where cytoskeleton is formed at the leading edge of the cell, migrates to the posterior, and is disassembled [Pol03]. Moreover, this behavior is a critical component of overall motility of the cell. A treatment of this viscous behavior is completely lacking in our model. The turnover of actin network implies that the cytoskeleton of *physarum* can reorganize over several periods of the deformation wave. What affect this may have on the particular type of amoeboid motility studied here is a completely open question, but one that our model is incapable of addressing. Incorporating a visco-elastic cytoskeleton into our existing framework would be illuminating in this regard.

Finally, we draw attention to the prescribed nature of our adhesion model. The strength of adhesion to the substrate was viewed as an input of our model and was chosen to correlate with the other wave patterns that have been observed in migrating *physarum*. It is not known precisely what structures *physarum* uses to adhere to its substrates, but in other cell types, adhesive structures such as focal adhesions are known to be mechanosensing and may change the strength of adhesion depending on the stresses or strain they experience. Both experimental and theoretical investigations have been dedicated to understanding the precise mechanism underlying this phenomenon [Ber06]. Whether *physarum* plasmodium are adhering to the substrate with integrin-like molecular binding, or pushing off of the extracellular matrix with non-specific frictional forces like those proposed in [Cha08b], it seems likely that the strength of adhesive interaction is an emergent property of the interacting mechanical stresses within the system. Our model has suggested a form which this emergent strength of adhesion may plausible take, but does not address the issue of how such a wave of adhesive strength may arise. Potentially, following the paradigm of mesenchymal migration, we might include a mechanistic model of the adhesive structures in *physarum* plasmodia that regulates the strength of adhesion based on local stresses. Conversely, in accordance with the hypothesis of [Cha08b], the strength of adhesion may be modeled as a frictional force that is a function of the local intracellular pressure. It would be of scientific value to explore both of these adhesion models and compare the emergent adhesion dynamics to the wave of adhesion postulated in this work. Such an investigation could potentially explain the emergence of the relative phase of flow and adhesion that our experimental collaborators observe and our model predicts. If the traction dynamics observed in experiments can be explained by a frictional force due to pressure, this would give more weight to the growing body of work suggesting that pressure driven protrusion and non-specific adhesion are viable cell motility strategies.

Bibliography

ACH90 Acheson, D. J. *Elementary Fluid Dynamics.* Oxford Applied Mathematics and Computing Science Series. The Clarendon Press, Oxford University Press, New York, 1990.

ALL63 Allen, R. D., W. R. Pitts, D. Speir, and J. Brault. "Shuttle-Streaming: Synchronization with Heat Production in Slime Mold." *Science*, *volume 142* (3598), 1963: pages 1485–1487.

BAS14 Bastounis, E., R. Meili, B. Alvarez-Gonzalez, J. Francois, J. C. Del Alamo, R. A. Firtel, and J. C. Lasheras. "Both Contractile Axial and Lateral Traction Force Dynamics Drive Amoeboid Cell Motility." *Journal of Cell Biology*, *volume 204* (6), 2014: pages 1045–1061.

BAU98 Bausch, A. R., F. Ziemann, A. A. Boulbitch, K. Jacobson, and E. Sackmann. "Local Measurements of Viscoelastic Parameters of Adherent Cell Surfaces by Magnetic Bead Microrheometry." *Biophysical Journal*, *volume 75* (4), 1998: pages 2038–2049.

BAU10 Baumgarten, W., T. Ueda, and M. J. B. Hauser. "Plasmodial Vein Networks of the Slime Mold Physarum polycephalum Form Regular Graphs." *Physical Review E*, *volume 82* (4), 2010: pages 046113–046113.

BAU13 Baumgarten, W. and M. J. B. Hauser. "Functional Organization of the Vascular Network of Physarum polycephalum." *Physical Biology*, *volume 10* (2), 2013: pages 026003–026003.

BER06 Bershadsky, A. A., M. M. Kozlov, and B. B. Geiger. "Adhesion-Mediated Mechanosensitivity: a Time to Experiment, and a Time to Theorize ." *Current Opinion in Cell Biology*, *volume 18* (5), 2006: pages 472–481.

BIO41 Biot, M. A. "General Theory of Three-Dimensional Consolidation." *Journal of Applied Physics*, *volume 12* (2), 1941: pages 155–164.

BRA01 Bray, D. *Cell Movements.* From Molecules to Motility. Garland, New York, 2001.

BRI87 Brix, K. and W. Stockem. "Studies on Microplasmodia of Physarum polycephalum." *Cell Biology International Reports*, *volume 11* (7), 1987: pages 529–536.

BUR88 Burridge, K., K. Fath, T. Kelly, G. Nuckolls, and C. Turner. "Focal Adhesions: Transmembrane Junctions Between the Extracellular Matrix and the Cytoskeleton." *Annual Review of Cell Biology*, *volume 4*, 1988: pages 487–525.

BUR99 Burton, K., J. H. Park, and D. L. Taylor. "Keratocytes Generate Traction Forces in Two Phases." *Molecular Biology of the Cell*, *volume 10* (11), 1999: pages 3745–3769.

BUT02 Butler, J. P., I. M. Tolic-Norrelykke, B. Fabry, and J. J. Fredberg. "Traction Fields, Moments, and Strain Energy That Cells Exert on Their Surroundings." *American Journal of Physiology - Cell Physiology*, *volume 282* (3), 2002: pages C595–C605.

Car97 Carew, E. O. and T. J. Pedley. "An Active Membrane Model for Peristaltic Pumping: Part I–Periodic Activation Waves in an Infinite Tube." *Journal of Biomechanical Engineering, Transactions of the ASME*, *volume 119* (1), 1997: pages 66–76.

Cha05 Charras, G. T., J. C. Yarrow, M. A. Horton, L. Mahadevan, and T. J. Mitchison. "Non-Equilibration of Hydrostatic Pressure in Blebbing Cells." *Nature*, *volume 435* (7040), 2005: pages 365–369.

Cha08a Chan, C. E. and D. J. Odde. "Traction Dynamics of Filopodia on Compliant Substrates." *Science*, *volume 322* (5908), 2008: pages 1687–1691.

Cha08b Charras, G. and E. Paluch. "Blebs Lead the Way: How to Migrate Without Lamellipodia." *Nature Reviews: Molecular Cell Biology*, *volume 9* (9), 2008: pages 730–736.

Cha09 Charras, G. T., T. J. Mitchison, and L. Mahadevan. "Animal Cell Hydraulics." *Journal of Cell Science*, *volume 122* (18), 2009: pages 3233–3241.

Cog10 Cogan, N. G. and R. D. Guy. "Multiphase Flow Models of Biogels From Crawling Cells to Bacterial Biofilms." *HFSP Journal*, *volume 4* (1), 2010: pages 11–25.

Cur90 Curtin, W. A. and H. Scher. "Mechanics Modeling Using a Spring Network." *Journal of Materials Research*, *volume 5* (3), 1990: pages 554–562.

DA07 Del Alamo, J. C., R. Meili, B. Alonso-Latorre, J. Rodriguez-Rodriguez, A. Aliseda, R. A. Firtel, and J. C. Lasheras. "Spatio-Temporal Analysis of Eukaryotic Cell Motility by Improved Force Cytometry." *Proceedings of the National Academy of Sciences*, *volume 104* (33), 2007: pages 13343–13348.

DA13 Del Alamo, J. C., R. Meili, B. Alvarez-Gonzalez, B. Alonso-Latorre, E. Bastounis, R. Firtel, and J. C. Lasheras. "Three-Dimensional Quantification of Cellular Traction Forces and Mechanosensing of Thin Substrata by Fourier Traction Force Microscopy." *PLoS ONE*, *volume 8* (9), 2013: page e69850.

Dem99 Dembo, M. and Y. L. Wang. "Stresses at the Cell-to-Substrate Interface During Locomotion of Fibroblasts." *Biophysical Journal*, *volume 76* (4), 1999: pages 2307–2316.

Dev12 Devendran, D. and C. S. Peskin. "An Immersed Boundary Energy-Based Method for Incompressible Viscoelasticity." *Journal of Computational Physics*, *volume 231* (14), 2012: pages 4613–4642.

DiM91 DiMilla, P. A., K. Barbee, and D. A. Lauffenburger. "Mathematical Model for the Effects of Adhesion and Mechanics on Cell Migration Speed." *Biophysical Journal*, *volume 60* (1), 1991: pages 15–37.

Fau92 Fauci, L. J. "Peristaltic Pumping of Solid Particles." *Computers & Fluids*, *volume 21* (4), 1992: pages 583–598.

Fri05 Frigo, M. and S. G. Johnson. "The Design and Implementation of FFTW3." In *Proceedings of the IEEE*. IEEE, 2005, pages 216–231.

Fun68 Fung, Y. C. and C. S. Yih. "Peristaltic Transport." *Journal of Applied Mechanics*, *volume 35* (4), 1968: pages 669–675.

Has89 Hassold, G. and D. Srolovitz. "Brittle Fracture in Materials with Random Defects." *Physical Review B*, *volume 39* (13), 1989: pages 9273–9281.

HAY08 Hayase, M., A. Maekawa, T. Yubisui, and Y. Minami. "Properties, Intracellular Localization, and Stage-Specific Expression of Membrane-Bound Beta-Glucosidase, BglM1, From Physarum polycephalum." *The International Journal of Biochemistry & Cell Biology, volume 40* (10), 2008: pages 2141–2150.

HER89 Herrmann, H. J., J. Kertész, and L. de Arcangelis. "Fractal Shapes of Deterministic Cracks." *Europhysics Letters, volume 10* (2), 1989: pages 147–152.

HOR86 Horwitz, A., K. Duggan, C. Buck, M. C. Beckerle, and K. Burridge. "Interaction of Plasma Membrane Fibronectin Receptor with Talin–a Transmembrane Linkage." *Nature, volume 320* (6062), 1986: pages 531–533.

HRE41 Hrennikoff, A. "Solution of Problems of Elasticity by the Framework Method." *Journal of Applied Mechanics, volume 8*, 1941: pages A169–A175.

IIM12 Iima, M. and T. Nakagaki. "Peristaltic Transport and Mixing of Cytosol Through the Whole Body of Physarum plasmodium." *Mathematical Medicine and Biology: a Journal of the IMA, volume 29* (3), 2012: pages 263–281.

ISE92 Isenberg, G. and W. H. Goldmann. "Actin-Membrane Coupling: a Role for Talin." *Journal of Muscle Research and Cell Motility, volume 13* (6), 1992: pages 587–589.

JAF71 Jaffrin, M. Y. and A. H. Shapiro. "Peristaltic Pumping." *Annual Review of Fluid Mechanics, volume 3*, 1971: pages 13–37.

KAM57 Kamiya, N., S. Abe, and H. Nakajima. "Simultaneous Measurement of Respiration and the Motive Force of Protoplasmic Streaming in the Myxomycete Plasmodium." *Proceedings of the Japan Academy, volume 33*, 1957: pages 206–210.

KAM59 Kamiya, N. "Protoplasmic Streaming." *Protoplasmatologia, volume VIII*, 1959.

KAM61 Kamiya, N. "Protoplasmic Streaming." *Protoplasma, volume 53*, 1961: pages 600–614.

KAM68 Kamiya, N. "The Mechanism of Cytoplasmic Movement in a Myxomycete Plasmodium." *Symposia of the Society for Experimental Biology, volume 22*, 1968: pages 199–214.

KEL00 Keller, H. U. "Redundancy of Lamellipodia in Locomoting Walker Carcinosarcoma Cells." *Cell Motility and the Cytoskeleton, volume 46* (4), 2000: pages 247–256.

KER09 Keren, K., P. T. Yam, A. Kinkhabwala, A. Mogilner, and J. A. Theriot. "Intracellular Fluid Flow in Rapidly Moving Cells." *Nature Cell Biology, volume 11* (10), 2009: pages 1219–1224.

KES82 Kessler, D. "Plasmodial Structure and Motility." In Henery Aldrich (Editor) *Cell Biology of Physarum and Didymium.* Academic Press, Inc., New York, 1982, pages 145–208.

KON09 Kong, F., A. J. García, A. P. Mould, M. J. Humphries, and C. Zhu. "Demonstration of Catch Bonds Between an Integrin and Its Ligand." *Journal of Cell Biology, volume 185* (7), 2009: pages 1275–1284.

KOY98 Koya, S. and T. Ueda. "The Onset of Rhythmic Streaming in the Physarum Plasmodium." *ACH, Models in Chemistry, volume 135* (3), 1998: pages 297–304.

KUK87 Kukulies, J., K. Brix, and W. Stockem. "Studies on Microplasmodia of Physarum polycephalum." *Cell and Tissue Research, volume 250* (1), 1987: pages 125–134.

Lai10 Lai, J. H., J. C. Del Alamo, J. Rodríguez-Rodríguez, and J. C. Lasheras. "The Mechanics of the Adhesive Locomotion of Terrestrial Gastropods." *Journal of Experimental Biology*, *volume 213* (22), 2010: pages 3920–3933.

Läm08 Lämmermann, T., B. L. Bader, S. J. Monkley, T. Worbs, R. Wedlich-Söldner, K. Hirsch, M. Keller, R. Förster, D. R. Critchley, R. Fässler, and M. Sixt. "Rapid Leukocyte Migration by Integrin-Independent Flowing and Squeezing." *Nature*, *volume 453* (7191), 2008: pages 51–55.

Läm09 Lämmermann, T. and M. Sixt. "Mechanical Modes of 'Amoeboid' Cell Migration." *Current Opinion in Cell Biology*, *volume 21* (5), 2009: pages 636–644.

Lev09 Levine, A. J. and F. C. MacKintosh. "The Mechanics and Fluctuation Spectrum of Active Gels." *The Journal of Physical Chemistry B*, *volume 113* (12), 2009: pages 3820–3830.

Li93 Li, M. and J. G. Brasseur. "Non-Steady Peristaltic Transport in Finite-Length Tubes." *Journal of Fluid Mechanics*, *volume 248*, 1993: pages 129–151.

Lim06 Lim, C. T., E. H. Zhou, and S. T. Quek. "Mechanical Models for Living Cells–a Review." *Journal of Biomechanics*, *volume 39* (2), 2006: pages 195–216.

LP94 Luby-Phelps, K. "Physical Properties of Cytoplasm." *Current Opinion in Cell Biology*, *volume 6* (1), 1994: pages 3–9.

LP00 Luby-Phelps, K. "Cytoarchitecture and Physical Properties of Cytoplasm: Volume, Viscosity, Diffusion, Intracellular Surface Area." *International Review of Cytology - A Survey of Cell Biology*, *volume 192*, 2000: pages 189–221.

Mat08 Matsumoto, K., S. Takagi, and T. Nakagaki. "Locomotive Mechanism of Physarum Plasmodia Based on Spatiotemporal Analysis of Protoplasmic Streaming." *Biophysical Journal*, *volume 94* (7), 2008: pages 2492–2504.

Mea87 Meakin, P. "A Simple Model for Elastic Fracture in Thin Films." *Thin Solid Films*, *volume 151* (2), 1987: pages 165–190.

Mit05 Mittal, R. and G. Iaccarino. "Immersed Boundary Methods." *Annual Review of Fluid Mechanics*, *volume 37* (1), 2005: pages 239–261.

Mit08 Mitchison, T. J., G. T. Charras, and L. Mahadevan. "Implications of a Poroelastic Cytoplasm for the Dynamics of Animal Cell Shape." *Seminars in Cell & Developmental Biology*, *volume 19* (3), 2008: pages 215–223.

Nag75 Nagai, R. and T. Kato. "Cytoplasmic Filaments and Their Assembly Into Bundles in Physarum Plasmodium." *Protoplasma*, *volume 86*, 1975: pages 141–158.

Nak99 Nakagaki, T., H. Yamada, and M. Ito. "Reaction–Diffusion–Advection Model for Pattern Formation of Rhythmic Contraction in a Giant Amoeboid Cell of the Physarum Plasmodium." *Journal of Theoretical Biology*, *volume 197*, 1999: pages 497–506.

Ohl95 Ohl, C. and W. Stockem. "Distribution and Function of Myosin II as a Main Constituent of the Microfilament System in Physarum polycephalum." *European Journal of Protistology*, *volume 31* (2), 1995: pages 208–222.

OS02 Ostoja-Starzewski, M. "Lattice Models in Micromechanics." *Applied Mechanics Reviews*, *volume 55* (1), 2002.

Ost84 Oster, G. F. and G. M. Odell. "Mechanics of Cytogels I: Oscillations in Physarum." *Cell Motility, volume 4*, 1984: pages 469–503.

Pál96 Pálsson, E. and E. C. Cox. "Origin and Evolution of Circular Waves and Spirals in Dictyostelium discoideum Territories." *Proceedings of the National Academy of Sciences, volume 93* (3), 1996: pages 1151–1155.

Per04 Persson, P. O. and G. Strang. "A Simple Mesh Generator in MATLAB." *SIAM Review, volume 46* (2), 2004: pages 329–345.

Pes77 Peskin, C. S. "Numerical Analysis of Blood Flow in the Heart." *Journal of Computational Physics, volume 25* (3), 1977: pages 220–252.

Pes02 Peskin, C. S. "The Immersed Boundary Method." *Acta Numerica, volume 11*, 2002: pages 479–517.

Pio12 Piovanelli, M., T. Fujie, B. Mazzolai, and L. Beccai. "A Bio-Inspired Approach Towards the Development of Soft Amoeboid Microrobots." In *Biomedical Robotics and Biomechatronics, the IEEE RAS EMBS International Conference on.* IEEE, 2012, pages 612–616.

Poi46 Poiseuille, J. "Experimental Research on the Movement of Liquids in Tubes of Very Small Diameters." *Mémoires presentés par divers savants a lAcadémie Royale des Sciences de lInstitut de France, volume 9*, 1846: pages 433–544.

Pol03 Pollard, T. D. and G. G. Borisy. "Cellular Motility Driven by Assembly and Disassembly of Actin Filaments." *Cell, volume 112* (4), 2003: pages 453–465.

Poz87 Pozrikidis, C. "A Study of Peristaltic Flow." *Journal of Fluid Mechanics, volume 180*, 1987: pages 515–527.

Rad13 Radszuweit, M., S. Alonso, H. Engel, and M. Bär. "Intracellular Mechanochemical Waves in an Active Poroelastic Model." *Physical Review Letters, volume 110* (13), 2013: page 138102.

Rie05 Rieu, J.-P., C. Barentin, Y. Maeda, and Y. Sawada. "Direct Mechanical Force Measurements During the Migration of Dictyostelium Slugs Using Flexible Substrata." *Biophysical Journal, volume 89* (5), 2005: pages 3563–3576.

Sab09 Sabeh, F., R. Shimizu-Hirota, and S. J. Weiss. "Protease-Dependent Versus -Independent Cancer Cell Invasion Programs: Three-Dimensional Amoeboid Movement Revisited." *Journal of Cell Biology, volume 185* (1), 2009: pages 11–19.

Sel01 Selverov, K. P. and H. A. Stone. "Peristaltically Driven Channel Flows with Applications Toward Micromixing." *Physics of Fluids, volume 13* (7), 2001: pages 1837–1859.

Sha69 Shapiro, A. H., M. Y. Jaffrin, and S. L. Weinberg. "Peristaltic Pumping with Long Wavelengths at Low Reynolds Number." *Journal of Fluid Mechanics, volume 37* (4), 1969: pages 799–825.

Sri09 Srinivasan, M. and S. Walcott. "Binding Site Models of Friction Due to the Formation and Rupture of Bonds: State-Function Formalism, Force-Velocity Relations, Response to Slip Velocity Transients, and Slip Stability." *Physical Review E, volume 80* (4), 2009: page 046124.

Sto94 Stockem, W. and K. Brix. "Analysis of Microfilament Organization and Contractile Activities in Physarum." *International Review of Cytology - A Survey of Cell Biology, volume 149*, 1994: pages 145–215.

TAK97A Takahashi, K., G. Uchida, Z.-S. Hu, and Y. Tsuchiya. "Entrainment of the Self-Sustained Oscillation in a Physarum polycephalum Strand as a One-Dimensionally Coupled Oscillator System." *Journal of Theoretical Biology*, *volume 184* (2), 1997: pages 105–110.

TAK97B Takamatsu, A., K. Takahashi, M. Nagao, and Y. Tsuchiya. "Frequency Coupling Model for Dynamics of Responses to Stimuli in Plasmodium of Physarum polycephalum." *Journal of the Physical Society of Japan*, *volume 66* (6), 1997: pages 1638–1646.

TAK00 Takamatsu, A., T. Fujii, and I. Endo. "Time Delay Effect in a Living Coupled Oscillator System with the Plasmodium of Physarum polycephalum." *Physical Review Letters*, *volume 85* (9), 2000: pages 2026–2029.

TAK01 Takamatsu, A., R. Tanaka, H. Yamada, T. Nakagaki, T. Fujii, and I. Endo. "Spatiotemporal Symmetry in Rings of Coupled Biological Oscillators of Physarum Plasmodial Slime Mold." *Physical Review Letters*, *volume 87* (7), 2001: page 078102.

TAN12 Tanaka, Y., K. Ito, T. Nakagaki, and R. Kobayashi. "Mechanics of Peristaltic Locomotion and Role of Anchoring." *Journal of the Royal Society Interface*, *volume 9* (67), 2012: pages 222–233.

TAY51 Taylor, G. "Analysis of the Swimming of Microscopic Organisms." *Proceedings of the Royal Society of London. Series A. Mathematical and Physical Sciences*, *volume 209* (1099), 1951: pages 447–461.

TEP91 Teplov, V. A., Y. M. Romanovsky, and O. A. Latushkin. "A Continuum Model of Contraction Waves and Protoplasm Streaming in Strands of Physarum Plasmodium." *BioSystems*, *volume 24*, 1991: pages 269–289.

TEP97 Teplov, V. A., Y. M. Romanovsky, D. A. Pavlov, and W. Alt. "Auto-oscillatory Processes and Feedback Mechanisms in Physarum Plasmodium Motility." In *Dynamics of Cell and Tissue Motion*. Birkhäuser Basel, Basel, 1997, pages 83–92.

TER86 Termonia, Y. and P. Meakin. "Formation of Fractal Cracks in a Kinetic Fracture Model." *Nature*, 1986: pages 429–431.

TER05 Tero, A., R. Kobayashi, and T. Nakagaki. "A Coupled-Oscillator Model with a Conservation Law for the Rhythmic Amoeboid Movements of Plasmodial Slime Molds." *Physica D: Nonlinear Phenomena*, *volume 205* (1-4), 2005: pages 125–135.

TER08 Teran, J., L. Fauci, and M. Shelley. "Peristaltic Pumping and Irreversibility of a Stokesian Viscoelastic Fluid." *Physics of Fluids*, *volume 20* (7), 2008: page 073101.

TER09 Teran, J. M. and C. S. Peskin. "Tether Force Constraints in Stokes Flow by the Immersed Boundary Method on a Periodic Domain." *SIAM Journal on Scientific Computing*, *volume 31* (5), 2009: pages 3404–3416.

THO99 Thoumine, O., O. Cardoso, and J. J. Meister. "Changes in the Mechanical Properties of Fibroblasts During Spreading: a Micromanipulation Study." *European Biophysics Journal*, *volume 28* (3), 1999: pages 222–234.

TOZ13 Tozluoğlu, M., A. L. Tournier, R. P. Jenkins, S. Hooper, P. A. Bates, and E. Sahai. "Matrix Geometry Determines Optimal Cancer Cell Migration Strategy and Modulates Response to Interventions." *Nature Cell Biology*, *volume 15* (7), 2013: pages 751–762.

Tre00 Trefethen, L. N. *Spectral Methods in MATLAB*, volume 10 of *Software, Environments, and Tools*. Society for Industrial and Applied Mathematics (SIAM), Philadelphia, 2000.

Ume13 Umedachi, T., R. Idei, K. Ito, and A. Ishiguro. “True-Slime-Mould-Inspired Hydrostatically Coupled Oscillator System Exhibiting Versatile Behaviours.” *Bioinspiration & Biomimetics*, *volume 8* (3), 2013: page 035001.

VP VP Scientific. “Viscosity Tables.” *http://www.vp-scientific.com/Viscosity_Tables.htm*.

Wan93 Wang, N., J. P. Butler, and D. E. Ingber. “Mechanotransduction Across the Cell Surface and Through the Cytoskeleton.” *Science*, *volume 260* (5111), 1993: pages 1124–1127.

Yam00 Yamada, S., D. Wirtz, and S. C. Kuo. “Mechanics of Living Cells Measured by Laser Tracking Microrheology.” *Biophysical Journal*, *volume 78* (4), 2000: pages 1736–1747.

Yi02 Yi, M., H. H. Bau, and H. Hu. “Peristaltically Induced Motion in a Closed Cavity with Two Vibrating Walls.” *Physics of Fluids*, *volume 14* (1), 2002: pages 184–197.

Yos10 Yoshiyama, S., M. Ishigami, A. Nakamura, and K. Kohama. “Calcium Wave for Cytoplasmic Streaming of Physarum polycephalum.” *Cell Biology International*, *volume 34* (1), 2010: pages 35–40.

Zha12 Zhao, G.-F., J. Fang, and J. Zhao. “A MLS-Based Lattice Spring Model for Simulating Elasticity of Materials.” *International Journal of Computational Methods*, *volume 09* (03), 2012: page 1250037.

Zha13 Zhang, S. “Personal Communication.”, December 2013.

APPENDIX A

Numerical Fluid Solve

In this appendix, we show the accuracy of our Pressure Poisson method for solution of the forced Stokes equation (outlined in Section 3.2.2) on a simple test problem. Our problem of choice is the so-called "four roll mill." The velocity field in the four roll mill is given by

$$\boldsymbol{u}_{true}(x, y) = \begin{bmatrix} \sin(2\pi x)\cos(2\pi y) \\ -\cos(2\pi x)\sin(2\pi y) \end{bmatrix}. \tag{A.1}$$

A quick calculation shows that this velocity field is periodic on $\mathbb{T}^2$ divergence free. Therefore $\boldsymbol{u}_{true}$ should therefore be the solution to Equation (3.30) for the appropriate forcing $\boldsymbol{f}$. In Figure A.1 we show a quiver plot of $\boldsymbol{u}_{true}$ purely for illustrative purposes. Substituting $\boldsymbol{u}_{true}$ into Equation (3.30) assuming zero pressure gradient, and solving for $\boldsymbol{f}$, we arrive at

$$\boldsymbol{f}_{true}(x, y) = \begin{bmatrix} -4\pi^2\mu\sin(2\pi x)\cos(2\pi y) \\ 4\pi^2\mu\cos(2\pi x)\sin(2\pi y) \end{bmatrix}. \tag{A.2}$$

The test problem proceeds like this:

1. For a given M_x and M_y, we generate the Eulerian grid as in Equation (3.18).
2. We evaluate the forcing function on the Eulerian grid: $\boldsymbol{f}_{true}(x^n, y^m) = \boldsymbol{f}^{nm}_{true}$.
3. This discrete forcing function is used as input for our fluid solver to produce a discrete velocity field ($\boldsymbol{u}^{nm}_{approx}$) on the Eulerian grid
4. We compute the error in our method by comparing the velocity produced by our solver to the true solution evaluated on the Eulerian Grid:

$$E^{nm} = \left|\boldsymbol{u}_{true}(x^n, y^m) - \boldsymbol{u}^{nm}_{approx}\right|. \tag{A.3}$$

5. We compute the $\mathbb{L}^\infty$ and $\mathbb{L}^2$ norms of the error:

$$\|E\|_{\mathbb{L}^\infty} = \max_{n,m} E^{nm}, \text{ and } \|E\|_{\mathbb{L}^2} = \sqrt{\sum_{n,m} (E^{nm})^2}. \tag{A.4}$$

In Figure A.2 we show the computed norms of the error E for four refinements of the Eulerian grid. As you can see, the absolute error is below 10^{-12} even for relatively unrefined grids. Note that we are analyzing absolute error because $\boldsymbol{u}_{true}$ is an order one function. The error is so low because the Fourier method that we are using allows us to solve Equation (3.30) *exactly* for functions that have a Fourier series which we can represent. Therefore, our method is as accurate as the FFT method that we use. Due to the form of $\boldsymbol{u}_{true}$, only 4 points on the Eulerian grid are required to accurately capture the Fourier series. Indeed, Figure A.3 shows a plot of the error E as a function of x and y for a very unrefined grid ($M_x = M_y = 8$). It is clear that the error in our fluid solver has already plunged to levels that approach machine precision.

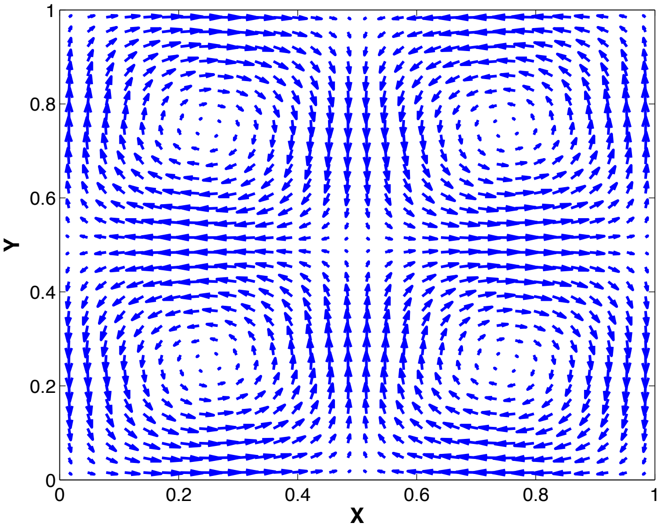

Figure A.1: Vector field illustrating the “four roll mill” velocity $\boldsymbol{u}_{true}$.

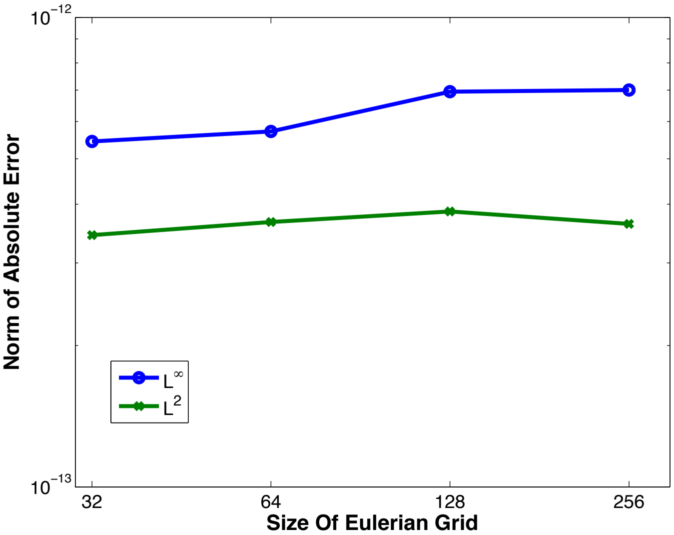

Figure A.2: Maximum and $\mathbb{L}^2$ norm of the error in computed solution for various refinements of the Eulerian grid.

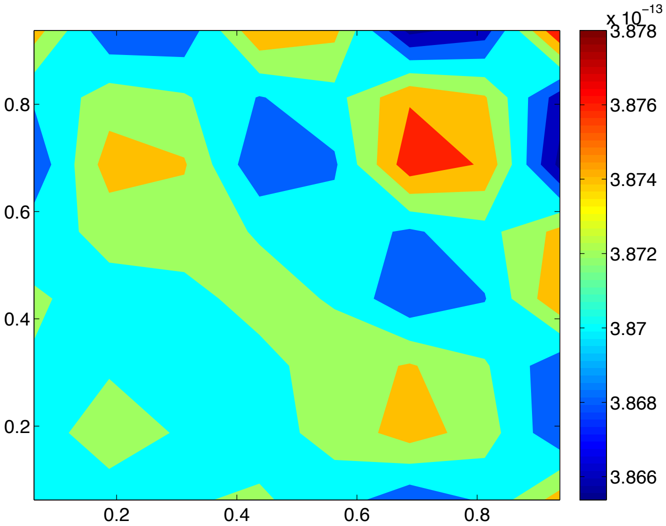

Figure A.3: Absolute error E as a function of x and y on an unrefined Eulerian mesh ($Mx = My = 8$).

APPENDIX B

Derivation of Elastic Coefficients

In this appendix, we derive expressions that relate the stiffness constants in the spring model to the elastic moduli of an isotropic elastic medium. To derive Equation (3.83) for the stiffness constant k^{ij}, we compute the discrete strain energy from a pure shear and compressive deformation. We choose k^{ij} to be consistent with the continuous strain energy density of a linear elastic material in the limit of infinitesimal deformation.

B.1 Shear Modulus

Consider a shear deformation that maps $(x, y) \rightarrow (x + \gamma y, y)$. The deformation gradient is then

$$\underline{\boldsymbol{A}} = \begin{pmatrix} 1 & \gamma \\ 0 & 1 \end{pmatrix}. \tag{B.1}$$

Let $\boldsymbol{v}^{ij} = \boldsymbol{X}^i - \boldsymbol{X}^j$ and let $\hat{\boldsymbol{v}}^{ij} = \boldsymbol{v}^{ij} / \left|\boldsymbol{v}^{ij}\right|$. From Equation (3.77) and Equation (3.78), the discrete strain energy associated with $\boldsymbol{X}^i$ is

$$\begin{aligned} E^i = \frac{k^{ij}\, d\ell^{ij}}{4} \sum_j \left(\frac{|\underline{\boldsymbol{A}}\boldsymbol{v}^{ij}| - |\boldsymbol{v}^{ij}|}{d\ell^{ij}} \right)^2 &= \frac{k}{4 d\ell^{ij}} \sum_j |\boldsymbol{v}^{ij}|^2 \left(|\underline{\boldsymbol{A}}\hat{\boldsymbol{v}}^{ij}| - 1 \right)^2 \\ &= \frac{k^{ij}}{4 d\ell^{ij}} \sum_j |\boldsymbol{v}^{ij}|^2 \left(|\underline{\boldsymbol{A}}\hat{\boldsymbol{v}}^{ij}|^2 - 2|\underline{\boldsymbol{A}}\hat{\boldsymbol{v}}^{ij}| + 1 \right) \end{aligned} \tag{B.2}$$

The quadratic term $|\underline{\boldsymbol{A}}\hat{\boldsymbol{v}}^{ij}|^2$ can be expressed as

$$|\underline{\boldsymbol{A}}\hat{\boldsymbol{v}}^{ij}|^2 = (\hat{\boldsymbol{v}}^{ij})^T \underline{\boldsymbol{A}}^T \underline{\boldsymbol{A}} \hat{\boldsymbol{v}}^{ij} = 1 + (\hat{\boldsymbol{v}}^{ij})^T \begin{pmatrix} 0 & \gamma \\ \gamma & \gamma^2 \end{pmatrix} \hat{\boldsymbol{v}}^{ij}. \tag{B.3}$$

The unit vector $\hat{\boldsymbol{v}}^{ij}$ can be written in polar coordinates as $\hat{\boldsymbol{v}}^{ij} = (\cos\theta, \sin\theta)^T$. Substituting into Eq. Equation (B.3) yields

$$|\underline{\boldsymbol{A}}\hat{\boldsymbol{v}}^{ij}|^2 = 1 + \gamma \left(2\cos\theta \sin\theta \right) + \gamma^2 \sin^2\theta. \tag{B.4}$$

Similarly, the linear term $|\underline{\boldsymbol{A}}\hat{\boldsymbol{v}}^{ij}|$ can be written as

$$|\underline{\boldsymbol{A}}\hat{\boldsymbol{v}}^{ij}| = \sqrt{|\underline{\boldsymbol{A}}\hat{\boldsymbol{v}}^{ij}|^2} = \sqrt{1 + \gamma\left(2\cos\theta\sin\theta\right) + \gamma^2\sin^2\theta}. \tag{B.5}$$

Expanding this term in the small deformation limit, $\gamma \ll 1$, yields

$$|\underline{\boldsymbol{A}}\hat{\boldsymbol{v}}^{ij}| = 1 + \gamma\cos\theta\sin\theta + \frac{\gamma^2}{2}\left(\sin^2\theta - (\cos\theta\sin\theta)^2\right) + \tag{B.6}$$

$$\frac{\gamma^3}{2}\left(-\sin^3\theta\cos\theta + (\cos\theta\sin\theta)^3\right) + \mathcal{O}(\gamma^4). \tag{B.7}$$

Retaining terms up to $\mathcal{O}(\gamma^2)$, the expression $(|\underline{\boldsymbol{A}}\hat{\boldsymbol{v}}^{ij}| - 1)^2$ simplifies to $(\gamma\cos\theta\sin\theta)^2$. Using the assumption that the network is isotropic, we average over all $\theta \in [0, 2\pi)$,

$$\langle(|\underline{\boldsymbol{A}}\hat{\boldsymbol{v}}^{ij}| - 1)^2\rangle = \frac{\gamma^2}{2\pi}\int_0^{2\pi} (\cos\theta\sin\theta)^2\, d\theta = \frac{\gamma^2}{8}. \tag{B.8}$$

Using this expresion and that $|\boldsymbol{v}^{ij}|^2 \approx (d\ell^{ij})^2$, the averaged discrete strain energy Equation (B.2) at a point is

$$E^i = \frac{k^{ij}}{4d\ell^{ij}} N_{\text{links}} \left((d\ell^{ij})^2 \frac{\gamma^2}{8}\right) = \frac{3}{16} d\ell^{ij}\gamma^2 k^{ij}, \tag{B.9}$$

where we have assumed that the average number of links to other points is $N_{\text{links}} = 6$. We note here that our above approximations hold for a regular hexagonal mesh, and our meshing algorithm produces a nearly hexagonal mesh. However, these approximations do not hold in the case of a rectangular or cartesian mesh, where the diagonal links must have a distinct length and stiffness than those lying along coordinate directions in order to obtain a continuum limit as the mesh is refined.

The strain-energy density function for an isotropic linearly elastic material is

$$W = \frac{\lambda_E}{2}\left[\text{tr}(\mathcal{E})\right]^2 + \mu_E \text{tr}(\mathcal{E}^2), \tag{B.10}$$

where the linear strain tensor is

$$\mathcal{E} = \frac{1}{2}\left(\nabla\boldsymbol{q} + \nabla\boldsymbol{q}^T\right), \tag{B.11}$$

and the displacement vector is

$$\boldsymbol{q} = \boldsymbol{X} - \boldsymbol{x} = \underline{\boldsymbol{A}}\boldsymbol{x} - \boldsymbol{x}. \tag{B.12}$$

For the shear deformation described above we have

$$\boldsymbol{q} = \begin{pmatrix} 0 & \gamma \\ 0 & 0 \end{pmatrix}\begin{pmatrix} x \\ y \end{pmatrix} \text{ and } \nabla\boldsymbol{q} = \begin{pmatrix} 0 & \gamma \\ 0 & 0 \end{pmatrix}. \tag{B.13}$$

The strain tensor is then

$$\mathcal{E} = \frac{1}{2} \begin{pmatrix} 0 & \gamma \\ \gamma & 0 \end{pmatrix}. \tag{B.14}$$

Substituting Equation (B.14) into the strain energy equation Equation (B.10) yields

$$W = \frac{\lambda_E}{2} \left[\text{tr}(\mathcal{E})\right]^2 + \mu_E \text{tr}(\mathcal{E}^2) = \frac{\lambda_E}{2} 0^2 + \frac{\mu_E}{2} \gamma^2 \tag{B.15}$$

We now convert the strain energy density (in 2-D, energy per area) to an energy for comparison to the discrete strain energy. Equation (B.9) gives the discrete strain energy at the *node* $\boldsymbol{X}_i$ in terms of the stiffness coefficient of the *link* k^{ij}. Multiplying the continuous strain energy density by the area weight dA_i and matching to the discrete strain energy for shear deformations, we obtain

$$(\mu_E \gamma^2/2) dA^i = 3k^{ij} \gamma^2 \, d\ell^{ij}/16, \tag{B.16}$$

and

$$k^{ij} = \frac{8\mu_E}{3d\ell^{ij}} dA^i. \tag{B.17}$$

However, if we use the area weight of node $\boldsymbol{X}^j$ (at the other end of the same link) to match the continuous strain energy, we obtain

$$k^{ij} = \frac{8\mu_E}{3d\ell^{ij}} dA^j. \tag{B.18}$$

To unambiguously define the stiffness coefficient, we use the average of these two quantities

$$k^{ij} = \frac{8\mu_E}{3d\ell^{ij}} \left(\frac{dA^i + dA^j}{2} \right). \tag{B.19}$$

B.2 Bulk Modulus

The bulk modulus in three dimensions is related to the Lamé constants by $K_v = \lambda_E + 2\mu_E/3$ and by $K_v = \lambda_E + \mu_E$ in two dimensions. To determine λ_E (and the bulk modulus), we consider a pure compression deformation so that the deformation gradient is

$$\underline{\boldsymbol{A}} = \begin{pmatrix} 1+\gamma & 0 \\ 0 & 1+\gamma \end{pmatrix}. \tag{B.20}$$

We compute the terms $|\underline{\boldsymbol{A}}\hat{\boldsymbol{v}}^{ij}|$ and $|\underline{\boldsymbol{A}}\hat{\boldsymbol{v}}^{ij}|^2$ that appear in Equation (B.2) for the compressive deformation Equation (B.20). The quadratic term is

$$|\underline{\boldsymbol{A}}\hat{\boldsymbol{v}}^{ij}|^2 = (\hat{\boldsymbol{v}}^{ij})^T\underline{\boldsymbol{A}}^T\underline{\boldsymbol{A}}\hat{\boldsymbol{v}}^{ij} = (\hat{\boldsymbol{v}}^{ij})^T \begin{pmatrix} (1+\gamma)^2 & 0 \\ 0 & (1+\gamma)^2 \end{pmatrix} \hat{\boldsymbol{v}}^{ij} = (1+\gamma)^2, \tag{B.21}$$

and the linear term is

$$|\underline{\boldsymbol{A}}\hat{\boldsymbol{v}}^{ij}| = (1+\gamma). \tag{B.22}$$

The averaged discrete strain energy at the point $\boldsymbol{X}^i$ is

$$E^i = \frac{k^{ij}}{4d\ell^{ij}} \sum_{i,j} |\boldsymbol{v}^{ij}|^2\gamma^2 = \frac{k^{ij}}{4} d\ell^{ij}\gamma^2 \times N_{\text{links}} = \frac{3}{2}k^{ij}d\ell^{ij}\gamma^2, \tag{B.23}$$

where again we take the average number of links at a point to be 6.

The strain tensor is simply $\mathcal{E} = \gamma\underline{\boldsymbol{I}}$, and so from Eq. Equation (B.10) the strain energy density is

$$W = \left(\frac{\lambda_E}{2}\left(4\gamma^2\right) + 2\mu_E\gamma^2\right) = 2\gamma^2\left(\lambda_E + \mu_E\right). \tag{B.24}$$

Multiplying by the same area weight as Equation (B.19), the elastic deformation energy at a point is

$$E = 2\gamma^2\left(\lambda_E + \mu_E\right)\left(\frac{dA^i + dA^j}{2}\right) = \frac{3}{2}k^{ij}d\ell^{ij}\gamma^2. \tag{B.25}$$

Taking the shear modulus from above, $\mu_E = 3k^{ij}d\ell^{ij}/(4\left(dA^i + dA^j\right))$, and solving for λ_E gives

$$\lambda_E = \frac{3}{2}\frac{k^{ij}d\ell^{ij}}{\left(dA^i + dA^j\right)} - \frac{3}{4}\frac{k^{ij}d\ell^{ij}}{\left(dA^i + dA^j\right)} = \frac{3}{4}\frac{k^{ij}d\ell^{ij}}{\left(dA^i + dA^j\right)}. \tag{B.26}$$

Note that $\lambda_E = \mu_E$, and thus a single elastic modulus characterizes the elastic material. The bulk modulus necessarily equals $2\mu_E$ in two dimensions. We conclude that

$$k^{ij} = \frac{8\lambda_E}{3d\ell^{ij}}\left(\frac{dA^i + dA^j}{2}\right). \tag{B.27}$$

Finally, we note that the stiffness coefficient has units of force, and is therefore not a traditional "spring constant." However, these units are consistent with our expression for the elastic energy within a spring, Equation (3.77).

APPENDIX C

Isotropic Contractile Stress

In this appendix, we derive the expression that relate the force of active contraction in our discrete network to a continuum isotropic stress (Equation (4.7)). We will derive the total force density at a point $\boldsymbol{s}^i$ due to contraction of the discrete isotropic network. We will then calculate the force density at a point due to an isotripic stress in the continuum model of a poro-elastic network and relate the magnitude of the two force densities. We reiterate that all calculations in this appendix are performed for a two-dimensional elastic material. To calculate the equivalent three-dimensional average stress we divide by the characteristic gap thickness (d).

Discrete Contraction As stated in Equation (4.4), in our simulations we input a contractile *force* in each link of the network. The form of this force is given by

$$\widehat{\boldsymbol{F}_a^{ij}} = f\left(\frac{\boldsymbol{s}^i + \boldsymbol{s}^j}{2}\right)\hat{r}^{ij}, \tag{C.1}$$

where $\boldsymbol{s}^i$ and $\boldsymbol{s}^j$ are the nodes at each end of the network link and $\hat{r}^{ij}$ is the orientation vector of the link. We define $\Delta\boldsymbol{s}^{ij} = \boldsymbol{s}^j - \boldsymbol{s}^i$, and we rewrite the orientation vector

$$\hat{r}^{ij} = \begin{bmatrix} \cos(\theta) \\ \sin(\theta) \end{bmatrix}. \tag{C.2}$$

This allows us to rewrite the force exerted by the link on node $\boldsymbol{s}^i$ in its components

$$\begin{aligned} \widehat{F_x^{ij}} &= f\left(\boldsymbol{s}^i + \frac{\Delta\boldsymbol{s}^{ij}}{2}\right)\cos(\theta) \\ \widehat{F_y^{ij}} &= f\left(\boldsymbol{s}^i + \frac{\Delta\boldsymbol{s}^{ij}}{2}\right)\sin(\theta). \end{aligned} \tag{C.3}$$

Now we perform a Taylor expansion of Equation (C.3) about the point $\boldsymbol{s}^i$. Because the form of g that we chose depends only on the horizontal component of $\boldsymbol{s}$, this Taylor expansion is simplified, only involves partial derivatives in one direction.

$$\begin{aligned}
\widehat{F_x^{ij}} &\approx \left(f\left(\boldsymbol{s}^i\right) + \frac{\partial f(\boldsymbol{s}^i)}{\partial x}\frac{d\ell^{ij}}{2}\cos\left(\theta\right)\right)\cos\left(\theta\right) \\
\widehat{F_y^{ij}} &\approx \left(f\left(\boldsymbol{s}^i\right) + \frac{\partial f(\boldsymbol{s}^i)}{\partial x}\frac{d\ell^{ij}}{2}\cos\left(\theta\right)\right)\sin\left(\theta\right).
\end{aligned} \tag{C.4}$$

Note that here we have assumed small strain, and therefore derivatives with respect to Eulerian and Lagrangian coordinates may be interchanged. We now make use of the fact that the network is approximately isotropic. We also assume assume that each node has 6 links emanating from it, and that each link is approximately the same length. We calculate the total force at point $\boldsymbol{s}^i$,

$$\begin{aligned}
\widehat{F_x^i} &= \frac{6}{2\pi}\int_0^{2\pi}\widehat{F_x^{ij}}\,d\theta = \frac{\partial f\left(\boldsymbol{s}^i\right)}{\partial x}\frac{3\overline{d\ell}}{2} \\
\widehat{F_y^i} &= \frac{6}{2\pi}\int_0^{2\pi}\widehat{F_y^{ij}}\,d\theta = 0.
\end{aligned} \tag{C.5}$$

Note that we would have arrived at the same expression for the total force at a point if we had assumed six evenly spaced links connected to the node $\boldsymbol{s}^i$. This gives us the total force density (due to contraction) at the point $\boldsymbol{s}^i$,

$$\begin{aligned}
F_x^i &= \frac{\widehat{F_x^{ij}}}{dA^i} = \frac{\partial g\left(\boldsymbol{s}^i\right)}{\partial x}\frac{3\overline{d\ell}}{2dA^i} \\
F_y^i &= \frac{\widehat{F_y^{ij}}}{dA^i} = 0.
\end{aligned} \tag{C.6}$$

Assuming that the network is approximately regular, this allows us to calculate the characteristic force density in the x-direction

$$F_x(\boldsymbol{s}^i) = \frac{\partial g\left(\boldsymbol{s}^i\right)}{\partial x}\frac{3\overline{d\ell}}{2\overline{dA}}, \tag{C.7}$$

where $\overline{dA}$ is the average area weight of the nodes in the network.

Isotropic Stress in a Continuum We now calculate the force density due to an isotropic stress of the form similar to the contraction we specify in Equation (4.3). We rewrite Equation (4.3) as

$$\underline{\boldsymbol{\sigma}}_a = g(\boldsymbol{s})\mathbb{I}. \tag{C.8}$$

Assuming small strain, we may interchange Lagrangian and Eulerian derivatives and a calculation immediately gives the force density due to this isotropic stress

$$\boldsymbol{F}_a = \nabla \cdot \underline{\boldsymbol{\sigma}}_a = \frac{\partial g(\boldsymbol{s})}{\partial x}\hat{x} + \frac{\partial g(\boldsymbol{s})}{\partial y}\hat{y}. \tag{C.9}$$

However, our chosen form of contractile stress does not depend on the lateral coordinate y, and therefore the force density due to active contraction is purely in the x-direction

$$F_x = \frac{\partial g(\boldsymbol{s})}{\partial x}. \tag{C.10}$$

Equating the force densities in Equations (C.7) & (C.10) and integrating with respect to x, we can relate the functional form of the discrete contractile force f and the continuous contractile stress g

$$g = \frac{3f\overline{d\ell}}{2\overline{dA}}. \tag{C.11}$$

Finally, for the particular functional forms f and g used in Chapter 4, we can relate the magnitude of discrete contractile force C and the equivalent continuous contractile stress σ_{max}

$$\sigma_{\text{max}} = \frac{3C\overline{d\ell}}{2\overline{dA}}. \tag{C.12}$$

Appendix D

Random Substrate Generation

To generate random substrates for Section 4.8, we begin with a discretized Eulerian grid of size $Nx \times Ny$. On this grid, we can represent Fourier modes with wave numbers $k_x \in [-\lfloor Nx/2 \rfloor, \lfloor Nx/2 \rfloor]$, and $k_y \in [-\lfloor Ny/2 \rfloor, \lfloor Ny/2 \rfloor]$ in the x and y directions respectively. For each Fourier mode, we draw an angle $\theta(k_x, k_y)$ out of a uniform probability distribution on the interval $(0, 2\pi)$. These are done independently, with the exception of the constraint that

$$\theta(k_x, k_y) = \theta(-k_x, k_y) = \theta(k_x, -k_y). \tag{D.1}$$

We then generate the function

$$\hat{h}(k_x, k_y) = e^{i\theta(k_x, k_y)}. \tag{D.2}$$

The constraint on θ ensures that this may be interpreted as the randomly generated Fourier representation of a *real* valued function on our Eulerian grid. We then filter these Fourier modes via multiplication with the function

$$\hat{f}(k_x, k_y) = \frac{1}{\left(1 + \sqrt{k_x^2 + k_y^2}\right)^{1.5}}. \tag{D.3}$$

After application of the filter, we define the function

$$\hat{g}(k_x, k_y) = \beta \hat{h} \hat{f}. \tag{D.4}$$

Finally, we manually set the value

$$\hat{g}(0, 0) = \mu_r, \tag{D.5}$$

and perform an inverse Fourier transform to generate the spatial heterogeneity $g(x, y)$. The parameter μ_r defines the mean of the function $g(x, y)$, while β controls its standard deviation. In practice, we found that a value of $\beta = 0.2$ resulted in a standard deviation of $\sigma_r = 0.34$ for our simulations.